CORA Cork Open Research Archive
Cartlann Taighde Oscailte Chorcaí

Title	Development of an acoustic telemetry platform for underwater sensing
Authors	Jafarzadeh, Hamed
Publication date	2021-11-14
Original Citation	Jafarzadeh, H. 2021. Development of an acoustic telemetry platform for underwater sensing. MRes Thesis, University College Cork.
Type of publication	Masters thesis (Research)
Rights	© 2021, Hamed Jafarzadeh. - https://creativecommons.org/licenses/by-nc-nd/4.0/
Download date	2026-11-08 00:13:34
Item downloaded from	https://hdl.handle.net/10468/12428



UCC
University College Cork, Ireland
Coláiste na hOllscoile Corcaigh

Ollscoil na hÉireann, Corcaigh

National University of Ireland, Cork



Development of an Acoustic Telemetry Platform for Underwater Sensing

Thesis presented by

Hamed Jafarzadeh

ORCID:0000-0002-2137-6424

For the degree of

Master of Science

University College Cork

Tyndall National Institute

Head of School/Department: Professor Jorges Oliviera

Supervisor(s): Dr Brendan O'Flynn, Marco Belcastro

2021

Table of Contents

Table of Contents 2

Table of Figures 5

Table of Tables 9

Declaration 10

Acknowledgements 11

Glossary 13

Abstract 14

1 Introduction 16

1.1 Research motivation and rationale 16

1.2 IMPAQT Project 18

1.3 Requirements of IMPAQT telemetry platform 21

1.4 The gap in the state-of-the-art summary 22

1.5 Novel Contributions 23

1.6 Contribution and organization of this thesis 23

1.7 Publications 24

2 State-of-the-art in Marine Sensing 25

2.1 Marine remote sensing systems 25

2.2 Marine wired sensing systems 28

2.3 Marine wireless sensing systems 31

2.3.1 General-Purpose Acoustic Underwater Modems 39

2.4 The gap in the state-of-the-art in acoustic wireless underwater sensing 43

3 Underwater electromagnetic communication 45

3.1 Impact of water on EM waves 45
3.1.1 Underwater path loss models 48
3.2 Experimental validation of Underwater EM transmission models 50
3.2.1 Underwater electromagnetic characterisation experimental setup 52
4 Underwater acoustic communication 58
4.1 Acoustic path loss model 59
4.1.1 Acoustic waves spreading loss 60
4.1.2 Acoustic waves absorption loss 60
4.2 IMPAQT Acoustic Transmitter Prototype 64
4.2.1 Acoustic transducers comparison and selection 66
4.2.2 Boost converters 70
4.2.3 Transducer driver 76
4.2.4 Microcontroller selection 79
4.2.5 Transmitter battery and power circuits design 81
4.2.6 Modulation methods comparison and selection 82
4.2.7 Software-based transducer oscillation damping 86
4.2.8 Communication interfaces 87
4.2.9 Acoustic transmitter board design 89
4.2.10 Acoustic transmitter power consumption estimations 90
4.3 IMPAQT Acoustic Receiver Prototype 94
4.3.1 Power supply design 95
4.3.2 Hydrophone amplifiers 98
4.3.3 Filtering and amplification of the received acoustic signal 100
4.3.4 Digitally controlled signal amplification 104

4.3.5 Received signal digitization 105
4.3.6 BPSK demodulation circuits design 107
4.3.7 OOK demodulation circuit design 115
4.3.8 Direct sampling of the received signal 117
4.3.9 USB communications 119
4.3.10 Data storage options 120
4.3.11 Received information transfer interfaces 120
4.3.12 Microcontroller selection 121
4.3.13 Acoustic receiver board design 122
5 Transceiver Systems Characterisation Tests and Results 125
5.1 Underwater electromagnetic communication test results 125
5.2 Underwater acoustic communication results 126
5.2.1 Functionality tests results of the acoustic telemetry platform 126
5.2.2 Transceiver system open-water test 130
5.2.3 Transmitter node battery life 132
5.2.4 Integration test of the transmitter node with external sensor 133
6 Conclusion and future works 135
6.1 Future Works 137
References 141
Appendix 151

Table of Figures

Figure 1 Seafood production origin (adapted from [2]) 17
Figure 2 IMPAQT Project overview (as per IMPAQT project proposal). 19
Figure 3 An overview of the telemetry platform 20
Figure 4 Schematic of multi-sensor, multi-temporal and multi-spatial remote sensing (adapted from [11]).....26
Figure 5 Schematic of airborne sonar system (adapted from [13]).....27
Figure 6 MEDUSA System in action (adapted from [15]).....29
Figure 7 YSI conductivity sensor on the left - YSI UV Nitrate sensor on the right (adapted from [16]).....29
Figure 8 YSI DB600 Data Buoy (adapted from [16]).....30
Figure 9 Injectable JSATS acoustic transmitter (adapted from [17]) 32
Figure 10 AE-FishBIT (adapted from [19]).....33
Figure 11 Wireless fish monitoring device system (left) and device (right) (adapted from [21]) 34
Figure 12 Berkeley Mica 2 Motes (adapted from [25]).....35
Figure 13 AquaBit seaweed monitoring tag (adapted from [26]).....36
Figure 14 AquaBox I (Left) - AquaBox II (Right) (adapted from [27]).....36
Figure 15 SeaSmart drone (adapted from [29]).....37
Figure 16 Cage Sense monitoring system (adapted from [33]) 38
Figure 17 WSN hardware (left) - Collaborative autonomous agent (right) [31].....39
Figure 18 PopotoSlim (adapted from [32]) 40
Figure 19 Modem M64 (adapted from [33]).....41
Figure 20 From Left to Right: Micromodem Power Amplifier, Micromodem 2.0 DSP, Micromodem Coprocessor, Micromodem Multi-Channel Analog Interface (adapted from [35]) 42
Figure 21 AHOI modem: mainboard (blue), receiver circuit (green), high-power transmitter (red), AS-1 hydrophone (adapted from [37]) 42
Figure 22 EM Signal's propagation in mediums (adapted from [43]).....46

Figure 23 River water and seawater EM waves attenuation 49
Figure 24 EM attenuation loss with frequency variations (adapted from [41]) 49
Figure 25 RF evaluation platform block diagram 54
Figure 26 RF characterisation setup 54
Figure 27 RF characterisation platform air communication test 55
Figure 28 Refractometer and its working principal (adapted from [66]) 56
Figure 29 Distance vs RSSI Underwater 57
Figure 30 Acoustic absorption coefficient and relaxation loss 62
Figure 31 Acoustic transmission loss vs distance at 42 kHz 63
Figure 32 Acoustic transmission loss vs piezo frequency at 100 m 63
Figure 33 IMPAQT Acoustic transmitter prototype board block diagram 66
Figure 34 Energy consumption as a function of source-level for PZT materials (adapted from [87]) 67
Figure 35 Voltage responses of PZT tubes of different material types (adapted from [87]) 67
Figure 36 Frequency responses of PZT tubes of different material types (adapted from [87]) 68
Figure 37 BII-7003 hydrophone 69
Figure 38 SMC3H3F380 Piezo transducer 70
Figure 39 Circuit analysis of Boost Converter (adapted from [96]) 71
Figure 40 Average current of AS-1 transducer at 20 V 72
Figure 41 Boost converter circuit 74
Figure 42 Microcontroller Based Dual-Boost converter 76
Figure 43 H-Bridge diagram (adapted from [104]) 77
Figure 44 Analog Switch internal components (adapted from [105]) 78
Figure 45 ADG1436 schematic 79
Figure 46 STM32 Microcontrollers family (adapted from [107]) 80
Figure 47 LPP 503562 Discharge Profile (adapted from [109]) 82
Figure 48 Frequency Shift Keying Modulation 83
Figure 49 Amplitude Shift KeyingModulation 84

Figure 50 Phase Shift Keying Modulation 84
Figure 51 Oscillation measurement of the AS-1 transducer.....86
Figure 52 TFBS4650 - External IrDA interface 87
Figure 53 Wired interface 88
Figure 54 IMPAQT Acoustic transmitter node characterization board 89
Figure 55 Power consumption plot and the corresponding measurements with the booster in the standby mode 93
Figure 56 IMPAQT Receiver prototype board 95
Figure 57 Charge pump inverter (adapted from [122]) 97
Figure 58 Power supply 97
Figure 59 Hydrophone amplifier with DC Servo (adapted from [123]) 98
Figure 60 Hydrophone driver simulation in LTSpice 99
Figure 61 J-Fet based hydrophone driver circuit 100
Figure 62 Recommended circuit for 4th order 380 kHz filter (adapted from [127]) 103
Figure 63 Frequency analysis of the 4th order 380 kHz filter 104
Figure 64 Schmitt trigger circuit 106
Figure 65 Single Threshold comparator (Top) vs Schmitt trigger comparator (Bottom) (adapted form[130]).....106
Figure 66 VCO-free digital BPSK demodulation (a) Proposed circuit,(b) the waveforms (adapted from [132]).....108
Figure 67 Simplified working principal of VCO-Free BPSK Demodulator.....109
Figure 68 VCO-Free BPSK demodulation simulation 109
Figure 69 A sample of the wrong demodulation 110
Figure 70 Costas loop (adapted from [131]) 111
Figure 71 Costas loop block diagram and simulation 112
Figure 72 Analog switch-based mixer 113
Figure 73 BPSK demodulator comparator stage 113
Figure 74 PLL circuit 115
Figure 75 OOK demodulation circuit 116

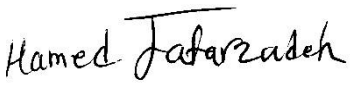
Figure 76 Envelope detector simulation 117
Figure 77 LTC2315 ADC IC 118
Figure 78 PulseView environment - an OOK signal analysis captured by IMPAQT receiver 120
Figure 79 HC-05 and IrDA transciever on the IMPAQT receiver node 121
Figure 80 The IMPAQT Receiver board layers decomposition 123
Figure 81 3D view of the IMPAQT receiver board 124
Figure 82 Annotated 3D view of the IMPAQT receiver board 124
Figure 83 The IMPAQT Telemetry platform boards 126
Figure 84 Transmitter boost convertor and modulator evaluation 127
Figure 85 OOK Modulation on the transmitter side 127
Figure 86 Filtered analog signals on the receiver side 128
Figure 87 Receiver board filtration, amplification stages results 129
Figure 88 OOK Demodulator output 129
Figure 89 Cork Harbour Marina pier deployment 131
Figure 90 SNR Measurements 132
Figure 91 STM32CubeMX Battery life estimator 133
Figure 92 The IMPAQT Transmitter node and The Unitov electronic tongue sensor integration protocol 134
Figure 93 the IMPAQT transmitter node and UNITOV electronic tongue 134
Figure 94 BPSK data received in the receiver side 139
Figure 95 IMPAQT Transmitter schematic block diagrams 151
Figure 96 LT1792-based hydrophone driver circuit 152
Figure 97 Digitally controlled variable gain amplifier 153
Figure 98 Modified Costas loop using an analog switch 154
Figure 99 Overview of the IMPAQT receiver schematic 155

Table of Tables

Table 1 IMPAQT Pilot sites 21
Table 2 Path loss exponent for different environments [42], [44], [45] 47
Table 3 Available commercial hydrophones 68
Table 4 Piezo tubes 69
Table 5 Boost converter controllers candidates 73
Table 6 Power consumption estimations from battery point of view 92
Table 7 Implemented filters in the prototype board 101
Table 8 Frequency analysis of the filters [127] 102

Declaration

This is to certify that the work I am submitting is my own and has not been submitted for another degree, either at University College Cork or elsewhere. All external references and sources are clearly acknowledged and identified within the contents. I have read and understood the regulations of University College Cork concerning plagiarism. Where other sources of information have been used, they have been acknowledged.

Signature: 

Date: 2021-11-14

Acknowledgements

First and foremost, I would like to express my deepest respect and most sincere gratitude to my supervisory team, Dr Brendan O'Flynn, and Marco Belcastro for their support, guidance, and patience throughout all stages of my work. I have been extremely lucky to have had two excellent supervisors who cared so much about me, my personal development, and my work. I'm also greatly indebted to their understanding and consultation in technical and non-technical matters which have helped me to endure some difficult times. I'm so happy about the decision that I made to be their student in the first place. I wish to thank the other members of my postgraduate committee John Barton and Dr Padraig Cantillon Murphy for their guidance and support along the way.

I want to thank my colleagues in the IMPAQT project, Caroline Peres Da Silva, Masoud Emam, Frank Kane, Joanne Casserly, Alexandro Catini, Corrado Di Natale, whom I didn't have the chance to meet in person due to Covid-19 circumstances, but they were always helpful and supportive.

I am hugely indebted to my amazing friend, Aryan Makhdoumi, and my friend, and also colleague, Omid Talebi, who spent hours discussing, consulting and helping me troubleshooting my work. I'm absolutely grateful of your assistance and support. I also had the chance to work alongside some other excellent professional people in Wireless Sensors Network group and in Tyndall national institute, which to me was a valuable, informative, and pleasant experience and I would like to thank them all for their support.

I want to thank my lovely family, and friends, especially Benedetta Petrosino, Souvik Kundu, Alireza Esfahani, Ehsan Shaghaei, and Erfan Zarinia who unconditionally supported me so far. I'm deeply thankful and blessed for having these amazing supportive family and friends.

This work is part of IMPAQT project (https://impaqtproject.eu/) – and it has received funding from the European Union's Horizon 2020 research and innovation

programme under Grant Agreement No 774109. Aspects of this publication have been funded in part by a research grant from Science Foundation Ireland (SFI) - co-funded under the European Regional Development Fund under Grant Number 16/RC/3835 – VISTAMILK and 13/RC/2077 - CONNECT. I would like to extend my gratitude to all of the mentioned funding agencies that support early career researcher and students and without their support this project would have never existed.

Glossary

IMTA – Integrated Multi-Trophic Aquaculture

GPIO – General Purpose Input Outputs

WSN – Wireless Sensor Network

UWTN – Underwater Transmitter Node

UWSN – Underwater Sensors Network

EM - Electromagnetic

IC – Integrated Circuit

IrDA – Infrared Data Association

PWM – Pulse Width Modulation

BPSK – Binary Phase-Shift Keying

OOK – On-Off Keying

I^2C – Inter-Integrated Circuit

PLL – Phase-Locked Loop

VAR – Variable Resistor

RF – Radio Frequency

FCC - Federal Communications Commission

PCB – Printed Circuit Board

RSSI – Received Signal Strength Indicator

VCC – Voltage Common Collector

DSP – Digital Signal Processor

IOT – Internet Of Things

GND – Ground

LED – Light-Emitting Diode

IC – Integrated Circuit

ADC – Analog-Digital Converter

LiPo – Lithium Polymer

DC – Direct Current

TQFP – Thin Quad Flat Pack

FPU – Floating Point Unit

MOSFET – Metal–Oxide–Semiconductor Field-Effect Transistor

COTS – Commercial Off-The-Shelf

BOM – Bill Of Materials

Abstract

With the advancement of electromagnetic communication technologies, it is now possible to transmit data wirelessly over tens of kilometers using a limited energy source which enables industries and researchers to build sophisticated wireless sensor networks in the terrestrial environment for various use cases. While there has been much progress in terrestrial electromagnetic wireless communication in recent years, underwater wireless communication has not received the same focus, and unsolved problems remain in terms of power consumption, miniaturisation, and data rates in marine-based underwater wireless sensor networks. Currently, there are a variety of sensors that can be deployed underwater, but to retrieve their data, either they must have a wired connection to the surface, or they must be physically collected to download the data after retrieval. Having a wireless underwater telemetry platform can significantly reduce the cost and efforts of deployment of marine sensors, eliminate the need for periodic sensor collection for data download, improve the reliability of underwater sensors by eliminating the need for wires and cables and provide real-time insights into the underwater sensory condition for multiple applications.

IMPAQT is a European research project aiming at the development of the technologies and methods to promote and support inland, coastal zone, and offshore Integrated Multi-Trophic Aquaculture (IMTA) sites. An underwater wireless sensor network can be hugely beneficial to the farmers as a monitoring tool that can provide real-time data sets as to the conditions in an IMTA site to help optimise conditions for growth and maximise the productivity of the aquaculture activities, as well as to potentially lead to taking early interventions against adverse events.

This thesis describes the design of the IMPAQT underwater ultrasonic wireless telemetry platform that has the potential to enable the building of small, dense wireless sensor monitoring underwater. The IMPAQT underwater telemetry platform provides a **general-purpose**, **low-cost**, **low-power, miniaturized transmitter node**, in a **one-way communication platform** for marine sensor data

collection. The IMPAQT underwater telemetry platform consists of ultrasonic transmitter nodes which can be configured in a star network and a receiver node to be used as a data aggregator and surface link for the transmitter (sensor) nodes. The transmitter node runs on a battery and provides an I/O interface through wired SPI/UART connection, wired analogue ports, and optical UART communication to be used with a variety of commonly used underwater sensors. The transmitter node periodically collects sensor information and transmits it wirelessly to the receiver node. The receiver node, which is designed to exist above the surface of the water (in a buoy or mounted on a cage), logs the transmitted information for manual collection or for transfer of the collected information to the cloud via long-range radios, e.g., GSM/LoRa to an inland data aggregator.

Keywords: *Underwater sensing, Cabled sensing, Underwater IOT, underwater modems, underwater telemetry, underwater remote sensing, Biotelemetry transmitter*

1 Introduction

1.1 Research motivation and rationale

According to the latest United Nations world population estimation, by the year 2050, the population of the earth will reach approximately 10 billion people [1], and this increase will result in a higher demand for protein in general, and in particular seafood as it is one of the main sources of food and nutrition for many people. In the past, capture fisheries production was the primary source of seafood, but this has changed in 2012, where aquaculture production volumes exceeded that of the traditional capture fisheries, and it is seen to be further increasing rapidly in recent years to meet demand [2]. From a global impact perspective, it is also essential to reduce levels of capture fisheries, as it is projected by Worm et al. [3] that by mid-century, with the harvesting pace of 2006, all species of wild seafood that are currently fished will collapse (over 90% depleted). Yet, available data suggest that these trends are still reversible [3]. In Figure 1, international levels of seafood production and production methods are shown across the world. As it can be seen, the aquaculture sector is growing quickly, and it is considered an effective way to supply global food. Aquaculture provides a secure, nutritional source while having a minimum impact on the environment with maximum benefit to society [4].

There are several aquaculture farming methods. The oldest method is the pond aquaculture system, where an artificial water pond is constructed and managed by farmers [5], where several different types of fish can be kept, making the pond system an optimal choice for the farmers in developing countries with no access to open waters. As they are situated inland and isolated from open waters, the farmers can process the wastewater to produce fertilizers. A recirculating system is a high-tech pond system that is a closed circuit of pipes that provides clean water to the ponds and pumps out the wastewater for purification and filtration, and recirculates it back to the system.

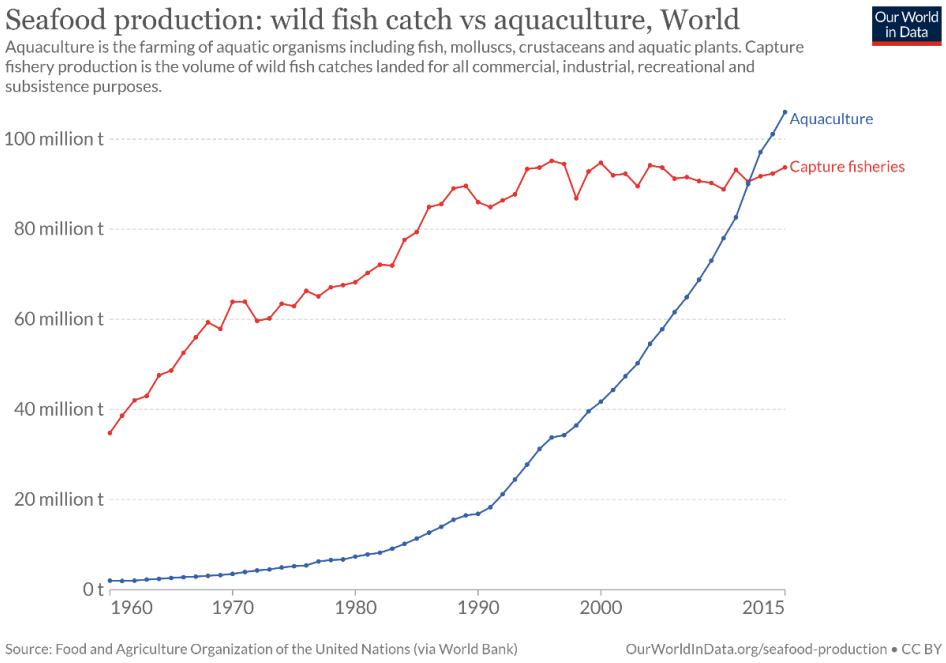


Figure 1 Seafood production origin (adapted from [2])

Open-water aquaculture is another promising method, where fish farm cages are situated in open waters at a distance from the coast, where fish are exposed to more natural living conditions and nutrients. Open-water aquaculture also provides more ecological space where the sites can expand to meet the increasing market demands for fish. To provide additional sustainability, reduce environmental impacts, and promote economic gains of open-water aquaculture, Integrated Multi-Trophic Aquaculture (IMTA) is gaining popularity among marine farmers. In IMTA, farmers combine fed species (e.g., fish, shrimp, oysters) with extractive species (e.g., seaweed, mussels), and the extractive species will use the by-products of the fed species, reducing the environmental impact of the sites and also providing commercial profit to farmers by selling both species.

In IMTA sites, where a high number of fish are kept together with other species, it is crucial to regularly monitor the water parameters, water current and waves. For instance, ammonia (NH_3) sensors can be used to determine fish feeding requirements, and along with water current sensors, they can be used to determine

extractive species placement. Hence, to maximize the commercial benefits and minimize the environmental impact of aquaculture sites; marine environmental monitoring solutions are being developed and utilized by marine researchers across the globe. There are a variety of solutions, including remote sensing, wired underwater sensors and cameras, and wireless monitoring solutions that are being used currently. In this thesis, the IMPAQT underwater telemetry platform is proposed, which replaces underwater sensor cables with an ultrasonic communication link, to reduce the complications and challenges associated with wired sensor deployment and maintenance, and potentially enable the construction of an underwater wireless sensors network. Additionally, this platform will facilitate the monitoring of marine environment by providing real-time insights and data-logging features.

1.2 IMPAQT Project

IMPAQT [6] is a European project aimed at promoting and supporting the development of IMTA sites by providing a multi-purpose (Inland, coastal, offshore), multi-sensing (heterogeneous sensors, biosensors, smart systems), and multi-functional (Monitoring, data analytics, decision making) data management platform. In the IMPAQT project, there are three main elements common with many other IoT solutions, these are data sources, databases, and analysis tools. In the IMPAQT project, **Data sources** are the flow of information from physical sensors, satellite images, and crowdsourced datasets. This information can be collected in real-time or provided to the system after post-processing. These information feed into the second part, the data management system. **The data storage and management system** stores, safe-guards, and provides a data interface for the third part, The **Intelligent Management System (IMS)**, which is the end-user interface to observe and analyse the collected data [7] and provide information to fish farmers using the system. One natural outcome of the IMPAQT project is the data it stores from the farm's sensors that can provide information to the farm owners regarding their farms, and also it can provide training data to the other farmers and improve the farming sector

performance [8]. The IMPAQT project is also enabling (close to) real-time decision making by providing farm data on the cloud for the farmers. In Figure 2, an overview of the IMPAQT project is shown.

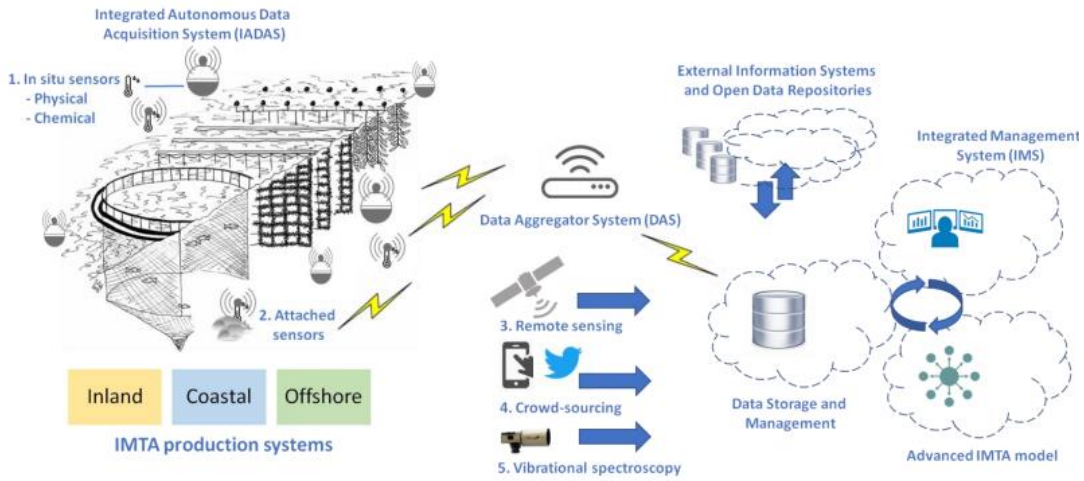


Figure 2 IMPAQT Project overview (as per IMPAQT project proposal).

As part of the IMPAQT data source systems, a communications device was required to collect information from the underwater sensors and transmit it to the data aggregator system (DAS) to provide accurate, real-time, and relevant information about the underwater environment. This underwater communications device is analogous to a terrestrial RF transmitter in a wireless sensor network and is implemented as part of a Marine Internet of Things deployment. Hence, a novel miniaturized low-power and low-cost underwater acoustic transmitter node and a buoy mounted receiver gateway have been proposed, designed and evaluated to collect data from sensors and transmit it to the inland data aggregator system (DAS). This thesis describes the **Development of an Acoustic Telemetry Platform for Underwater Sensing** implemented as part of the IMPAQT project.

In conventional marine monitoring systems, each sensor deployed in the water must have a cable connected to a logger system which usually floats on the water surface to provide logging or radio-based communications, e.g., a data logging

buoy. The use of underwater cables introduce a variety of issues. For instance, cables are a risk to motorized boats' propellers where they might get caught in or get cut off. Marine animals like sea lions might also cut the cables or move them and displace the sensor. Additionally, in small areas such as a cage or offshore farms, having several cables in the small area intensify the mentioned problems. In simple terms, the IMPAQT acoustic telemetry platform intends to replace the cables in the underwater monitoring systems, especially in IMTA sites where there might be several sensors installed in a small area. It provides a reliable communication sensor platform that can be installed in a remote location (up to 92 m from a data aggregator or hub) that resolves the risks and issues associated with the cables, eliminates the cable, as well as reduces associated deployment and maintenance costs. In Figure 3, an overview of the proposed telemetry platform is shown.

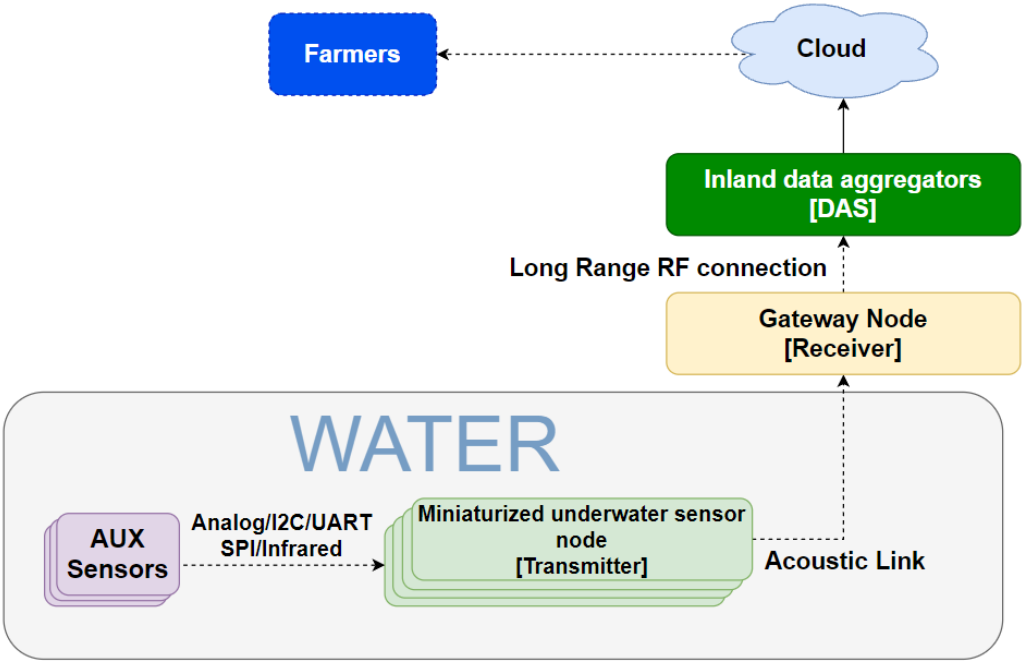


Figure 3 An overview of the telemetry platform

1.3 Requirements of IMPAQT telemetry platform

IMPAQT is a project aimed at promoting and supporting the development of IMTA sites, as described in Section 1.2. The IMPAQT consortium contains six pilot sites, which are a combination of offshore and inland waters, shown in Table 1. It can be seen from the salinity point of view; the Marine Institute (MI) sites are a combination of freshwater and seawater sites. This means that any system developed needs to be able to work in seawater and freshwater, which is challenging, particularly if Electromagnetic (EM) communications are considered (as is described in Section 3.1.1). Another important point evident from Table 1 is the maximum depth of the deployment sites. According to the data provided by the pilot site owners, the maximum depth can be up to 25 m. This is an important consideration in determining the communication range requirements for the IMPAQT telemetry platform as well as the IP rating [9] considerations for any systems deployed at that depth. Another important factor for the transmitter node is that it should be small enough to integrate with other sensors while minimizing its impact on them and the environment that the sensor is installed in, i.e., water current sensors and floating sensors. It is also important that the transmitter node run on a battery so it would be independent of the attached sensor, and it can communicate even when the attached sensor ran out of charge for up to three months based on the user configuration.

Table 1 IMPAQT Pilot sites

Parameters	**Camli**	**Mi-Marine**	**Mi-Freshwater**	**SAMS**	**NSF**	**YSFRI**
Salinity (PSU*)	25-45	0-40	0	0-35	20-40	25-35
Max Depth	20-25 m	20 m	1.5 m	1.5 m	20-25 m	7.5 m
Location	Ildır, Yalı, Çeşme/İzmir, Turkey	Doonreaghan, Galway, Ireland	Cloonloo, Co. Sligo, Ireland	Port-a-Bulin, West Coast of Scotland	Scheveningen, The Netherlands	Shandong, China

Considering the requirements defined by the project's specification phase and needs associated with collaborators' IMTA sites, it is concluded that for the short-range communications, there is a possibility to investigate electromagnetic communications systems, especially for near the water surface deployment as LoRa [10] systems were currently in use as a sensor interface communications platform. This was based on an evaluation of the state-of-art research projects and theoretical background of electromagnetic propagation underwater, and it is described in detail in Chapter 3. In Chapter 4, ultrasonic underwater communication is investigated as an alternative communications technology option, and an ultrasonic communication telemetry platform is proposed based on the project requirements.

1.4 The gap in the state-of-the-art summary

As described in detail in Chapter 2, current state-of-the-art modems are designed to have two-way communication. This is necessary for many underwater applications, including underwater robots, underwater communication systems etc., however, this is not necessary when working in underwater monitoring systems. In many underwater monitoring applications, having a transmitter-only node would be sufficient to send information to the gateway node. By having a transmitter-only node, it is possible to reduce the size and cost of the transmitter nodes significantly, which can also improve the battery life of the transmitter node. Additionally, most of the current modems are not designed to be integrated into other miniaturized and battery-powered products. By having general-purpose integrable modems, it is possible to use them in conjunction with off-the-shelf sensors and in the new products and researched-based prototypes. Another missing feature in the current modems is that the collected data need to be extracted manually on-site, and they are not featuring long-range terrestrial radios.

This gap in the state-of-the-art has been filled by the development of the IMPAQT underwater transceiver system described in this thesis.

1.5 Novel Contributions

The proposed acoustic telemetry platform for underwater sensing provides a set of features that distinguish this platform from current state-of-the-art platforms, which are listed below:

- It is a **general-purpose** telemetry platform that **can be integrated** with other sensors and devices to carry information **wirelessly** underground
- It is a **novel one-way telemetry platform** targeted at underwater monitoring applications, including an **underwater transmitter node**, **a gateway node and the possibility of terrestrial long-range communication link interface**
- It has a **miniaturized transmitter design**
- It has a **low-power** and **low-cost transmitter** compared to the state-of-the-art modems due to the limited number of components used for the transmitter-only circuit

1.6 Contribution and organization of this thesis

In this thesis, in **Chapter 1**, the motivation for this work is discussed, followed by the requirement of the IMPAQT project and the IMPAQT telemetry platform. Then the summary of the gaps in these areas, specifically in underwater wireless ultrasonic communication platforms, is described in **Chapter 2**, the state-of-the-art systems are studied in more detail with a focus on the wireless sensing systems in the market and the literature. In **Chapter 3**, the method of research for evaluating underwater electromagnetic communication is described. Initially, the related theoretical models are studied and then a practical characterisation setup is prepared and evaluated. In **Chapter 4**, which is the central part of this work, the underwater acoustic communication models are studied and then a system is proposed to meet the requirements of the project. Then the system design and circuit design of the proposed telemetry platform are discussed in detail. In **Chapter 5**, the developed telemetry platform evaluation result is shown and discussed. In **Chapter 6**, the results are concluded, and future plans and design flaws to be fixed in future are discussed.

1.7 Publications

- Jafarzadeh, H., Belcastro, M. and O'Flynn, Brendan (2020) 'IMPAQT Miniaturized Underwater Acoustic Telemetry Platform: Transmitter Node System Design', SENSORCOMM 2020, The Fourteenth International Conference on Sensor Technologies and Applications Valencia, Spain, 21-25 November, pp. 34-37. ISBN: 978-1-61208-819-8 – **Best paper award** [Link]

- H. Jafarzadeh, M. Belcastro, and B. O'Flynn, "IMPAQT miniaturized underwater acoustic sensors network platform," vol. 2020, pp. American Geophysical Union, Fall Meeting 2020, abstract #A216-0010. [Link]

- H. Jafarzadeh, M. Belcastro, and B. O'Flynn, "IMPAQT UNDERWATER ACOUSTIC TELEMETRY PLATFORM: RECEIVER DESIGN," AquaEurope 2021 Conference – [Link]

- H. Jafarzadeh, M. Belcastro, and B. O'Flynn, "Next Generation IMPAQT Miniaturized Underwater Transmitter System Design," IARIA 2021 Journals – **Accepted -** [Journal Website]

2 State-of-the-art in Marine Sensing

There are three major techniques for monitoring the marine environment: Wired sensing, wireless sensing, and remote sensing. In wired sensing, which is the most common method, scientists and researchers install various sensors in the underwater environment and connect the installed sensors using wires to the out-of-water monitoring and logging unit. In wireless monitoring, the cables get replaced by acoustic modems, electromagnetic transceivers, and optical links. In remote sensing, satellite images are used to perform analysis and measure the desired properties from these images. In the rest of this chapter, the state-of-the-art of each method is summarised, and the gap in the state-of-the-art solutions is studied.

2.1 Marine remote sensing systems

Remote sensing is the act of extracting valuable information from a distance, usually using satellite, high-altitude balloons, and aircraft images by measuring the reflected and emitted radiation of an area at a distance. In [11], Q. Xing et al. utilized multi-sensor remote sensing for hazard management. They traced the development of macroalgae, and they were able the find the cause of the incident. They have used satellite images, unmanned aerial vehicles, and ground spectroradiometers to correlate the incident with the source. They found out that these large macroalgae blooms (green tide) in the Yellow sea is related to a specific aquaculture practice at a specific location.

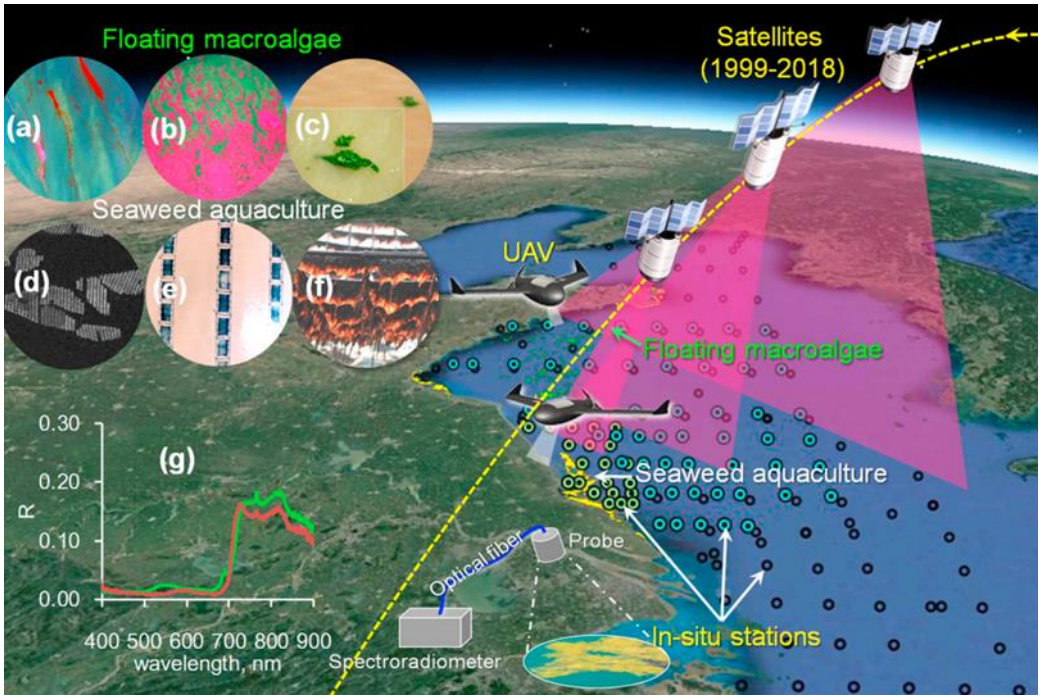


Figure 4 Schematic of multi-sensor, multi-temporal and multi-spatial remote sensing (adapted from [11])

Due to technology limitations, high-resolution imaging of the sea and ocean is limited to less than 7% of the global waters. Images taken from satellites can be coarse in pixel resolutions due to the distance from which the image is taken from the surface of the sea. In addition, the area that they cover is limited as they move around the earth in a specific flight path or orbit. To provide high-resolution imaging of the sea in its entirety, many satellites are required to cover large areas, which is costly both in terms of operation and deployment aspects [12]. Satellites use imaging sensors to analyse the reflectance intensity of different sunlight wavelengths to extract information. However, orbital errors and environmental condition errors such as weather conditions might affect the estimations. Additionally, this technique cannot be used near the coast as the signal reflection from land contaminates the radar pulses, and as a consequence, the data is unreliable at distances shorter than 40 km from the coast [12]. Hence, remote sensing cannot be used solely for monitoring the marine environment, and local monitoring is also essential to gain valuable information.

In a hybrid type local/remote sensing project, Fitzpatrick et al. [13] have developed an airborne sonar system for remote sea floor mapping, which is shown in Figure 5. Although the main goal of this project was ocean floor mapping, the idea of having an airborne mapping system can be used in other monitoring systems. The proposed airborne system by Fitzpatrick et al. shown in this figure uses the laser-induced photoacoustic effect to transmit ultrasonic sound waves and receive the reflected wave using micromachined high-sensitivity ultrasonic transducers. Using the proposed proof-of-concept, it would be possible to provide an image of a user-specified area of the sea floor with less cost as compared to satellite imaging, and in large-scale deployment, it is possible to perform high-throughput mapping of underwater areas and the sea floor. This method is a novel way of mapping sea floor but incapable of measuring other properties such as chemical properties.

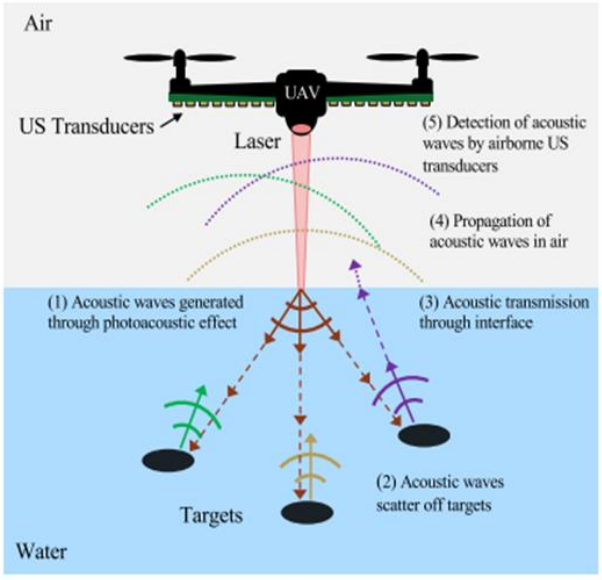


Figure 5 Schematic of airborne sonar system (adapted from [13])

2.2 Marine wired sensing systems

In Section 2.1, methods of remote sensing using satellites and drones are discussed, however, they all have a common issue, they cannot directly measure the chemical and physical properties of the seawater and animals. It is also costly and may not be practical to scan any particular desired site, as the satellites are moving in a specific path around the earth. Along with satellite data, in-situ sensor data is also needed for calibration purposes. The state-of-the-art drones can be used in hybrid remote sensing, however, similar to satellites, they cannot measure the in-situ physical and chemical properties. Hence in-situ underwater sensors are required to measure various chemical and physical properties. In this section, the wired sensing systems are discussed, and in Section 2.3, the wireless monitoring systems are discussed.

In [14], Canadian and US universities initiated a program called NEPTUNE (North-East Pacific Time-Series Undersea Networked Experiments) to install hundreds of sensors and cameras underwater to continuously provide information to the scientists on land consisting of an 800 km network of electro-optic cable laid on the seabed. This project has streamed the collected sensors data to the internet since the year 2006. In [15], MEDUSA, an aerial-aquatic robot demonstrated. A dual robot that is capable of traveling in air and landing on water, releasing an underwater micro-vehicle into water, with a cable connected to collect sensory information. In Figure 6, MEDUSA is shown.

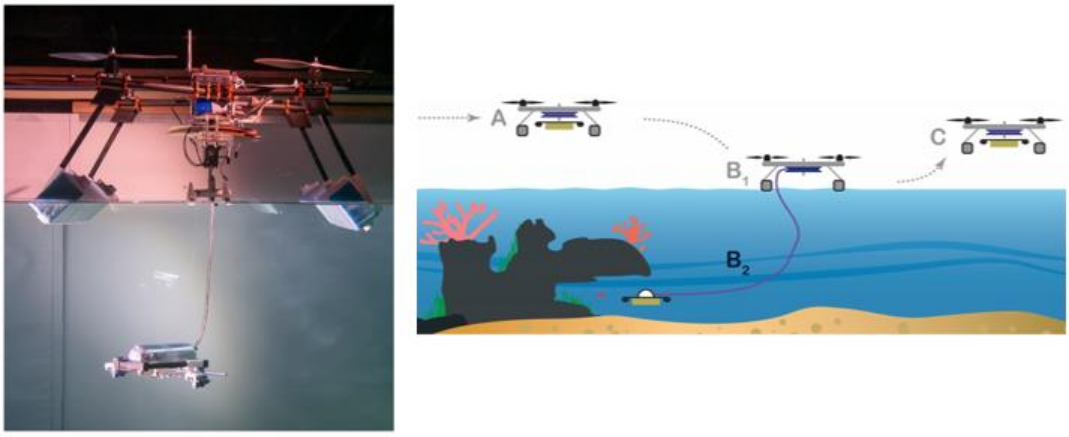


Figure 6 MEDUSA System in action (adapted from [15])

There are also various commercial cabled sensors available in the market to monitor water parameters. YSI offers a wide variety of underwater sensors including, but not limited to UV nitrate sensor, chloride, depth, conductivity, ammonia for wastewater and freshwater applications [16].

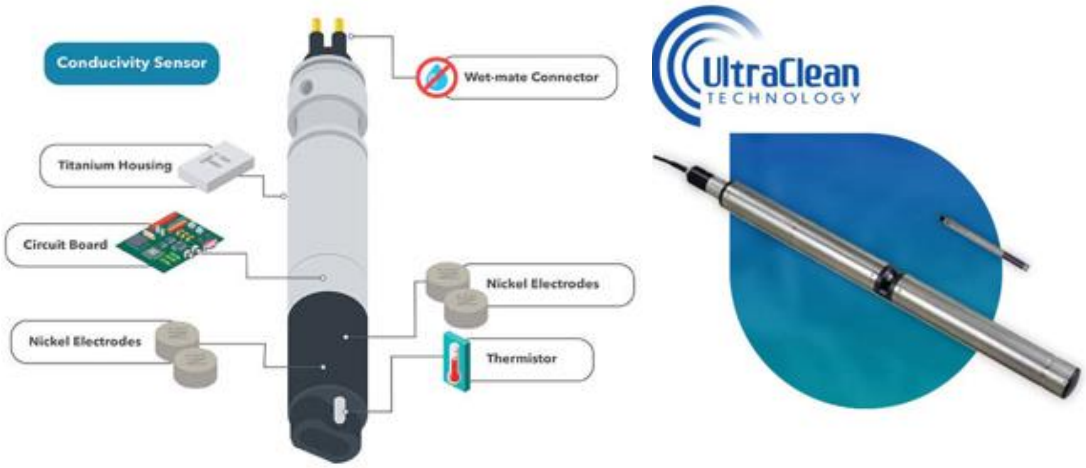


Figure 7 YSI conductivity sensor on the left - YSI UV Nitrate sensor on the right (adapted from [16])

To record and view the sensors data, a data buoy should be placed close-by to receive the data from wired sensors.



Figure 8 YSI DB600 Data Buoy (adapted from [16])

The main disadvantage of wired systems is the need to have a cable connected between the sensors and logging units. It limits the density of sensors deployment and limits the distance of the sensor's deployment while increasing the maintenance costs, especially in open-water applications. It also introduces various risks associated with cables, including tangling and getting cut by propellers and animals. Also, it is technically not possible to have many sensors in a limited space as cable management and deployment would be difficult. The advantage of wired systems is the reliability due to physical connection with surface, long battery life, dependent on surface logging unit.

2.3 Marine wireless sensing systems

There are limitations associated with wired and remote sensing systems. In remote sensing systems, most of the information's extracted from imaging sensors and reflected radiations, and it is impossible to measure various physical and chemical properties remotely. While wired systems can potentially measure the in-situ properties, there are still limitations and risks associated with them. The first and most obvious limitation is that connected sensors and devices cannot move freely underwater. They are always connected by a wire, and they have a limited reach. For instance, in marine animals tracking, a wired system cannot be used. Additionally, there are risks associated with cables, where the cables might get tangled, cut off by propellers or animals. Also, when various sensors need to be deployed in a small space, i.e. in IMTA sites, the placement and management of the cable are challenging.

A variety of wireless solutions have been investigated over the past decades. In 1987, the U.S. Army Corps of Engineers initiated a program to monitor and enhance juvenile salmon survival chances and migration behaviour. They developed Juvenile Salmon Acoustic Telemetry System (*JSATS*) to track the movement of the fish in dams, fisheries, and cages, shown in Figure 9 [17]. *JSATS* tags are extremely compact, with a length of 15 mm and a diameter of 3.38 mm, which allows them to be injected using a needle into the body of the fish. They can transmit ultrasonic pings for a year with a 15-second ping interval. But *JSATS* tags are only capable of transmitting a pre-programmed unique identification code and temperature data, and they are not able to provide any other sensor data.

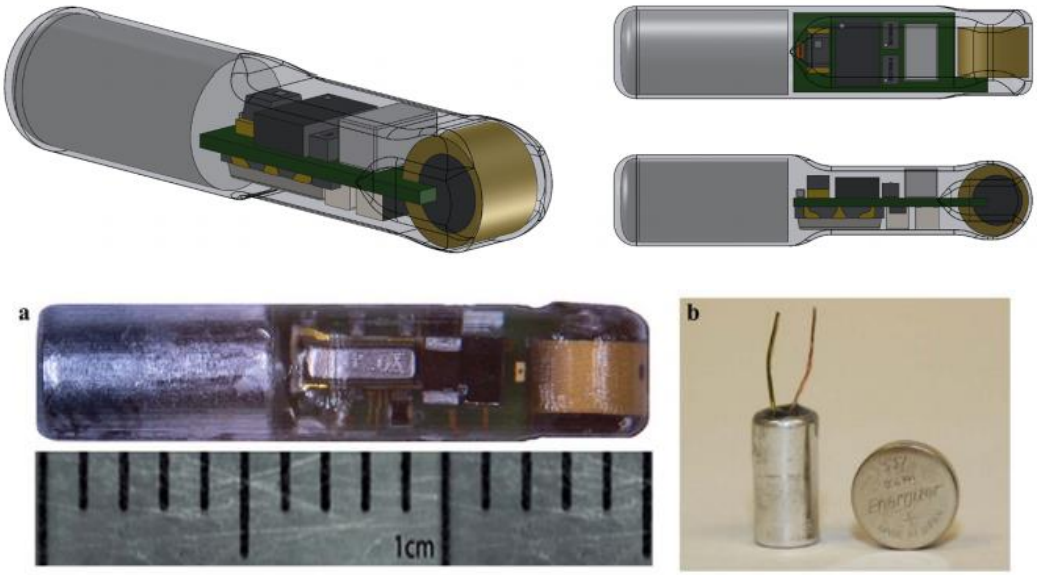


Figure 9 Injectable JSATS acoustic transmitter (adapted from [17])

J. Lu et al. [18] reported that the latest version of the *JSATS* tag can last up to 285 days with the ping rate of 15 seconds and 98 days with the ping rate of 5 seconds at 163 dB sound level, and each ping can travel up to 500 m. *JSATS* can be injected into a fish body using an 8-gauge needle.

In [19], J. A. Martos-Sitcha et al. describe the development of the *AE-FishBIT*, an ultra-low-power sensor device, for monitoring physical activities and respiratory frequency of the farmed fish using the onboard accelerometer sensor, attached to the operculum of the fish, and logging the sensors' information. *AE-FishBIT* is a small non-invasive monitoring sensor with a footprint of 14 mm x 7 mm x 7 mm and with a total mass of 600 mg. *AE-FishBIT* is not able to transmit the data, and the fish is required to be captured to download the sensors data. However, due to its form factor and size, it is easy to attach and detach the device to the operculum of the fish. The typical battery life of the tag is 1-3 months.

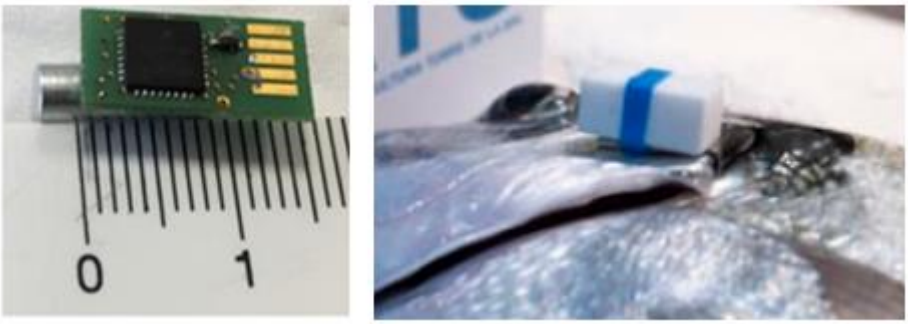


Figure 10 AE-FishBIT (adapted from [19])

Almeida et al. [20] monitored the behaviour of Lusitanian toadfish using accelerometry data provided by the externally attached *AccelTag*, which was able to log, recognize and transmit the behaviour type of the fish. The typical battery life of the tag claimed to be 30 days. It is capable of continuously recording tilt, roll, forward acceleration, lateral acceleration, vertical acceleration of fish for more than 7 hours.

In [21], C. Brockmann et al. implemented an energy-efficient system for monitoring fish in freshwater using high-frequency RF transceivers, capable of operating for one month on a single coin cell battery, with a duty cycle of 1 Hz. They utilize a low-power microcontroller, *MSP430F147*, and a low-power sub-GHz RF transceiver, *CC1101*, which transmit at 866 MHz, both from Texas Instruments. They also implemented an EMG sensor as well as a temperature sensor inside the module, which can be seen in Figure 11. They reported that the device was able to transmit data out of the fish cage, and they measured -70.52 dBm as Received Signal Strength Indicator (RSSI) outside of the fish cage, and they also reported that the module was able to cover one cubic meter of signal travelling distance.

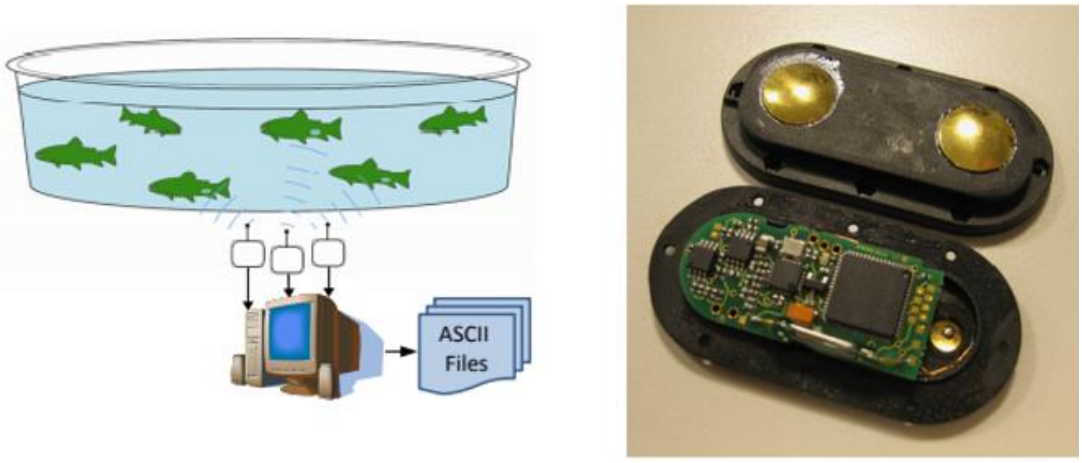


Figure 11 Wireless fish monitoring device system (left) and device (right) (adapted from [21])

In [22], Shaneyfelt et al. were looking for reliable high-speed communication links for the transmission of data between air and underwater robotic swarms. They have used 2.4 GHz XBee Pro 100 mW modules. The 2.45 GHz radiofrequency region is not optimal for marine operations as the EM waves at that frequency are significantly absorbed by water [23]. This is the reason that most microwave ovens are working within the 2.45 GHz frequency region. However, the authors were aware of this, and they reported that they were planning to test the worst-case scenario. They carried out the experiments in a regular freshwater swimming pool. In their experiment, they had a significant finding that when they put the antenna inside a plastic enclosure, the effective communication distance underwater was reduced to 2.8 meters. In contrast, when they immersed the antenna within the water, the effective range increased to 7.62 meters. Although there wasn't a clear explanation from the authors, It could be anticipated that this can be the result of the refraction caused by the air gap between the antenna and water when it was inside the plastic enclosure. A refraction will be described in Section 3.2. They also make sure that all wires and cables are shielded to ensure that the antenna is the only object radiating energy. However, their results are not in line with theories; according to the estimation model in [24] and discussions in Section 3.2, with their experiment

configuration, the propagation of the 2.4 GHz EM waves should have been limited to a range of less than 1 meter. In Section 3.1 of this thesis, the impact of water on EM waves is discussed in further detail.

In [25], Akyildiz et al. have reported that the *Berkeley Mica 2 Motes*, shown in Figure 12, traditionally a popular experimental platform in the sensor networking community, has been reported to have a transmission range of 120 cm underwater at 433 MHz by experiments performed at the Robotic Embedded Systems Laboratory (RESL) at the University of Southern California. They were not clear about the type of water, whether it was freshwater or salty water, as the salinity of the water significantly impact the communication range. In Section 3.1, the impact of water on EM waves is discussed extensively.

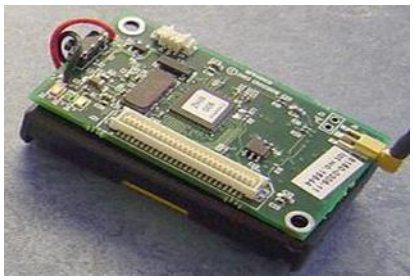


Figure 12 Berkeley Mica 2 Motes (adapted from [25])

Peres et al. [26] developed a seaweed monitoring tag, named *AquaBit*, to record the accelerometery data of seaweed movement alongside recording the temperature, light intensity and pressure of the marine environment that it is deployed in. This novel miniature low-power NFC-enabled tag records the relevant seaweed growth parameter for roughly two weeks at a 52 Hz sampling rate, and the recorded data can be downloaded using the onboard NFC transceiver and a mobile phone or using a USB cable and provided Python-based host application. Although this is an interesting portable monitoring device, it needs to be collected to extract the logged data.



Figure 13 AquaBit seaweed monitoring tag (adapted from [26])

Underwater robot sensing technologies are gaining popularity for marine engineering and resource exploration. Underwater robots can perform autonomous navigation and obstacle avoidance. They can be equipped with a variety of practical sensors for specific applications and tasks. Some robots are used in acoustic sensing applications that mainly include underwater acoustic image reconstruction and mapping, and some are used in conjunction with divers to track them while exploring [28]. In [27], Ohata et al. developed a small underwater robot system for monitoring shallow waters. It had video image streaming capabilities, and it also included a high-end laptop to perform image processing and handle decisions on the edge.



Figure 14 AquaBox I (Left) - AquaBox II (Right) (adapted from [27])

Another novel monitoring drone is called *SeaSmart* Drone. It is a patented wireless drone designed to collect marine environmental data, for instance, oxygen, salinity, biomass, and temperature, by travelling from the water surface through the aquaculture cages to collect data and returning to the surface to transmit the collected information [29]. The *SeaSmart* drone can run for six months on a single battery.

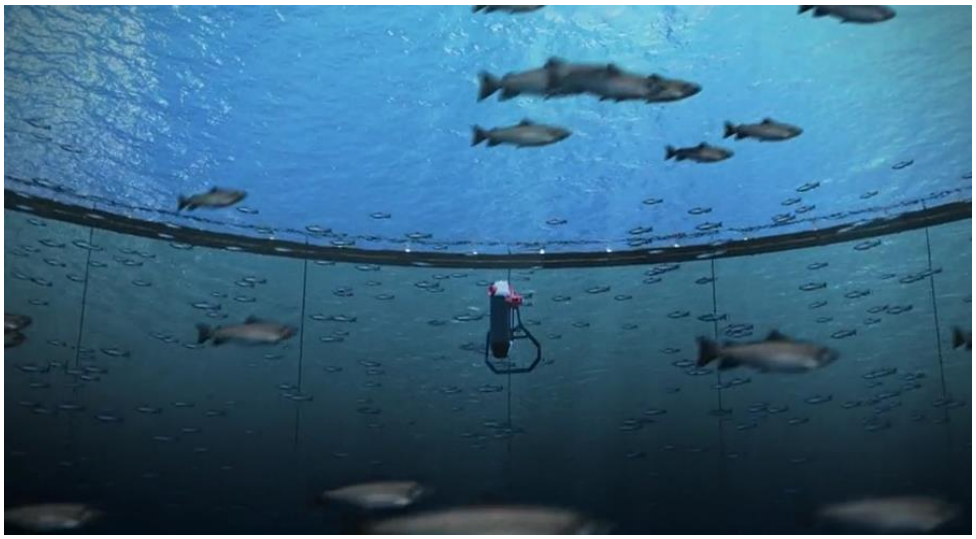


Figure 15 SeaSmart drone (adapted from [29])

The *Waterlinked* company has a solution for sensing aquaculture cages, called *CageSense*. It is a network of various sensors and gateways that provide real-time underwater sensing [30]. They provide a variety of wireless acoustic sensors that can be attached to cages using zip ties, and they can report the oxygen, salinity level, and cage's tilt and depth. There is a limited amount of information regarding these sensors at the time of writing this thesis. However, they are not providing a standalone communication platform as part of the *CageSense*, and the communication platform is embedded into their available sensors.

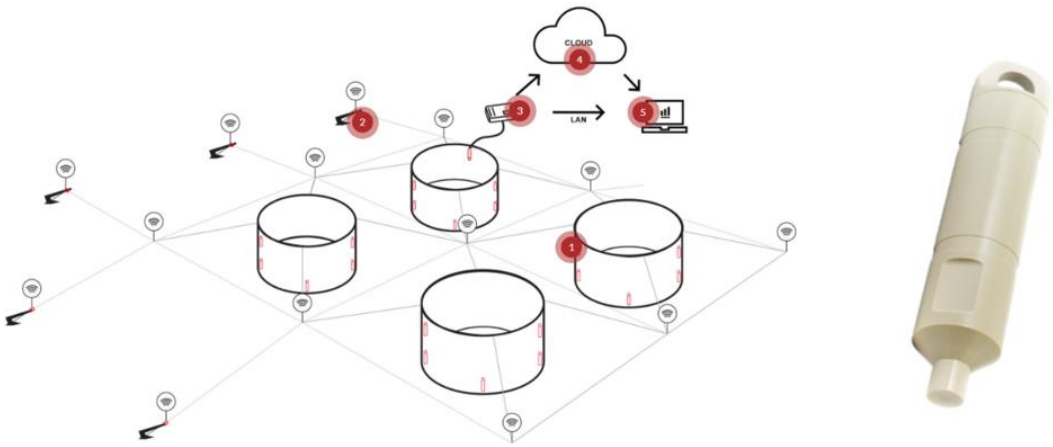


Figure 16 Cage Sense monitoring system (adapted from [33])

Apart from underwater marine life monitoring, underwater monitoring solutions can also be used in other applications. Murphy et al. [31] developed a Wireless Sensor Network (WSN) for underwater collaborative autonomous agents that can be used in the investigations of tanks and pipes within inaccessible environments, i.e. oil pipes underwater. They proposed miniaturized hardware with RF communication capability that, together with other nodes, can form an underwater sensor network to collect sensory information. They proposed an intuitive ring antenna design that can be used to receive data from various angles inside oil pipes. The proposed network consists of several nodes, each 25 cm apart from the other node that collectively acts as a network to collect information and pass it to a PC. The WSN hardware and collaborative autonomous agent with WSN hardware used inside are shown in Figure 17.

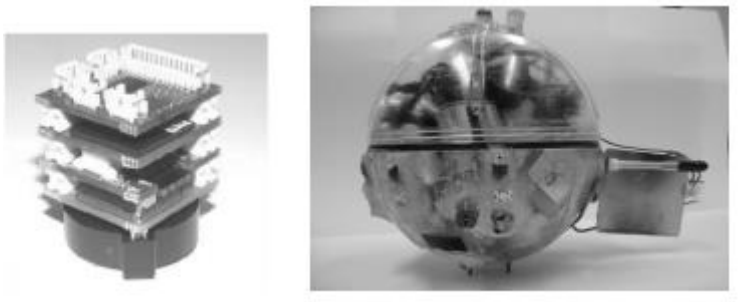


Figure 17 WSN hardware (left) - Collaborative autonomous agent (right) [31]

2.3.1 General-Purpose Acoustic Underwater Modems

Up to this point, remote sensing, wired and application-specific wireless sensing is discussed. In summary, remote sensing systems are costly both in operation and deployment, and they cover limited areas as they orbit in a particular path. They also cannot measure in-situ properties, i.e., chemical and physical properties of the water and the marine environment. On the other hand, wired sensing systems are capable of measuring in-situ properties, but their applications are limited as they need wired connections to logging or aggregator systems. There are also risks, costs and limitations associated with cables that prevent widespread usage of wired systems. Wireless sensing systems can overcome the limitations of wired systems. There are various application-specific wireless systems, which were previously introduced in this section, for instance, the tracking tags and attached fish activity monitoring systems.

However, the described wireless systems are designed to solve a specific challenge, and they are not providing a general-purpose modem that can be used in various applications. A general-purpose underwater modem is a similar concept to the RF transceiver module in terrestrial communications, where it can be integrated into products to carry data wirelessly. The development of general-purpose modems has great importance as it solves the communication challenges associated with underwater devices development and enables the researchers and developers to focus on the development of their devices rather than the communications, and it

saves costs and efforts and potentially provides the opportunity for developing novel and intuitive monitoring systems. The IMPAQT acoustic telemetry platform lies in this domain. In this subsection, the state-of-the-art underwater modems are discussed.

The Popoto company claims that their modems are robust, inexpensive, high power, and general-purpose [32]. Their *Slim modem* uses FSK and M-ary PSK modulation, and it uses a 26 kHz carrier frequency for modulation purposes. The maximum bitrate is dependent on the modulation techniques that have been used, which can be 80 bit/s in FSK mode and up to 10 kbit/s (transmit only) in PSK. It has logging capabilities, RS-232, Ethernet, and RS-422 interfaces, and its dimensions are 110 mm x 30 mm x 33 mm. It can drive up to a 20 W transducer, and it supports up to a 5 km transmission range based on the conditions and modulations selected. As *Popoto Slim* is a two-way communication module with a price point of $1750, it is not cost-effective for high-volume applications where one-way communication is only needed. This modem is designed to be used alongside a PC or other data storage hosts, and it cannot act as an independent gateway to transfer data to remote terrestrial locations.

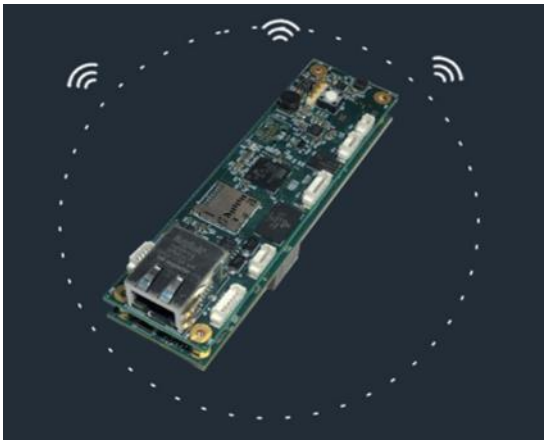


Figure 18 PopotoSlim (adapted from [32])

Waterlinked company's modem, *Modem M64*, is a two-way half-duplex 64 bit/s acoustic modem that can support up to 200 m. It has a UART interface that can be connected to underwater sensors, ROVs and AUVs. It has a cylindrical shape, with a diameter of 30 mm and length of 112 mm, and it weighs 120 g. It is working in a range of 31.25-250 kHz frequency, and there is no information about the modulation technique used [33]. Each *Modem M64* is sold at €1690 at the time of writing this thesis, and there is no transmitter-only node; hence it introduces a huge cost for high-volume application, i.e., monitoring systems, where one-way communication is only needed. It consumes 2.59 W power while in operation, and there is no information about the sleep mode power consumption.



Figure 19 Modem M64 (adapted from [33])

The institute of *Woods Hole Oceanographic* developed various versions of *WHOI Micromodems* over a decade. *WHOI Modem* is a small, lower power acoustic modem that can transfer 8-5400 bit/s using FSK and PSK modulation techniques. The modem and its parts are shown in Figure 20. These modems use DSP and FPGAs, which increase their power consumption and size significantly. The smallest low-power modem is 11 cm x 4.5 cm and consumes 0.63 W in idle mode and up to 60 W in transmission at 25 kHz. In reception mode, it consumes approximately 2.54 W in PSK mode and 0.62 W in FSK mode [34], [35], [36]. These modems need to be connected to an external device to log information, and they are not featuring long-range terrestrial connections as they are not built for monitoring solutions.

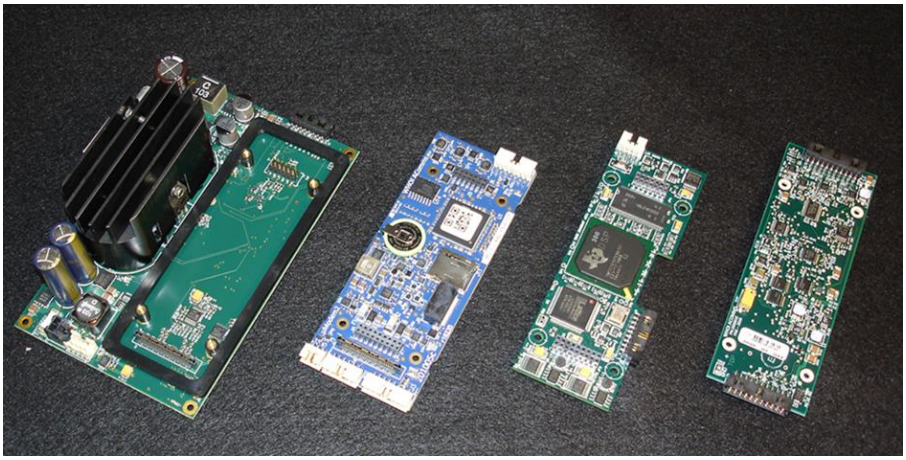


Figure 20 From Left to Right: Micromodem Power Amplifier, Micromodem 2.0 DSP, Micromodem Coprocessor, Micromodem Multi-Channel Analog Interface (adapted from [35])

B.-C. Renner et al. [37] have developed an open-source underwater acoustic modem, which is small enough to be carried by micro Autonomous Underwater Vehicles (AUVs), low-power, costs less than $600 and can be reliably communicated up to 150 m and more and it also supports ranging without adding extra hardware to it. Each board is about 50 mm x 50 mm rectangular shape, and the stack height is about 25 mm. Regarding the power consumption, in idle mode, it consumes 300 mW on average and during transmission, the consumption rises to 2.1 W and 750 mW depending on the transmit board type. The focus of this modem is underwater vehicles, where two-way communication is necessary. Considering the application, there are no logging capabilities, and it is not suited for long-term deployment considering the power consumption in idle mode. While it is a capable modem for underwater communications, it is not designed for monitoring solutions.

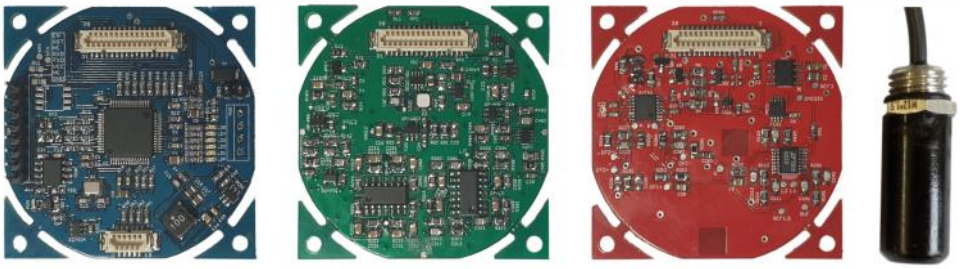


Figure 21 AHOI modem: mainboard (blue), receiver circuit (green), high-power transmitter (red), AS-1 hydrophone (adapted from [37])

2.4 The gap in the state-of-the-art in acoustic wireless underwater sensing

Although there are great efforts on monitoring underwater wired and wirelessly, there are still gaps in the technologies. The underwater modems are mostly designed in a way that they can handle full-duplex or half-duplex communication, which is not always necessary when working with sensors. In a variety of applications, including high-volume applications, a transmitter-only node would be sufficient to send sensors information to another receiver node. Having the receiving circuit incorporated in the wireless nodes will result in higher power consumption and a larger and more expensive circuit. Hence there is a lack of miniaturized, low-cost, low-power transmitter-only wireless nodes. Another gap is the lack of a general-purpose attachable transmitter with a multiple sensor interface option, where can be attached to other sensors and systems to be used as the communication platform.

On the receiver side, the state-of-the-art modems are mostly using complex circuits and FPGAs to demodulate various modulation schemes to maximize the communication throughput, which naturally results in higher power consumption and a larger and more expensive circuit, where they can be minimized by using a simpler modulation like OOK, where a high-bandwidth, high-speed communication are not critical factors. Additionally, one important lacking feature in the state-of-the-art modems is that they are not featuring long-range terrestrial connection. They are local, and the user needs to extract the data manually. LoRa communication can be used to have real-time data on the cloud, and it would be a great addition to the monitoring systems, and it is a step forward toward the internet of underwater things.

The IMPAQT Underwater communication platform developed and described as part of this thesis provides a **general-purpose**, **low-cost, miniaturized**, **low-power**, **one-way telemetry platform** for monitoring underwater environments where the

data flows from transmitter nodes to the water-surface receiver node and from the receiver node to shore stations using **LoRa communication interface**. The IMPAQT underwater communication platform provides a full-stack underwater monitoring platform from edge sensors to data aggregator systems. By incorporating digital and analog sensors' communication interface, it essentially replaces the sensor cables underwater and improves the sensor's signal to noise ratio by reading the sensor data in-situ. Such a system has not been previously reported in the literature. The proposed system will be a great addition to IMTA sites, especially which can help farmers to collect information in real-time and make informed decisions as regards their crop care in a timely fashion to optimise crop yield.

3 Underwater electromagnetic communication

Electromagnetic communications are the most commonly used data transmission method in terrestrial wireless sensing applications. Various off-the-shelf transceivers can be used in terrestrial applications, from low-power, microscale transceivers to giant satellite antennas [38], and there is significant research ongoing in this domain in terms of power consumption optimization [39] and its applications [40]. However, in underwater communications, the electromagnetic transceiver options are not an ideal means of data transmission. Several factors affect EM signals propagation underwater and make it challenging to develop general-purpose underwater electromagnetic transceivers and communications systems [41]. In underwater applications, electromagnetic signal transmission loss increases in conjunction with increasing the frequency, while by decreasing the frequency, the antenna size increases [42]. So, there is a trade-off between the required range and antenna size. In this subsection, the theoretical background is discussed, and the associated practical test is described.

3.1 Impact of water on EM waves

In various publications, researchers have studied electromagnetic wave propagation underwater [21], [24], [25], [41]. In communication systems, the link budget defines the maximum range that a signal can travel and be detected by the receiver. The link budget is the sum of all power gains and losses that affect the signal during transmission. The transmitter power and antenna gain are positive gains, and path loss, fading, connector loss, and receiver's efficiency are negative gains. Receiver sensitivity indicates the minimum signal strength level required for a receiver to detect a transmitted signal. If the sum of all mentioned positive and negative gains stays above receiver sensitivity, the receiver can detect the transmitted signal. In Figure 22, adapted from [43], link budget parameters are shown.

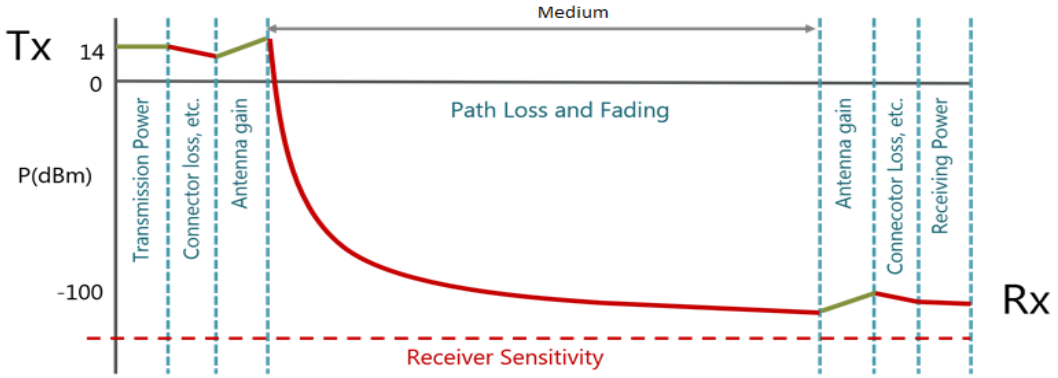


Figure 22 EM Signal's propagation in mediums (adapted from [43])

To calculate the link budget for an RF system, a number of parameters are required [43]. Transmission power is the transmitter output wattage limited by FCC regulations, power supply rating, and amplifier circuit size. Connector loss includes the power loss associated with electrical traces on the PCB, antenna wires and antenna connector quality, etc. Antenna gain is defined by how the antenna converts input power into radio waves in a specific direction. After the antenna emits the EM signals, they travel through the medium, where they attenuate, and the amount of attenuation is defined by the path loss model. The path loss model will be discussed in more detail later in this section. On the receiver side, depending on the antenna's effectiveness in converting the electromagnetic signal to an electrical signal, the signal level may get amplified or reduced. The received signal then travels through the antenna cable and connector in the receiver board, which generally is lossy, and then finally, it will be received by the receiver circuit. Each receiver circuit usually specifies a property called “Receiver Sensitivity“, which will define the minimum required amplitude of the electrical signal so that it can be detected. Among the link budget elements, the path loss is primarily controlled by the medium through which the EM signal passes, and it is only related to the physical and chemical properties of the medium. For example, in the IMPAQT project, the mediums are freshwater and seawater, and seawater attenuates electromagnetic signals severely due to its saltiness, fresh water has less of an impact (although it is still significant).

There are various parameters that affect signal propagation underwater, which are studied extensively in [24], [41], [42], [44]. In the rest of this section, they are briefly introduced.

Path loss attenuation: Path loss attenuation is the amount of wave signal degradation that occurs when a wave propagates in a medium channel. The amount of path loss attenuation depends on the conductivity and distance that the signal has travelled. It is channel and frequency-specific. For the underwater medium, the major contributors to the signal attenuation are EM properties of water, absorption loss, and multipath, etc. [42]. Equation 1 shows the relation between signal power (P_r), and distance (d), where (n) is the path loss exponent, shown in Table 2 [42], [44], [45].

$$P_r \propto d^{-n} \quad 1$$

Equation 1 shows that the signal power decreases as the distance between transmitter and receiver increases.

Table 2 Path loss exponent for different environments [42], [44], [45]

Environment	Path loss exponent "n"
Free space	2
Urban area cellular radio	2.7 to 3.5
Shadowed urban cellular radio	3 to 5
In building line-of-sight	1.6 to 1.8
Obstructed in building	4 to 6
Obstructed in factories	2 to 3
Underwater	2 to 4

Electro-Magnetic properties of water*:* Utilizing a high-frequency radio band enables high-speed communication; however, the disadvantage of using high frequencies underwater is that the signal will suffer from severe attenuation. Thus, it is unable to travel long distances. A significant contributor to this

attenuation is the dielectric permittivity of water and the electrical conductivity of the medium. Electrical conductivity is related to the type of water. Commonly, for seawater, the conductivity is 4 S/m (Siemens per meter), which is approximately 400 times higher than the conductivity of freshwater, which is typically around 0.01 S/m [46]. It is important to note that the seawater conductivity depends on the location and depth, and it has been studied in [47]. With an increase in electrical conductivity, the overall propagation distance decreases. Freshwater is considered a low-loss medium due to its low conductivity; this enables EM waves to propagate in freshwater better than in seawater.

3.1.1 Underwater path loss models

There are two primary electromagnetic path losses (L_{EM}) that happen in underwater RF communication. Attenuation ($L_{\alpha,\varepsilon}$) in dB/m due to the conductivity and complex permittivity and reflection loss (L_R) in dB at the water-air boundaries as shown in the equation below. In the IMPAQT project, there is no communication out of the water, and both transmitters and receivers are supposed to be underwater. Hence the reflection loss (L_R) will be 0 dB. Electromagnetic path loss (L_{EM}) in dB can be represented as follow:

$$L_{EM} = L_{\alpha,\varepsilon} + L_R \quad (2)$$

There are two interesting proposed models in [24], [41] regarding electromagnetic path loss estimation. In [24], which was published in 1987, Butler proposed an estimation model for attenuation loss ($L_{\alpha,\varepsilon}$) and reflection loss (L_R), and then he performed various experiments in the Adelaide river to verify his proposed equation. In Equation 3, his proposed model is shown, where $L_{\alpha,\varepsilon}$ is attenuation in dB/meter, f is the frequency in hertz, and σ is conductivity in mhos/meter.

$$L_{\alpha,\varepsilon} = 0.0173\sqrt{(f\sigma)} \quad (3)$$

In Figure 23, the attenuation for Adelaide river ($\sigma = 0.054$ mhos/meter) and seawater ($\sigma = 4$ mhos/meter) is shown.

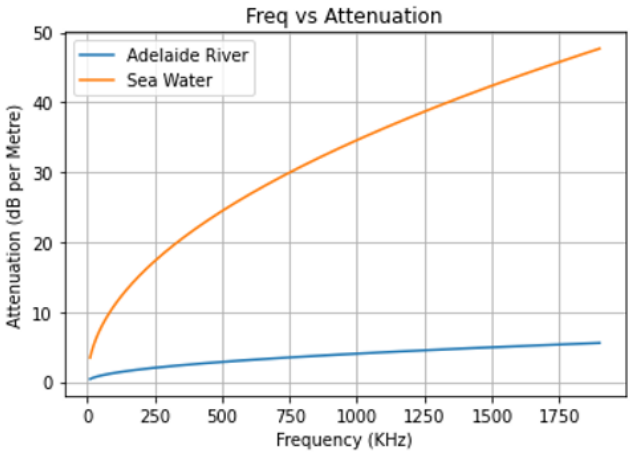


Figure 23 River water and seawater EM waves attenuation

In [41], Hattab et al. proposed a realistic radio frequency path loss model in comparison with Al-Shamma'a et al. [48] and Uribe et al. [49] for seawater environment. The attenuation loss with frequency variations is shown in Figure 24.

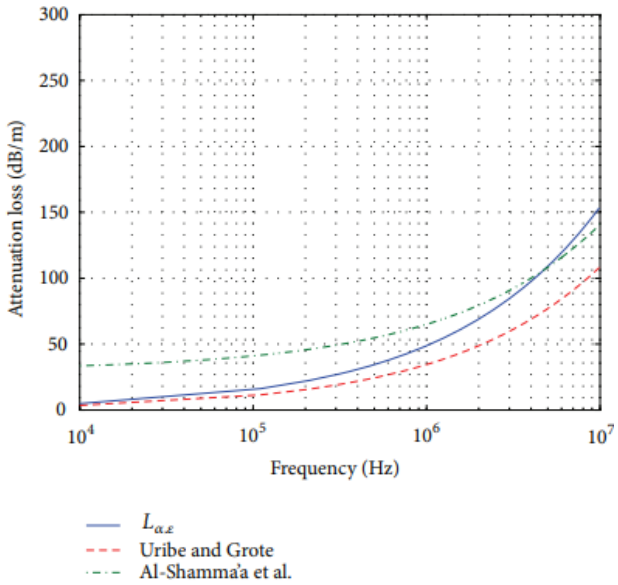


Figure 24 EM attenuation loss with frequency variations (adapted from [41])

3.2 Experimental validation of Underwater EM transmission models

As discussed in the previous section, various theoretical models are used to estimate the path loss model for underwater electromagnetics propagation. To evaluate the propagation of EM waves underwater for use in very short range sensor communications, it has been decided to use general-purpose LoRa transceivers. LoRa transceivers are well-known for their long-range capabilities in terrestrial communications with very little power consumption. LoRa uses a modified (Sub GHz) frequency modulation (frequency-shift keying) that allows data to be transferred over a long-range [50]. Hence, considering its working range, LoRa was considered to be a good candidate for underwater testing. Current state-of-the-art LoRa transceivers by Semtech, *SX127x* series, offer a receiver sensitivity of -133 dBm with the most optimal configuration [51]. SX127x series are able to operate in the frequency range of 169 MHz to 868 MHz. According to the models proposed by Butler [24] as well as Hattab et al. [41], at a frequency of 169 MHz, the travelling distance for the *SX127x* series should be approximately 2.3 meters in freshwater and less than 20 cm in seawater. Similarly, at a frequency of 868 MHz frequency, the transmission range is limited to less than 110 cm in freshwater and less than 13 cm in seawater according to the same path loss models. When it comes to real-world environments, various additional parameters can also attenuate the communication range. To outline some effective real-world parameters in underwater electromagnetic communication, these can be summarized below:

Refraction: as the electromagnetic waves transient from the antenna into the water, their speed will change significantly to adjust to the propagation speed in the water. If there would be an air gap between the antenna and water, this also makes the signal attenuate more since it urges the signal to change its propagation speed three times as it goes from antenna to air and then from air to water.

Diffraction: When signals are propagating underwater, they may encounter obstacles, and it causes the waves to bend around the corners of the obstacle, this results in the signal losing energy.

Reflection: It occurs when a signal wave reflects from objects or surfaces underwater. In underwater applications, it can be the water surface or the sea/river floor. Reflections result in multiple paths of signals arriving at the receiver with a slight delay, causing fading or amplification of the signals.

Scattering: This happens when a signal wave hits an object with irregularities or rough surface, It causes the wave to propagate in various directions, which will result in receiving the signal from multiple paths at the receiver side, and it reduces signal energy as it is dispersed in the broader area.

The above properties are hard to estimate using theoretical models since they are heavily dependent on the environment. Hence, tests were performed using an EM wave characterization platform to validate the theoretical models and observe the communication in the practical test environment. To choose the transceiver modules, the following criteria are considered:

Frequency range: Lower frequency EM waves attenuate less in underwater environments, which results in a higher transmission range; however, the lowest possible frequency is limited by antenna size. A low-frequency communication requires a large antenna, which is not preferred in the IMPAQT application. At the time of writing this thesis, available off-the-shelf LoRa transceiver's frequencies were between 169 MHz to 2.4 GHz.

Antenna size can be determined using the wavelength of the transceiver, which can be calculated using the following equation [52]:

$$\lambda = \frac{v}{f} \qquad 4$$

Where λ is wavelength in meters, v is the speed of the wave in a medium (For radio waves in air, it is approximately 2.998 x 10^8 m/s, and for seawater at

169 MHz is approximately 2.1 x 10^7 m/s [53]), f is the frequency of the wave [54, p. 4].

For instance, the wavelength of 169 MHz in the air is 177.392 cm. Estimation of the wavelength for seawater is discussed in [24]. As resonance can occur at smaller wavelength fractions, an antenna can be 1/2, 1/4, 1/8 of the wavelength.

Transmission power and transmitter antenna gain: Higher transmission power and antenna gain result in a higher communication range. There are various modules with a wide range of transmission power available in the market. Regarding the antenna gain, in a reasonable dimension of shorter than 20 cm, there were up to 5 dBi whip antennas available in the market [55].

Receiver sensitivity and receiver antenna gain: Lower receiver sensitivity in simple terms means a higher possibility of detecting weak signals, resulting in a higher communication range. Higher antenna gain on the receiver side also increases the communication range. To achieve better gain, it is possible to change the antenna to the Yagi type, which increases the gain to 10 dBi, but the antenna will be very large and unsuitable for the proposed application [56].

RF amplifiers: Using amplifiers in free space has been limited by Federal Communication Commission (FCC) to particular transmission power [57], but no rules have been introduced so far in the underwater environment.

3.2.1 Underwater electromagnetic characterisation experimental setup

To validate the theoretical results, the underwater communication range for two *SX1276-based* transceiver nodes at 868 MHz was evaluated. *SX12176* is a LoRa Long range low power transceiver by Semtech semiconductor [58], and it is the most commonly used transceiver in long-range communication. LoPy4 [59] is a compact *MicroPython* enabled radio node based on *SX1276* transceivers, designed to work at 868 MHz frequency. Other than LoRa transceivers, there are *Sigfox* and Wi-Fi and

Bluetooth on the board. Two identical characterisations platforms based on *LoPy4* nodes were prepared, which are shown in Figure 25. The LoRa module is configured with a frequency of 868 MHz, channel bandwidth of 125 kHz, spreading factor of 12, preamble symbols of 6 and transmission power of 14. These values are set based on the supporting longest range possible with the help of the article published by Mark Zachmann [60]. An *STM32F4-Disco* board [61] has been used to control the custom made *SX1276RF1IAS* modules, which have not been used in this test; it also connects to an external start switch to initiate the test procedure and synchronize the transmitter and receiver's start moment for logging purposes. An SD Card is used for logging the communication packets statistics. As these characterisation setups are meant to be immersed up to 5 meters deep in water, two IP68 plastic enclosures [62] were used as the containers, and silicon sealant materials were used to seal the antenna connectors and switch cut-outs. As shown in Figure 26, airtight bags were also used to cover the enclosure and antenna to provide an extra level of water protection. Using a 70 micrometer airtight plastic bag adds an extra layer of plastic between the antenna and water, which is inevitable. However, based on the practical experiments by Donmez [63] on 1 mm plastic material and another experiment demonstration at 10 GHz frequency on a range of plastic materials [64], the effect of a thin plastic layer is negligible.

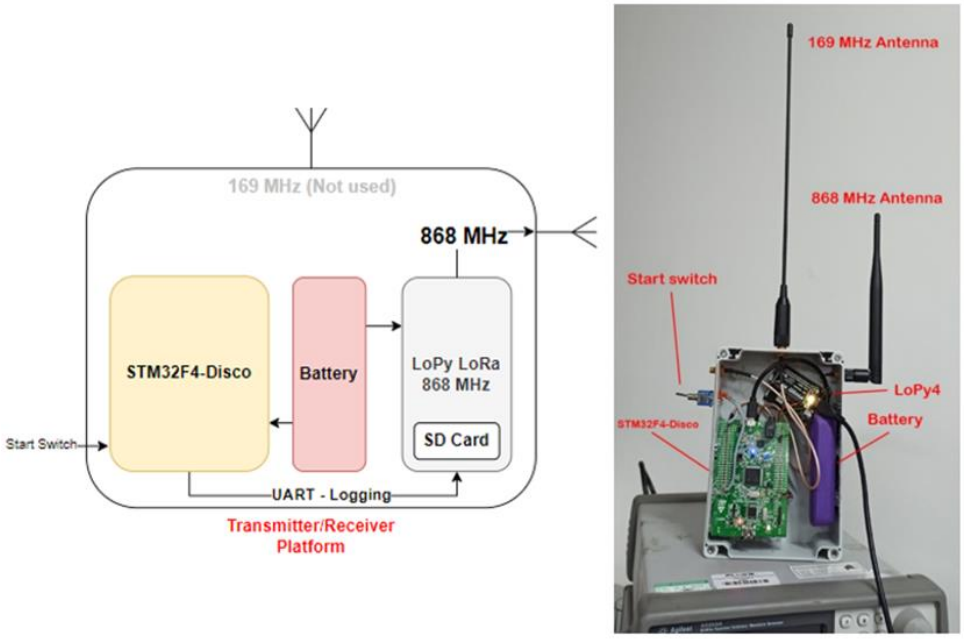


Figure 25 RF evaluation platform block diagram



(A) RF characterization boards fitted in a sealed container

(B) Containers wrapped in an airtight bag and installed on a rod

Figure 26 RF characterisation setup

Initially, an urban environment communication range test in free space has been performed to confirm that the modules were correctly configured. The non-line-of-sight urban communication test was carried out near *Tyndall National*

Institute [65] in *Cork* [51.898736, -8.483184]. In these tests, the transmitter characterisation node was installed on the second floor of a four-level building in the urban area and received signal strength was recorded while increasing the distance of transmission. In Figure 27, an aerial image of the test environment and the average RSSI is shown. The red line shows the path taken with the transmitter board. The LoPy4 868 MHz receiver node managed to receive the transmitter signals up to 240 meters away from the starting point, with no line-of-sight, with the presence of the dense and high buildings in between the transmitter and receiver and the transmitter located inside a four-level building. This indicates that the setup was working as expected, and there were no loose connections or deficiencies in the RF transceiver setup.

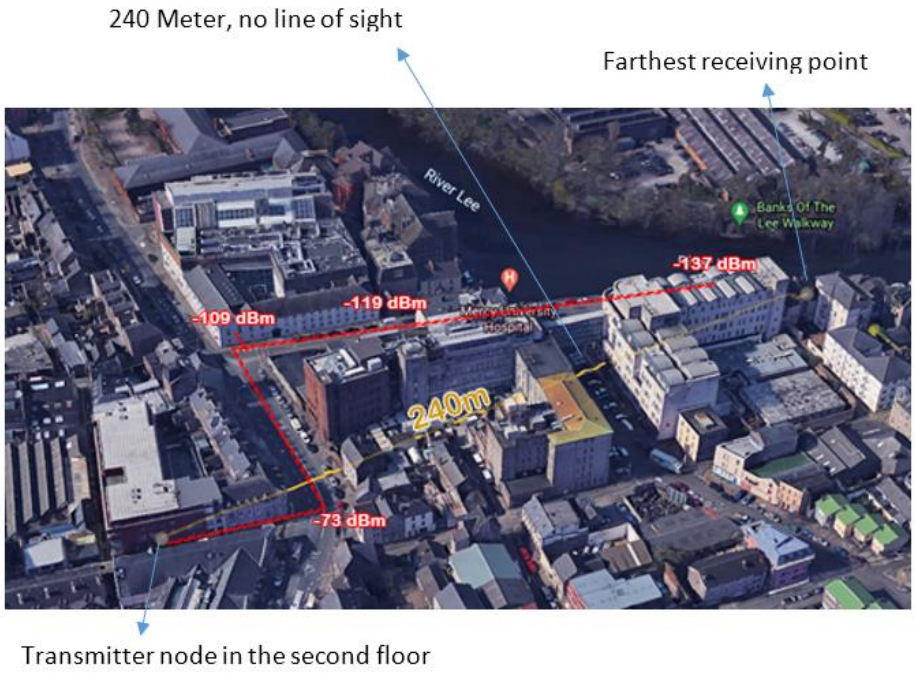


Figure 27 RF characterisation platform air communication test

After testing the communication in the air, an underwater test in the *River Lee* in Cork [51.898757, -8.483163] was performed. First, the salinity of the water was measured using a salinity refractometer. “Refractometers measure the degree to which the light changes direction, called the angle of refraction. A refractometer

takes the refraction angles and correlates them to refractive index (nD) values that have been established. Using these values, you can determine the concentrations of solutions" [66]. A salinity refractometer and its working principle are shown in Figure 28. The salinity of the River Lee water was measured, and it was approximately 0%, which means that it approximated a freshwater river at the time of measurement (the River Lee is tidal and experiences a saltwater column according to the tidal cycle [67]).

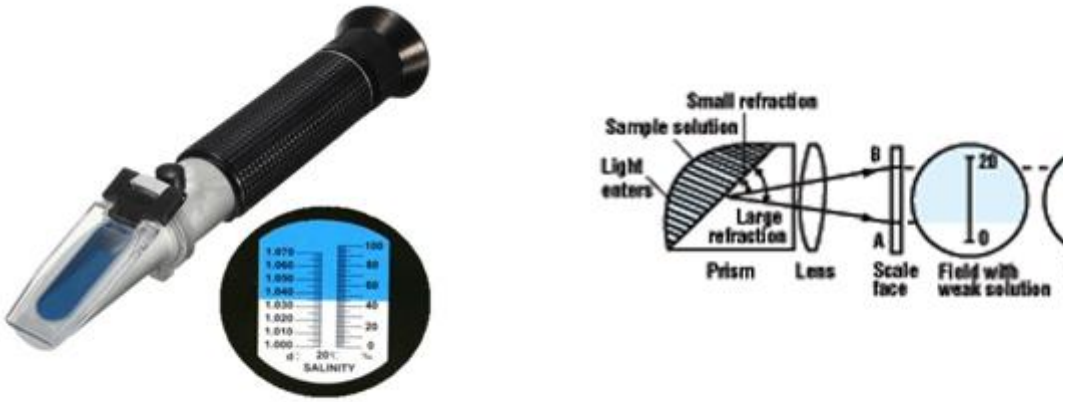


Figure 28 Refractometer and its working principal (adapted from [66])

In the test scenario, both receiver and transmitter were kept underwater while the receiver was recording the RSSI values. Then the distance between transmitter and receiver increased from 50 cm to 120 cm, as shown in Figure 29. At 50 cm, the average RSSI was -112 dBm, decreased to -120 dBm at 100 cm; however, at 100 cm, the percentage of packet drops increased significantly. At approximately 120 cm, the communications were significantly degraded, and the average RSSI of the limited received packets was -130 dBm approximately. These results are closely in line with the estimations that are discussed at the beginning of Section 3.2, where it estimated that the *SX1276* transmission range would be approximately 110 cm underwater.

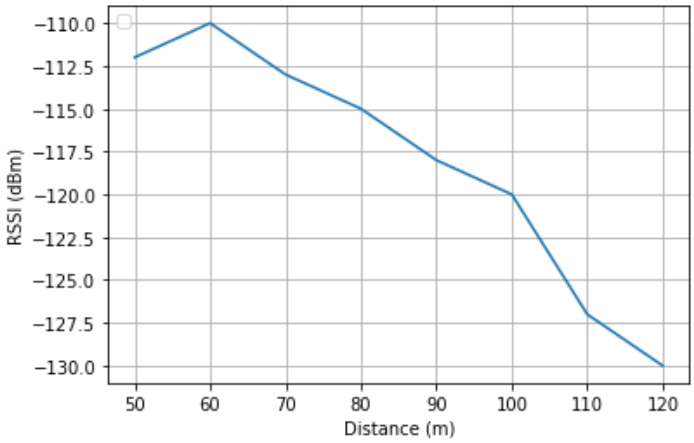


Figure 29 Distance vs RSSI Underwater

The experiment proved that RF communications underwater using high-frequency, high-power radio frequencies is not the optimal solution even at short range. It concludes that at 868 MHz, starting from 100 cm distance between transmitter and receiver, the signals start to get attenuated significantly, and a stable communication connection is not possible. Although these results are in line with the theoretical estimations, in practical deployments, as discussed at the beginning of this section, the signals might get more attenuated for a number of reasons, these include the transceivers antenna misalignment, refraction, diffraction caused by the environmental factors and also possible change of the river salinity as tidal changes were experienced [67]. By validating the theoretical results for underwater electromagnetic communication, it is concluded that the optimal solution for the IMPAQT sites would be using acoustic communication rather than electromagnetic communication except at very short ranges.

4 Underwater acoustic communication

Due to the fact that in most aquaculture sites, a longer-range communications system is required between the sensors and associated receivers, an ultrasonic telemetry platform was developed as an alternative to the short-range EM transceiver system described in Section 3.2.1. Sound waves can propagate through mediums by vibrating the molecules in the matter. Hence, sound waves can move through solids, liquids or gases. In solid materials, molecules are packed closely together, which results in sound waves travelling faster, while in gases where molecules are loosely packed, sound waves move slower. For instance, sound travels approximately four times faster in water compared to air [68]. The temperature of the medium also has an effect on the propagation of sound waves. In a hotter material, the molecules are moving, vibrating and colliding with each other more often, which results in an increase in the sound propagation speed. The parameters which impact on sound propagation are discussed in more detail in Section 4.1.

Sound waves can propagate in different modes depending on the medium properties in question, these are known as called "wave modes". There are three primary categories of wave modes: transverse, longitudinal, and surface [69]. In air and liquid, sound generally travels by means of a variation of pressure (compression and rarefaction) in the direction of the wave propagation. In this mode, which is called “Longitudinal Waves”, liquid or air molecules move back and forth in the direction of wave propagation [70]. In solid materials, it is possible to produce waves perpendicular to the direction of travel which are called “Transverse Waves”. In “Surface Waves”, the waves travel along the interface between two different mediums e.g., the air-substrate interface, and it can be considered as the combination of transverse and longitudinal moves [70]. There exists also the “Plate Waves” mode that is similar to surface waves which can only be generated in very thin (a few wavelengths thick) materials [69].

In this work, acoustic transducers are used to excite longitudinal waves in the water. As acoustic waves have low attenuation in water, they are commonly used for

underwater communication. Low-frequency acoustic waves can travel further when compared to high-frequency acoustic waves underwater, but their bandwidth is reduced when compared to higher-frequency acoustic waves. In IMTA sites and local monitoring applications, where there would be a receiver node close-by, it is possible to use high-frequency waves, this enables the tags to transmit more information in a given time, and it also increases the overall battery life of the nodes due to short transmission period and lowers power consumption associated with the use of high-frequency transducers. Regarding the size requirements, high-frequency transducers are also generally a smaller form factor. The receiver transducer, which is usually known as a hydrophone, needs to be immersed in water to capture the signals. Acoustic telemetry has been used in a wide range of applications, such as tracking the movements of fish in dams and rivers, water quality monitoring in seawater and freshwater environments [71]. An acoustic signal can propagate easily in both seawater and freshwater as it uses pressure waves instead of EM waves. Acoustic signals can travel from tens of meters to a few kilometers depending on the transducer size and transmit power. In comparison with RF communications, there are some drawbacks associated with underwater acoustic communications, such as high end-to-end delay, multipath propagation, Doppler spread, limited bandwidth, high bit-error-rate, and relatively higher current consumption [38].

4.1 Acoustic path loss model

The acoustic channel models are extensively discussed in [72]–[74]; in this section, an overview of a general underwater channel model will be discussed. This section has already been partly published in peer-review conference proceedings [75]. The ultrasonic wave produced by the piezo transducers is attenuated by two main factors in an aquatic environment, spherical spreading loss and absorption loss [73].

4.1.1 Acoustic waves spreading loss

If an acoustic beam was infinitely narrow, it only gets attenuated due to the absorption [73], however in a practical situation, as an acoustic wave propagates in any medium, it spreads in the medium and consequently loses its power as its area will increase by travelling in the medium [73]. Acoustic intensity can be defined using the following equation [73]:

$$I_a = \frac{W_a}{A} \quad 5$$

Where W_a is acoustic power in W, A is the surface area in m^2, and I_a is the acoustic intensity which in SI system is in W/m^2. Considering how the area increases with distance from the transducer, the relation between the intensity and the distance can be estimated. If a transducer radiates waves equally in all directions, the waves will spread spherically from it. Then the transmission loss due to the spherical loss can be estimated using the following equation [73]:

$$L_s = 20\ Log\ R \quad 6$$

Where L_s is the spherical transmission loss in dB, and R represents the distance from the source in meters.

4.1.2 Acoustic waves absorption loss

Another parameter that has an impact on ultrasonic transmission loss in water is absorption coefficient (α), which in this thesis measured in dB/km, and later used to estimate the total path loss. and it depends on two variables, viscous absorption and the chemical relaxation effect [76]. When a sound signal propagates in a medium with suspended particles, the motion of the particles caused by the acoustic waves produces heat via viscous drag. Hence, part of the vibration energy converts to heat, and this decreases the sound energy, and this is called viscous absorption [77]. Viscous absorption is significant at high frequencies (above 100 kHz). When an abrupt physical or chemical change happens to an equilibrated system, such as a sudden rise in temperature or pressure, it takes time for the system to re-

equilibrate under the new condition. The relaxation effect may be caused by a redistribution of energy in physical or chemical parameters, such as redistribution of energy among the atoms and molecules, and this is called the chemical relaxation effect. It can be studied in detail in [78]. The chemical relaxation frequency can vary for each substance. At the low-frequency range, up to a few kHz, boric acid chemical relaxation is the primary source of absorption [79]. For intermediate frequency bands, up to a few 100 kHz, magnesium sulphate chemical relaxation is the main source of absorption [76]. The IMPAQT transmitter described in this thesis uses an *AS-1* transducer, which can operate in a wide range of 1 Hz-100 kHz, and at this frequency range, viscous absorption and the magnesium sulphate chemical relaxation effect is seen to be significant [76]. Absorption coefficient (α) expressed in decibels per kilometer (dB/km) for boron and magnesium sulphate can be estimated by the following simplified equation [76] :

$$\alpha = 0.106\frac{f_1 f^2}{f^2 + f_1^2}e^{(pH-8)/0.56} + 0.52\left(1+\frac{T}{43}\right)\left(\frac{S}{35}\right)\frac{f_2 f^2}{f^2 + f_2^2}e^{-z/6} + 0.00049 f^2 e^{-\left(\frac{T}{27}+\frac{Z}{17}\right)} \quad (7)$$

Where f is the transducer frequency in kHz, T is the temperature in °C, Z is depth in km, and S is the salinity in parts per thousand (ppt). f_1 and f_2 are the relaxation frequency for boron and magnesium sulphate in kHz, which can be estimated as below:

For boron
$$f_1 = 0.78\left(\frac{S}{35}\right)^{\frac{1}{2}} e^{\frac{T}{26}} \quad (8)$$

For magnesium
$$f_2 = 42e^{\frac{T}{17}} \quad (9)$$

The absorption coefficient in dB/km relative to piezo frequency is shown in Figure 30 with T = 8 °C, S = 35 ppt, Z = 0.050 km, pH = 8.1.

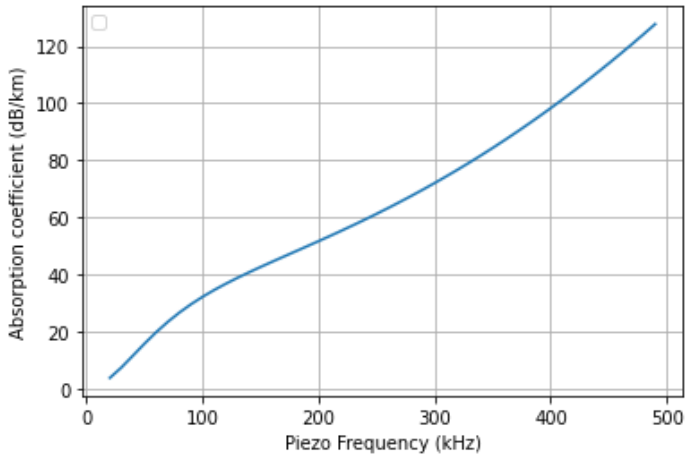


Figure 30 Acoustic absorption coefficient

In the proposed design and operating environment, f = 42 kHz (Piezo resonance frequency), T = 8 °C (water temperature), S = 35 ppt (seawater salinity), pH = 8.1 (current ocean pH level [80]), and Z = 50 m (estimated working depth). An absorption coefficient of 12.3 dB/km has been estimated for an infinitely narrow acoustic beam; however, as discussed before, practical beams spread spherically as they propagate through the water. Hence, Equation 10 can be used to establish the transmission loss (L_t) in dB at the distance of R considering absorption coefficient (α) described in Equation 7, and spherical spreading loss (L_s) described in Equation 6 [73]:

$$L_t = L_s + \alpha R, \qquad 10$$

In the IMPAQT project, a maximum distance of 100 m is considered between the transmitter and receiver nodes, according to envisaged user requirements on IMTA sites, which leads to an overall transmission loss of 41.2 dB at 100 m. There is an online absorption coefficient calculator provided by the *National Physical Laboratory of the United Kingdom* that can be used to estimate the absorption coefficient [81]. In Figure 31, the transmission loss versus distance from the transmitter at 42 kHz is shown. In Figure 32, the transmission loss versus piezo frequency at 100 m is shown, which indicates that by increasing the piezo frequency, the transmission loss would increase.

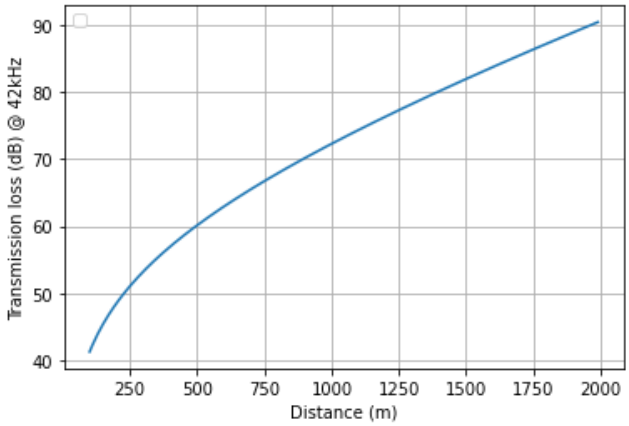


Figure 31 Acoustic transmission loss vs distance at 42 kHz

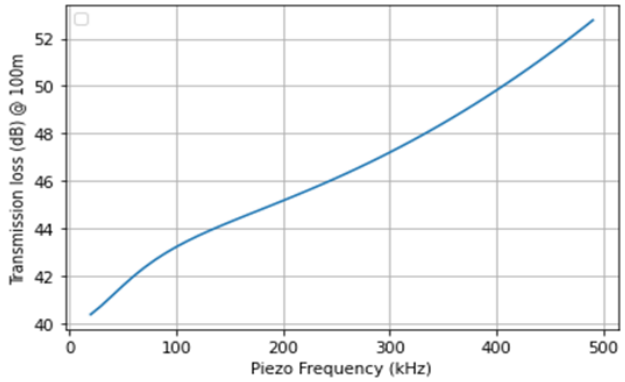


Figure 32 Acoustic transmission loss vs piezo frequency at 100 m

Considering the transmission loss shown in Figure 31 and Figure 32, to achieve the desired communication range, the transmitted signal amplitude should be adequate to provide enough sound pressure in water for the waves to propagate. This is discussed in Section 4.2.2. There are alternative methods to increase the communication range. For instance, Ghaffarivardavagh et al. [82] discussed the usage of ultra-wideband underwater backscatter nodes built using piezoelectric metamaterials to extend the communication range of underwater transmitter nodes.

4.2 IMPAQT Acoustic Transmitter Prototype

As discussed in Section 1.3, the IMPAQT telemetry platform consists of transmitters and receivers for sensor data collection. Transmitters need to be **miniaturized**, **low-power,** and **low-cost**, and they must be easily attachable to other sensors. There are no commercially available transmitter nodes with the mentioned specifications in the market to perform one-way acoustic communication and modulation. As a result, to meet project requirements, a miniaturized acoustic communication system was designed and evaluated. To design such a platform, various factors need to be considered.

Frequency range: As discussed in Section 4.1, acoustic signal propagation in water is mainly affected by the frequency of the transducer. This factor will limit the operating frequency range of the transducer.

Transducer Power: In a high-performance transducer, the transducer power input has a direct relation with the water pressure produced. The water pressure has a direct relation with the resulting waves travelling distance. In simple terms, with higher electrical power applied to a transducer, a higher transmission range can be achieved. Transducer specifications limit the maximum electrical power that the transducer can handle. In electrical systems, Power (P) in W is equal to Voltage (V) in V multiplied by the amount of current (I) in A. The power can be increased by either increasing the voltage or the current [83].

$$P = V \times I \tag{11}$$

In piezoelectric systems, the I is controlled by the piezo materials depending on the voltage applied to their terminals. To have an adequate acoustic intensity, in this case, the voltage needs to be increased, which is a challenging task in a miniaturized battery-powered device where there is a limitation on the number of battery cells that can be used. Generally, a boost converter is used as a solution to increase the voltage in battery-powered devices. A boost converter (Step-Up converter) is a circuit that can step up the voltage to a controlled level. The

maximum voltage is limited by the inductor size and the boost converter controller capabilities, which will be discussed later in this section.

Receiver transducer: On the receiving side, a high-quality receiver, which in an underwater context is called a hydrophone, is required to capture the weak acoustic signals. Receiver sensitivity is an important property of the hydrophones that needs to be considered; receiver sensitivity is measured in dBV/µPa. Also, working frequency and response are other important factors in hydrophones; they are usually depicted in a graph showing the receiver sensitivity across a frequency range. In simple terms, better receiver sensitivity will result in better signal detection and improve the communication range [84].

An ultrasonic transmitter node usually consists of an underwater transducer, generally a piezoelectric material, a transducer driver, a controller, and a boost converter to step up the battery voltage. In the remainder of this section, each node's element is discussed.

There were various possible solutions to these problems; hence, characterisation prototype boards were designed, which included various methods to evaluate the different factors involved in the prototype design, such as miniaturized booster circuits, modulation and demodulation techniques and power consumption involved. In the rest of this section, the procedure used to study and design the prototype of the transmitter node characterisation board is described. The design diagram of the IMPAQT transmitter node prototype board is shown in Figure 33. In the rest of this subsection, each block is described, and the design method is discussed.

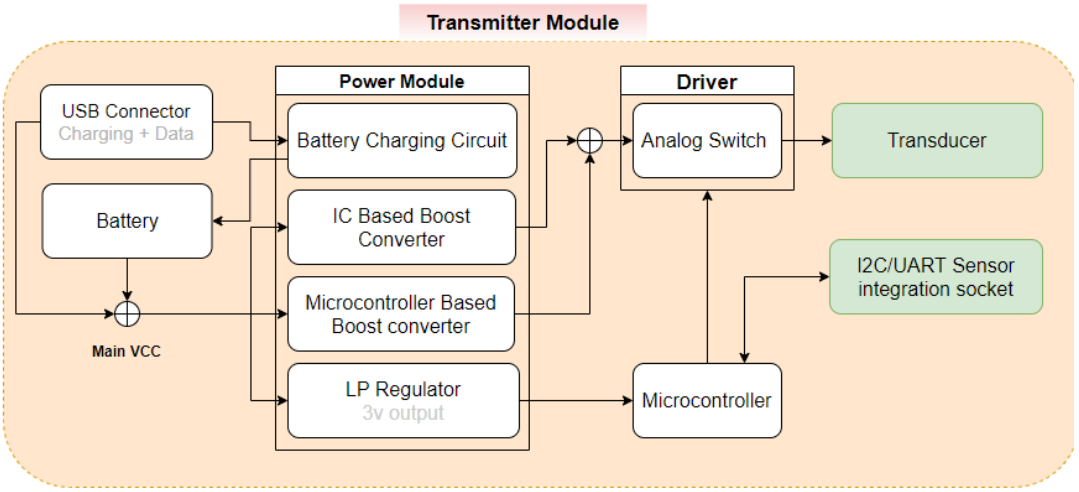


Figure 33 IMPAQT Acoustic transmitter prototype board block diagram

4.2.1 Acoustic transducers comparison and selection

Hydrophones are similar to microphones but for underwater environments, and they convert acoustic waves into electrical currents that can be used to receive underwater acoustic signals in the electronic boards. Hydrophones are generally made with piezoelectric material that converts mechanical displacements into electrical currents. PZT materials are one of the most widely used piezoelectric materials, and they have been used in different applications, in particular as fish tags [20][85][86]. In [87], four types of PZT materials' (Customized Type VI, Type VI, Type I, and Type II) energy consumption, source-level, and frequency response has been compared. They have used various PZT ceramic tubes, *PZT508* is a modified Type VI piezo from *Morgan Electroceramics* [88]. *Pz21* is Type VI piezo material from Ferroperm Piezoceramics. *EBL1* and *EBL2* are piezo Type I and Type II respectively from *EBL* company [89]. As it is shown in Figure 34, PZT Type VI consumes more energy compared to other types. But they also provide better source level (shown in Figure 35) and frequency response (shown in Figure 36) compared to others. From the energy consumption aspect, PZT Type I and II consumes the least amount of energy per transmission compared to other types, but they provide lower source level and frequency response compared to others.

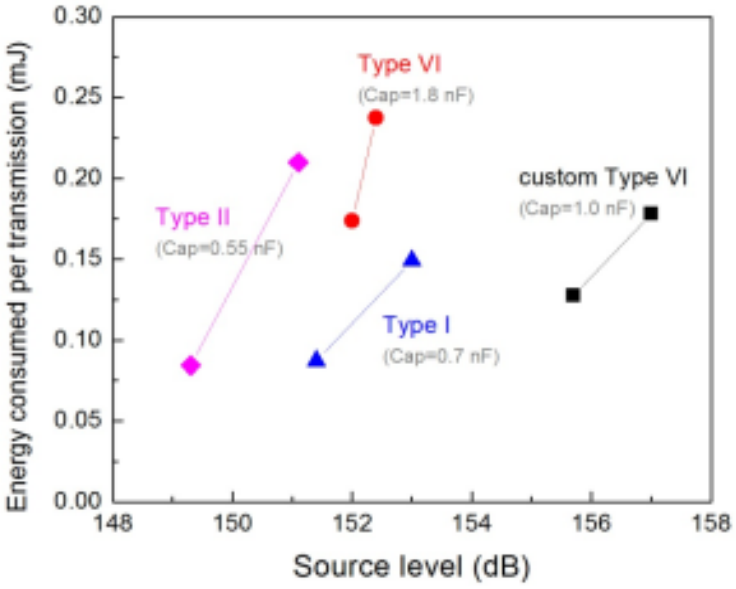


Figure 34 Energy consumption as a function of source-level for PZT materials (adapted from [87])

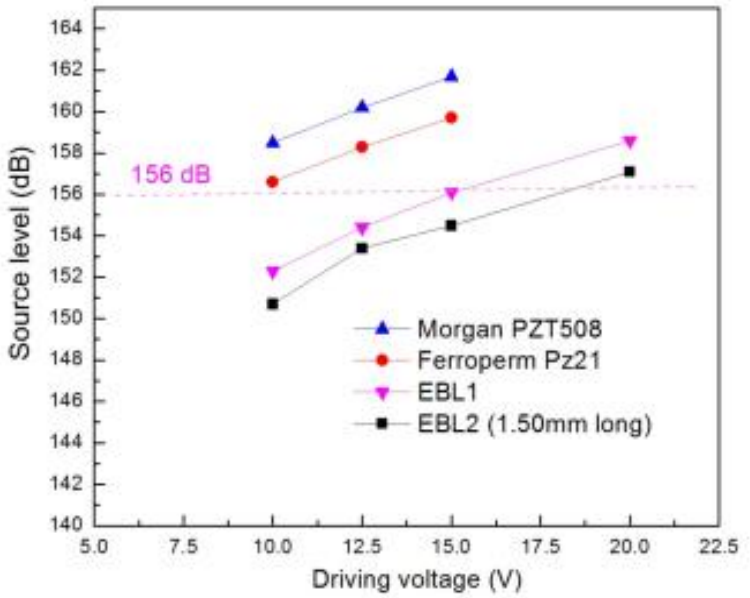


Figure 35 Voltage responses of PZT tubes of different material types (adapted from [87])

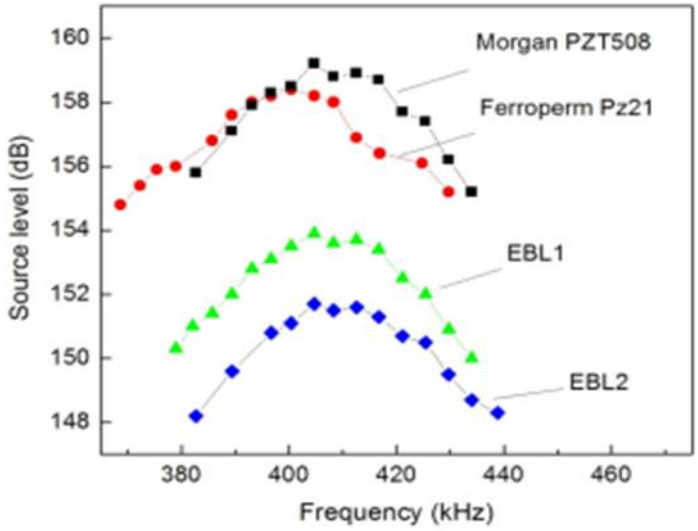


Figure 36 Frequency responses of PZT tubes of different material types (adapted from [87])

As a result of the above comparison and also the availability of off-the-shelf hydrophones, five commercial hydrophones have been considered, shown in Table 3. From the provided list, for the receiver side, *BII-7003* has been selected as it covers a wide range of frequencies, virtually enabling the possibility of research on various miniaturized transducers. It also has reasonable sensitivity and working depth. *BII-7003* is shown in Figure 37. For the transmitter side, *AS-1* [90] from *Aquarian Scientific* has been selected. It is able to transmit in a wide frequency range of 1 Hz to 100 kHz. It has a compact size with an excellent operating depth of 200 m. It is important to note that *AS-1* can work as a transmitter and receiver.

Table 3 Available commercial hydrophones

Manufacturer Part number	**Frequency range**	**Sensitivity** (dB re 1 V/µPa)	**Working depth** (m)	**Type**
SQ42-00 [91]	1 Hz to 400 kHz	-216	3500	Not available
BII-7003 [92]	1 Hz to 560 kHz	-211	400	Type I
AS-1 [90]	1 Hz to 100 kHz	-208	200	Type II
H3 [93]	10 Hz to 100 kHz	-192	80	Type II

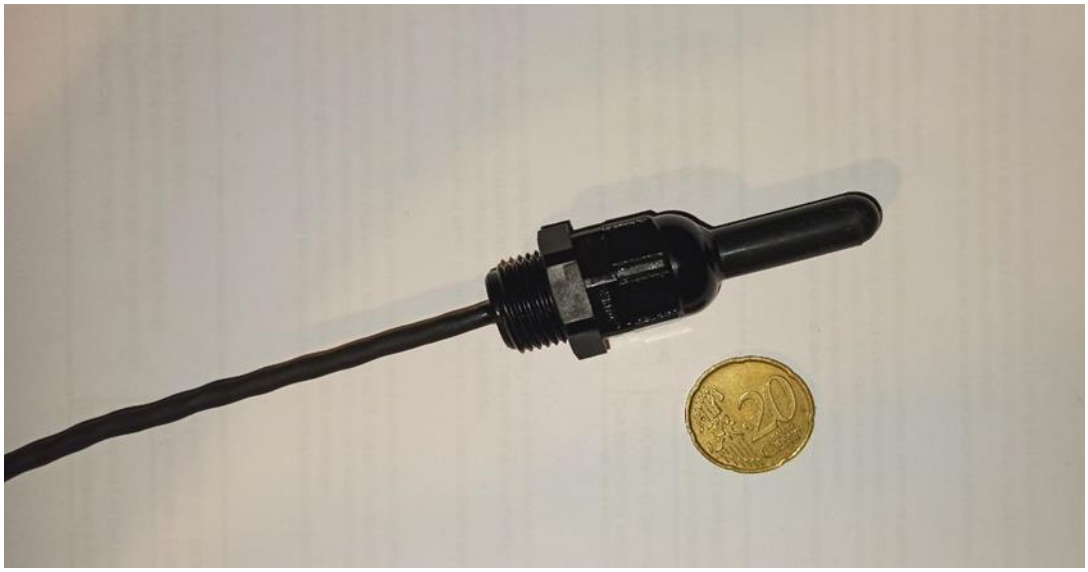


Figure 37 BII-7003 hydrophone

There is also the possibility to fabricate the transducer from piezo tubes. In that case, it would be possible to achieve a more compact transducer and transmitter node design by fabricating the transducer. However, it requires special manufacturing materials and calibration tools. In Table 4, various compatible piezo tubes are listed that can be used in the fabrication process of a transducer. SMC3H3F380 piezo tubes are shown in Figure 38. The fabrication process is extensively discussed in [94]. The listed piezo materials information can be found on the manufacturer's website [95].

Table 4 Piezo tubes

Manufacturer part number	**Frequency kHz**	**Outer diameter (mm)**	**Inner diameter (mm)**	**Length**	**Electrical Capacitance CS**
SMC3015T4410	520	3	1.5	4	350 pF
SMC3H3F380	380	3	-	3	70 pF
SMC26D22H13111	42	26	22	13	6600 pF



Figure 38 SMC3H3F380 Piezo transducer

4.2.2 Boost converters

The *AS-1* transmitter's transducer [90] is designed to operate up to 30 V peak to peak; however, the transmitter node is designed to run on a LiPo battery with a nominal voltage of 3.7 V. To provide an adequate ultrasonics sound energy level, a voltage booster circuit is required to boost the voltage to higher values. A voltage booster circuit, or boost converter, also known as a step-up converter, is a DC-to-DC power converter that increases the input voltage to the required output voltage of 20 V. Voltage boosters are a subset of switched-mode power supply that requires four main components, a diode, a transistor, and an energy storage element which usually consists of a capacitor, an inductor, or the combination of both. The boost converter circuit also requires a controller. The voltage controller receives feedback from the output voltage of the booster circuit so as to control the voltage level to be at the pre-defined level (20 V). The controller controls the voltage level of the booster circuit using an electronic switch. The working principle of the booster circuit is shown in Figure 39. By closing the switch, the current flows through the inductor, and the inductor stores energy by generating a magnetic field. When the controller turns

off the switch, the current flow stops. The energy that was stored in the inductor as a magnetic field creates a secondary power supply that will be used to charge the subsequent capacitor through the diode [96]. This procedure charges the capacitor frequently and results in higher voltage on the capacitor that later will be used to drive the acoustic transducer. The boosting procedure is shown in Figure 39.

To select the appropriate components for the boost converter, it is essential to estimate the current required for driving the hydrophone at the maximum power. As stated in the *AS-1* technical specifications [90], the maximum voltage that *AS-1* can handle on its input is 30 V peak to peak, which means that it can be supplied with up to 30 V if the other terminal is connected to the ground (0 V). However, having a voltage over 25 V requires capacitors in the voltage range of 50 V, which are bulky. Hence, it has been decided to use 20 V as the driving voltage level. It is 5 V less than the maximum voltage of the capacitors, and it provides a safe margin in case of a high-voltage ripple when driving the transducer.

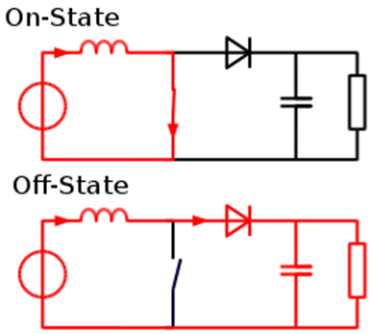


Figure 39 Circuit analysis of Boost Converter (adapted from [96])

The average current of the piezo transducer can be estimated by Equation 12 [97] :

$$I_{Avg} = \frac{2Q}{T_s} = 2CVf \qquad 12$$

where Q represents the charge in the piezoelectric transducer, T_s represents the period of the driving signal, C represents the static capacitance in Farad, V represents the driving voltage, f is the signal frequency. In the IMPAQT transmitter context, C = 5 nF (*AS-1* static capacitance[90]), V = 20 V (*AS-1* transducer driving voltage), f = 42 kHz (the modulation frequency). Using the parameters of the selected hydrophone and desired frequency, the average current would be about 8.4 mA while transmitting at the highest sound level. In Figure 40, the average current for the *AS-1* transducer is shown at different frequencies.

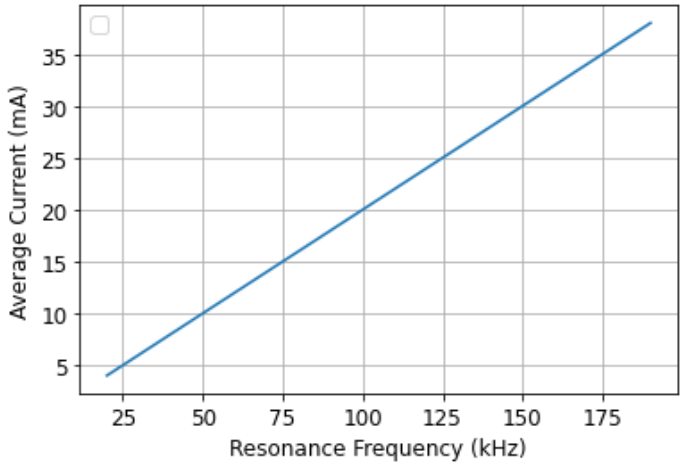


Figure 40 Average current of AS-1 transducer at 20 V

From Figure 40, it can be inferred that up to 100 kHz, which is the maximum working frequency for an AS-1 transducer, the maximum current is less than 35 mA. It is important to note that this is the current drawn from a 20 V power source. In the system design of the IMPAQT transmitter node, 100 mA will be used as the required driving current hereafter, and it is marginally higher than the required current, which makes it possible to use other transducers if required. It also provides a safe margin for the driver's current supply while driving the transducer.

Considering the current and voltage requirements, a list of possible candidates for the transmitter boost converter design is listed in Table 5. In boost

converters, switching frequency has an inverse relationship with output capacitor size and inductor size. Higher switching frequency requires a smaller capacitor and inductor. However, a higher switching frequency increases the time required to reach the desired voltage level. The mechanism and considerations associated with selecting the optimum switching frequency are provided in [98].

Table 5 Boost converter controllers candidates

Name	Switching Frequency	Vin (Min-Max)	Vout (Min-Max)	Current (Max)	I supply (µA)	I shutdown (µA)	Footprint area (mm^2)
LT8337 [99]	300 kHz-3 MHz	2.7-28	26	5 A	15	0.3	9
MAX1771 [100]	300 kHz	2-16.5	2-100	2 A	110	5	28
TPS61040 [101]	1 MHz	1.8-6	1.8-28	0.4 A	28	1	4

Among the candidates compared in Table 5, the LT8337 boost converter is the versatile option. It has an internal switch that facilitates the usage in a design. It provides 28 V as the output voltage, which meets the required voltage of 20 V. In addition, its PCB footprint area is 9 mm^2, and it is slightly larger than the TPS61040, but considering the current supply and integrated switch, it offers the best current to footprint ratio. The *MAX1771* has the largest footprint area, and it requires an external FET switch. *Max1771* boost converter controller was selected for the first prototype board due to three reasons, (a) component package type makes it easier to solder/desolder for testing and debugging purposes, (b) it supports up to 100 V, which makes it a perfect choice for evaluating various hydrophones (c) it can supply up to 2 A current, which allows testing various hydrophones and configurations. In Figure 41, the circuit for the boost converter is shown. The MainVCC terminal is supplied by the battery, ranging from 2.5 V to 3.7 V, and it is connected to the inductor. There is a MOSFET switch (*IRLML6344* [102]) to drive the current through the inductor. The *MAX1771* control the MOSFET switch as described earlier to induce a magnetic field around the inductor, which then will be used to charge a 100 uF tantalum capacitor. Tantalum capacitors have a much higher capacitance for their

size; however, they are more expensive. The desired output voltage for the boost converter can be selected using the two feedback resistors (R4=R2, R5=R1) using Equation 13; where Vref = 1.5 V and R6 can be in the range of 10 k to 500 kΩ.

$$R4 = R6(\frac{Vout}{Vref} - 1) \qquad 13$$

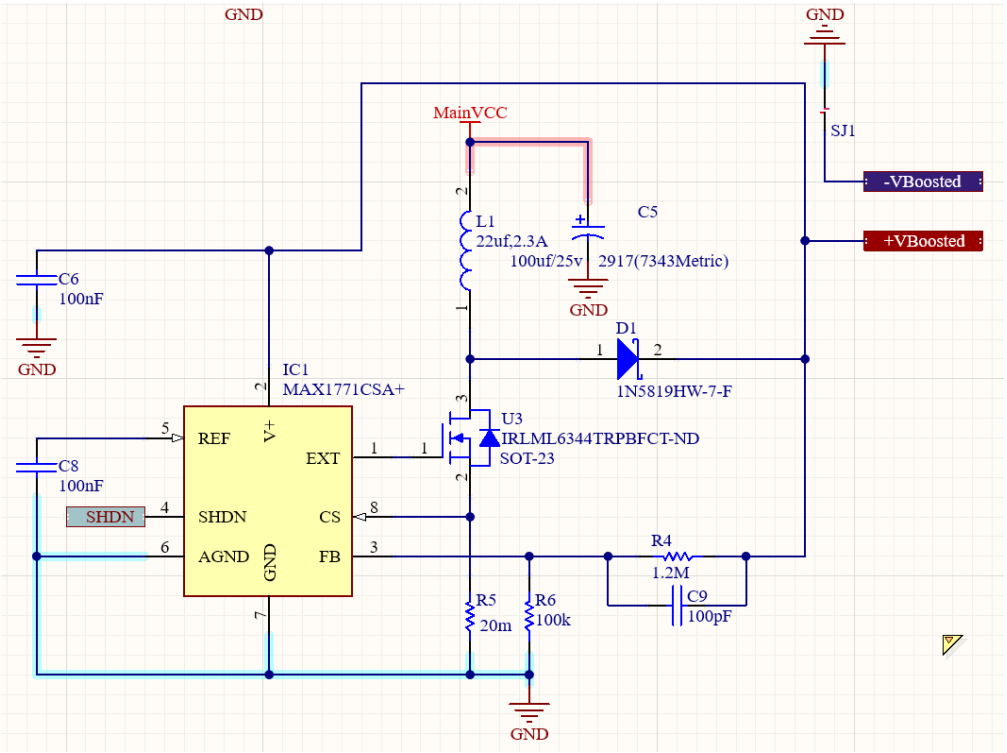


Figure 41 Boost converter circuit

In the *MAX1771* component's datasheet [100], it is suggested to use 22 µH for the inductor [100], and it is recommended that a design should follow the manufacturer recommendations [103]. A large value for the inductor results in a slower start-up time, which is the time it takes for the boost controller to reach the desired output voltage. A smaller value inductor will result in faster start-up time, however, it causes high-frequency noises and significant ripples in the output. A detailed explanation of the inductor, capacitor and diode selection criteria is

described in [103]. The above circuit design will provide up to 20 V and 600 mA current, which is sufficient for driving the *AS-1* transducer.

In addition to the off-the-shelf boost converter controllers, there is the opportunity to control the boost converters circuit using a microcontroller. In the prototype block diagram (Figure 33), this circuit is shown as the "Microcontroller based boost converter". In the IMPAQT transmitter node design,a shared-inductor dual-boost technique is used to provide higher voltage in a shorter time. Shared inductor boosting requires a precise switching timing of the MOSFETS for high-side and low-side in order to avoid short circuits when both MOSFETS are in the saturated mode (also known as shoot-through). The implemented dual-boost converter is shown in Figure 42. At the beginning (T_0), U4 and U5 are in the on state, and there is a current flowing in the inductor; at T_1, U5 turns off, causing an inverted polarity high-voltage induced on the inductor, which results in a current flowing through D4 and charges the corresponding *+VBoosted* capacitor. At T_2, both U4 and U5 turn on, resulting in current flowing in the inductor again; At T_3, U4 turns off, resulting in an inverted polarity high-voltage induced on the inductor, which will be in series with the circuit ground and will charge corresponding *-VBoosted* capacitor. The circuit implemented, and control of the the MOSFETs with the microcontroller was attempted, but as soon as running the test code, the MOSFETs were burning. After investigations, it was found that a MOSFET shoot-through protection circuit should have been included. The shoot-through protection circuit protects the MOSFET from burning by turning it off as soon as the flowing current passes a pre-set amount. This flaw in design resulted in a non-functioning circuit. On the other hand, adding the shoot-through protection circuit will add several components to the circuit, resulting in a larger circuit. Thus, off-the-shelf controllers (*MAX1771*) were used, which includes all the protection and control circuits on a tiny controller.

There is a voltage feedback circuit on the board to measure the boosted voltage using the onboard microcontroller. This circuit is a conventional voltage divider circuit, with the resistor values of 2.2 MΩ in series with the boosted voltage

and 220 kΩ resistor pull-down resistor. The resistor values are chosen so as to have the lowest possible current leakage with a good immunity against noise. This circuit will consume 1.52 µA when the device is in sleep mode and 8.2 µA when the voltage is boosted to 20 V, according to the simulations.

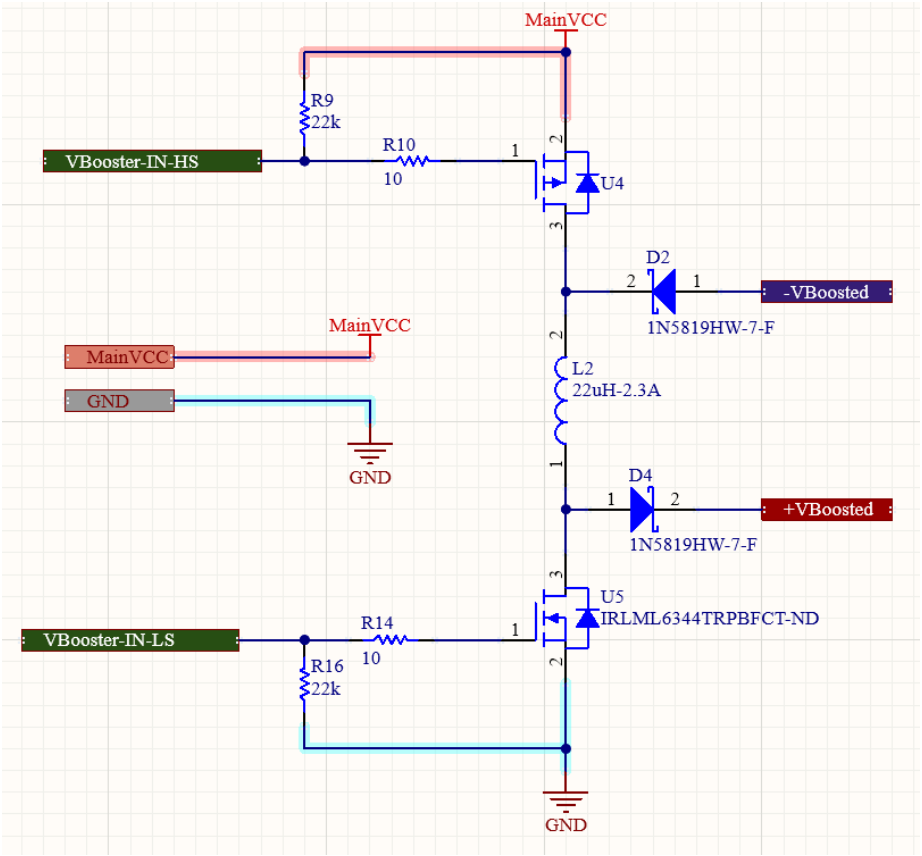


Figure 42 Microcontroller Based Dual-Boost converter

4.2.3 Transducer driver

To implement the required modulation scheme, it is necessary to drive the boosted voltage on the piezo transducer pins and alter the applied voltage according to the modulation scheme. A modulation scheme can be implemented on the microcontrollers, but driving the transducer cannot be done via the microcontroller directly, as the microcontroller's supply voltage for the pins is fixed at 3.3 V or 1.8 V (depending on the microcontroller supply voltage), and a microcontroller cannot deliver a high-current pulse that is needed for driving the hydrophones. The solution

is to use an intermediate component between the transducer and microcontroller, which can receive the modulation signals from the microcontroller and deliver it to the transducer at the required voltage and current levels. There are several solutions to this problem, such as H-Bridge driver ICs, H-Bridge transistor circuits, and analog switches. H-Bridges are made from electronic switches, such as MOSFETs and transistors, and they are used to supply electronic loads, such as motors and transducers. They can alter load current polarity and voltage as required. The transistors (Q1, Q2, Q3, Q4) in Figure 43 are controlled indirectly by the microcontroller, and M in the centre of each H-Bridge is a load (i.e., motor), which is a transducer in the transmitter node use-case. When Q1 and Q4 turn on, the current flows from Q1 to Q4, and when Q3 and Q2 turn on, the current will flow from Q3 to Q2. This variation in current will result in applying different voltage polarities on the load [104], which is a desirable requirement in driving acoustic transducers. However, the main problem with H-Bridge is that they are mainly developed for driving motors and to handle high current flows, which is not necessary for an acoustic transducer driving use-case. Electronic switches (e.g., analog switches) use the almost same principle as h-bridges but in a more compact fashion, and they can connect directly to the microcontroller. They handle fewer currents in a range of 100-500 mA, which is suitable for driving the *AS-1 transducer*.

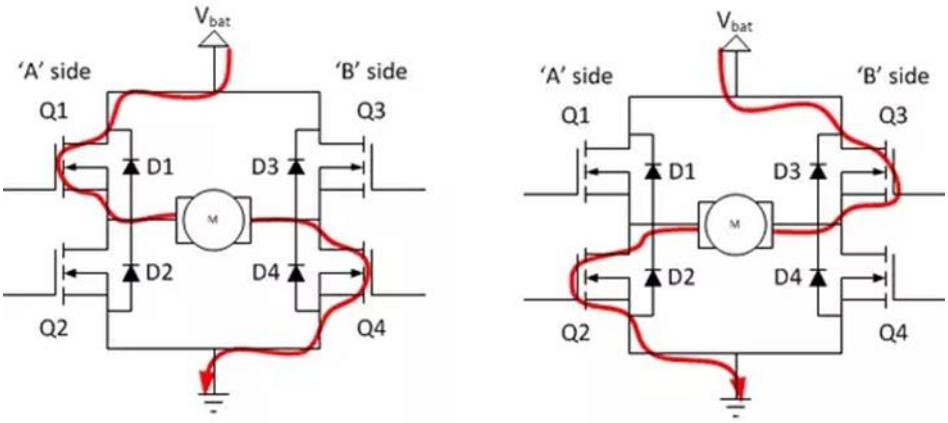


Figure 43 H-Bridge diagram (adapted from [104])

In Figure 44, a simplified structure of an analog switch is shown. As it can be seen, the structure of the analog switch is similar to the H-Bridge. Both include two switches for each terminal (Out). However, the analog switch uses a combination of a P-Channel MOSFET and N-Channel MOSFETs and a current buffer, which makes it possible to connect directly to a microcontroller. Analog switches control pins can be connected directly to a microcontroller. It is important to note that an analog switch can handle significantly less current, which in the IMPAQT project use-case is fine as it meets the 100 mA required current for driving the *AS-1* transducer.

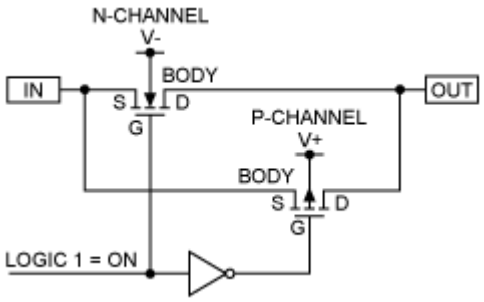


Figure 44 Analog Switch internal components (adapted from [105])

In the IMPAQT transmitter node developed, the *ADG1436* analog switch from Analog Devices [106] was used. *ADG1436* is capable of handling 600 mA of continuous current passing through, and its footprint is only 16 mm^2. The circuit diagram for *ADG1436* is shown in Figure 45.

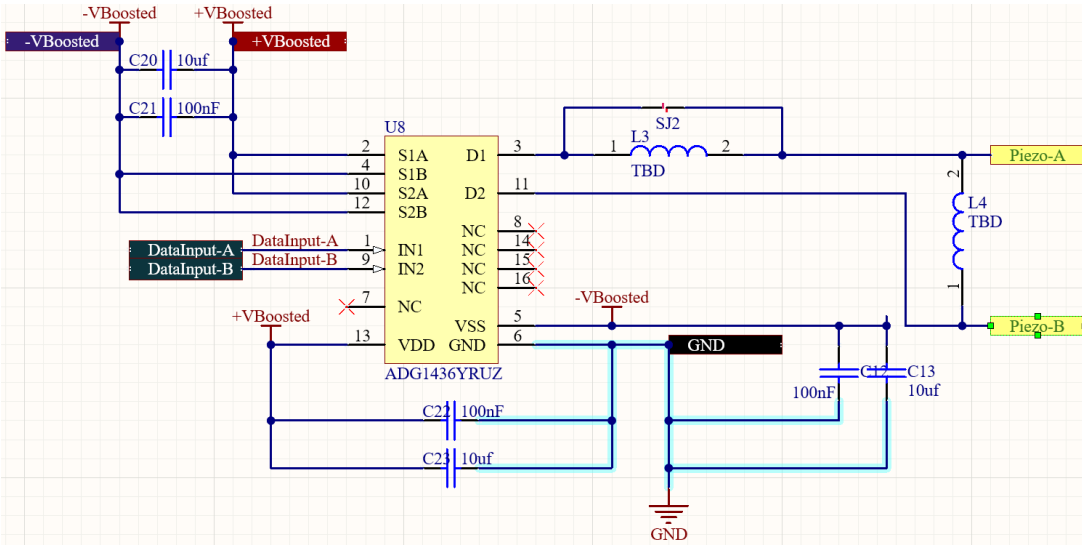


Figure 45 ADG1436 schematic

Two complementary Pulse-Width-Modulation (PWM) signals are connected to the control pins (IN1, IN2) to provide the modulation scheme waveform. The L3 inductor placed in series with the piezo can reduce the impedance it presents to the driving source and increase the power transfer. Since the piezo transducer is mainly a capacitive load, an inductor can reduce the capacitive reactance by resonating at the piezo frequency. The L4 also serves the same purpose of increasing the power applied on the transducer by acting as a parallel inductor to the piezo transducer. However, L3 and L4 inductors are not fitted on the manufactured board, as they were meant to be fitted if impedance matching was required.

4.2.4 Microcontroller selection

Among various microcontroller manufacturers, *ST Microelectronics* provides the widest range of microcontroller selections, from tiny 8 bit microcontrollers to advanced 32 bit dual-core *ARM* microcontrollers. In Figure 46, the *STM32* microcontroller's product families are shown. *ST Microelectronics* provides a complete set of free tools to develop, test, and debug firmware. As the transmitter node needs to be low-power, the Ultra-Low-Power family provided by *ST Microelectronics* would be a suitable choice. The Ultra-Low-Power family provides

various options regarding the processor architecture selection, from the basic M0 to the advanced M4 family. The differences between M0 to M4 families are the feature-set that the microcontroller provides. For instance, in the M0 family, there is no Floating-Point Unit (FPU) unit, while the M4 family includes the FPU unit, which enhances the floating-point operation's speed.

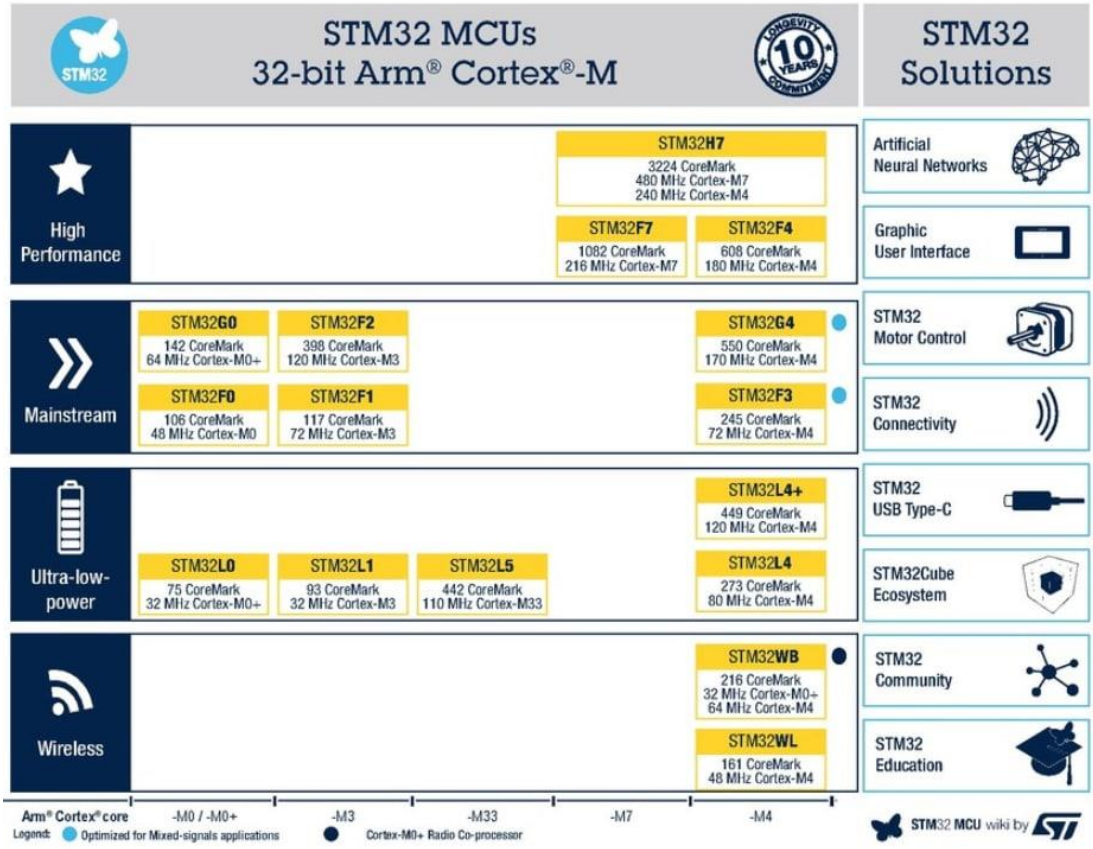


Figure 46 STM32 Microcontrollers family (adapted from [107])

The decision criteria for selecting the suitable microcontroller for the transmitter node is as below:

Pin Count: In the transmitter node prototype board, at least 23 pins were required to evaluate various subsystems. The closest microcontroller package with at least 23 pins is TQFP-32 based microcontrollers, which are rectangular with eight pins on each side of the microcontrollers.

Timers: The board needed at least three advanced timers with output ports. One with two channels for controlling the customized boost converter circuit, one timer for controlling only the low side of the customized boost converter, one with two complementary output channels to produce modulation scheme waveforms.

Analog to digital converter: It was decided to monitor both *"-Vboosted"* and *"+Vboosted"* voltage levels to ensure that the boost converter has boosted the voltage to the required level. To monitor these levels, two channels of ADC were necessary. There are also three auxiliary ADC inputs on the board to provide an extra integration option for analog sensors.

Low power consumption: Being low-power is a critical requirement for the IMPAQT transmitter. Hence, It was decided to use the *STM32L* series. They offer very one of the low power consumption microcontroller series in the market.

Considering all the above criteria, *STM32L082KZT*, a TQFP-32 package microcontroller, is one of the microcontrollers which meet all the requirements, and it has a minimal package and cost.

4.2.5 Transmitter battery and power circuits design

The IMPAQT transmitter nodes are running on 1/*LP503562* [108] batteries. The battery is a 3.7 V battery with a 1200 mA capacity. The battery dimensions are 63 mm L x 3.5 mm W x 5.6 mm T. Battery voltage generally depends on the discharge capacity profile of each cell; in LiPo batteries, the nominal voltage is 3.7 V, and the discharge profile is shown in Figure 47 [109]. The lines represent the discharge current. As it can be inferred from the figure when the cell is fully charged, the voltage is approximately 4.2 V, and when it completely discharges, the voltage reaches slightly above 3 V. Due to the voltage variation of the battery cell, it is required to have a regulator circuit in the transmitter node to stabilize the voltage at a specific value.

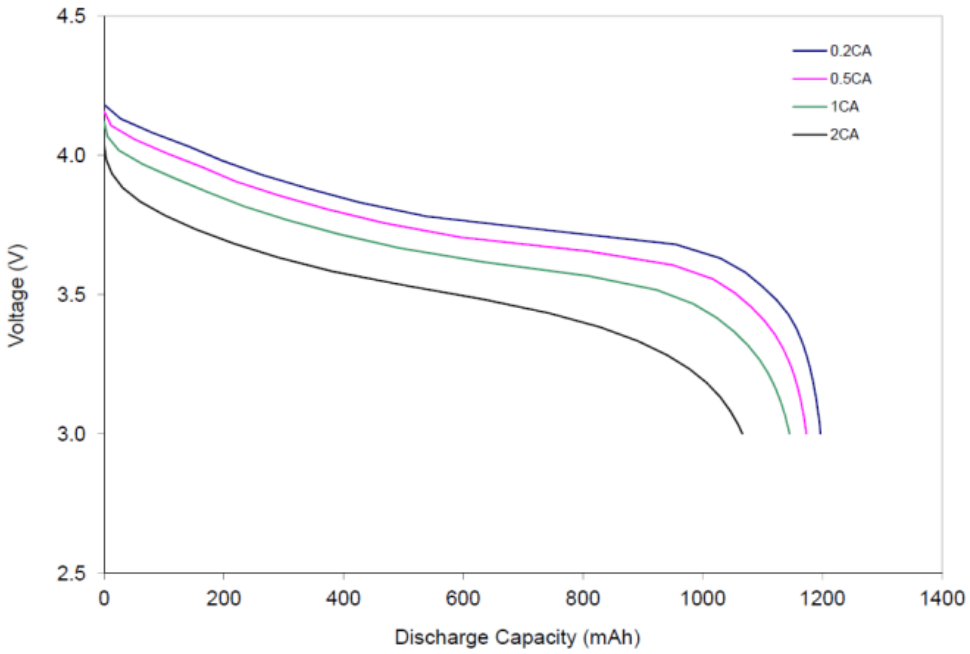


Figure 47 LPP 503562 Discharge Profile (adapted from [109])

There are a variety of voltage regulators in the market. The main criteria for the transmitter node are footprint size and quiescent power consumption. *TPS78230DDCT* [110] provides a low dropout voltage of 130 mV at maximum load and exceptionally efficient 500 nA quiescent current in a tiny SOT-5 footprint. It can supply up to 150 mA, and it has a 3% accuracy under maximum load [110].

4.2.6 Modulation methods comparison and selection

An input data needs to be modulated with carrier waves in ultrasonic communication systems to propagate in a medium efficiently. It is possible to send the data in a medium without a carrier wave; however, it requires a big transducer and strong amplification to be able to transmit it. Hence, in modern communication systems, a carrier wave is used to carry the information. Carrier waves don't have information on their own, and they should be modulated with the input data to carry the information. In this subsection, the three most famous modulation schemes will

be discussed, and the reason for selecting the On-Off-Keying (OOK) as the modulation scheme for the IMPAQT transmitter explained.

A) FSK

In FSK modulation, the data is transmitted through a variation of the carrier frequency. Several carrier frequencies can be used to indicate different symbols. The simplest FSK is binary FSK (BFSK), which uses only two distinct frequencies to transmit binary information. A sample BFSK modulation is shown in Figure 48.

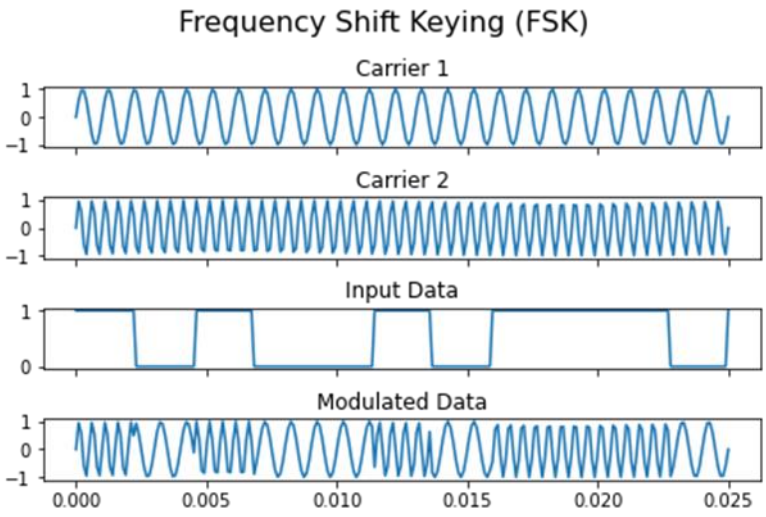


Figure 48 Frequency Shift Keying Modulation

B) Amplitude Shift Keying (ASK)

In amplitude-shift-keying, bits are differentiated by the changes in amplitude of the modulated signal, as shown in Figure 49. In ASK modulation, multiple amplitude levels can be used to differentiate various symbols. On-Off-Keying (OOK) is the simplest ASK modulation, which uses two levels of amplitude and transmits one-logic bits and zero-logic bits by presence or absence of a carrier signal, respectively. Figure 49 represents an OOK signal. The disadvantage of ASK modulation is that it is sensitive to distortions and atmospheric noises and the

advantage of this method is that the modulation and demodulation of ASK signals are relatively inexpensive.

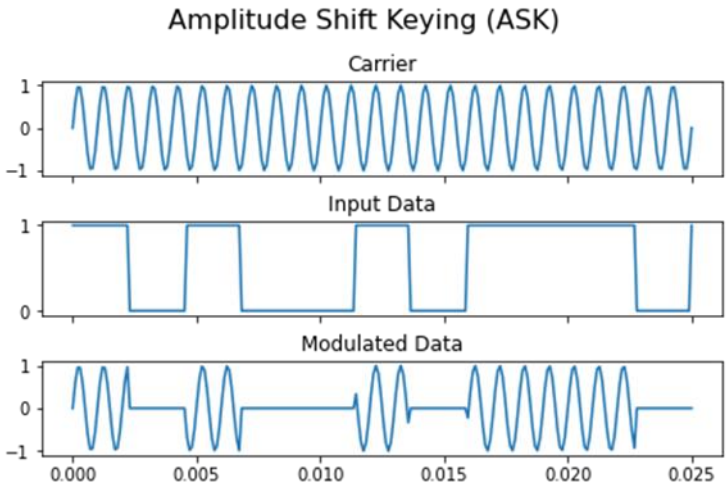


Figure 49 Amplitude Shift KeyingModulation

C) Phase Shift Keying (PSK)

In PSK modulation, each symbol is represented by a specific phase of the modulated signal. In the simplest form of PSK, Binary Phase Shift Keying (BPSK), two signals with different phases (i.e., Sine and Cosine) are used to represent binary data (0s and 1s).

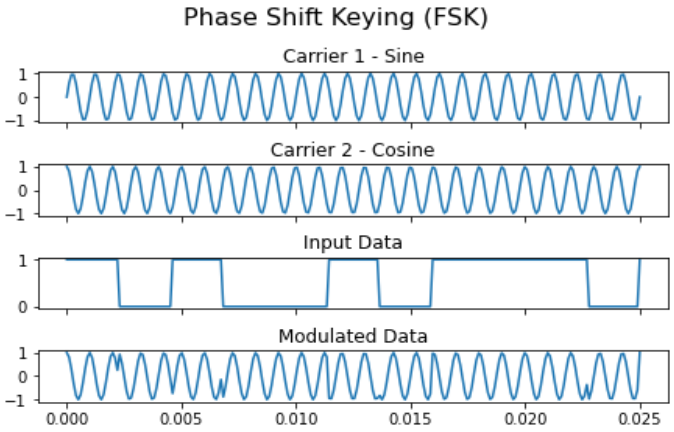


Figure 50 Phase Shift Keying Modulation

D) Comparison of FSK, ASK, PSK modulations for the underwater environment

In the simplest form of FSK modulation, BFSK, two distinct frequency bands are needed to transmit the information, and these two distinct frequency bands need to be apart from each other so that they can be demodulated successfully without interfering with each other. Thus, FSK requires a larger bandwidth compared to other modulation types where a single frequency band is enough for transferring binary data. FSK is widely used in underwater modem design and development as it is more immune to noises, especially in long-range communications, and also it is easy to demodulate compared to PSK. ASK modulation has a higher chance of error, as noise mostly affects amplitudes, but compared to FSK, using the binary form of ASK (OOK), less energy is consumed as the hydrophone is not active for logic-zero bits. The receiver circuit and demodulation process for ASK is inexpensive compared to other modulation schemes, and it also offers high bandwidth efficiency. PSK is the most efficient system regarding the speed of information transmission. However, It uses more bandwidth compared to ASK modulation, and the receiver implementation is expensive compared to others, as it requires coherent clock synchronization and demodulation. A good comparison of FSK, ASK, and PSK modulation strategies can be found in [111].

The IMPAQT transmitter node has been designed to be capable of transmitting Binary ASK (OOK), Multiple Frequency-Shift-Keying (MFSK), and Binary PSK (BPSK). The experimental characterization tests (described in Section 5.2) were carried out using OOK modulation since, according to the literature, OOK is a more suitable modulation option when receiver power consumption is a major concern. This is due to the fact that OOK doesn't require coherent demodulation and it is less dependent on gain control and resolution in the receiver. On the transmitter side, in the OOK scheme, the transmitter consumes relatively less power compared to other schemes, as it does not transmit any carrier wave for logic-zero bits. OOK can get

combined with FSK, enabling the use of multiple frequency (MFSK) advantages to send various symbols at a time [112].

4.2.7 Software-based transducer oscillation damping

One of the key limiting factors in the data transmission speed when using the OOK modulation scheme is the tendency of the transducer to continue free oscillation for a short while (or indefinitely in a frictionless environment) after being driven. There are various properties linked to the oscillation [113], and estimating the oscillation length requires information about the transducer fabrication stages and materials used, which is not easily possible. An alternative method is to measure the free-oscillation length in a medium by driving it for a certain amount of time and then measure the oscillation that results from that stimulation. The duration of induced oscillation and the free oscillation period were precisely measured, shown in Figure 51 below. As can be seen after 10 ms induced oscillation by the hydrophone driver circuit, the transducer continued to oscillate for 5.2 ms freely. The induced voltage was measured and found to have a direct relationship with the free oscillation period.

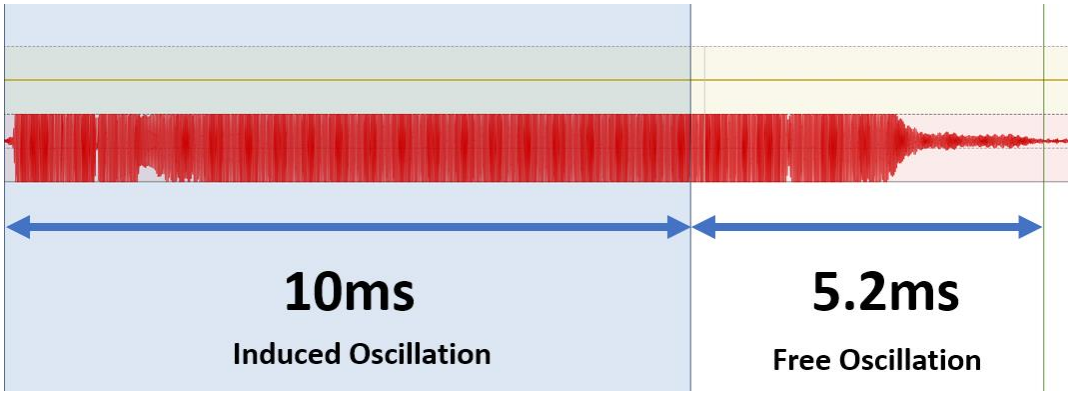


Figure 51 Oscillation measurement of the AS-1 transducer

It is important to measure the free oscillation period, as it can help to optimize the hydrophone induced oscillation duration, which ultimately increases the bitrate. In order to have a 10 ms total oscillation period, the induction duration was reduced to 4.8 ms to compensate for the free-oscillation that results from the driving signal. So overall, there would be 4.8 ms induced oscillation and 5.2 ms free oscillation,

which altogether results in approximately 10 ms oscillation that is required. However, this compensation should only happen if the logic-one is followed by a logic-zero. In other cases, the logic-one duration should be as normal (10 ms). This is necessary to keep the frequency or the period of the bits fixed and steady.

4.2.8 Communication interfaces

At the initial stage of the project, based on user requirements, a sealed tag with integrated sensors was planned with no physical connector for integration with external sensors so as to maintain enclosure integrity at depths up to 25 m. To provide a communication interface with the external sensors from the sealed and waterproofed transmitter unit (i.e. no external ports for sensor interconnect), an optical infrared interface was initially considered. A *TFBS4650 IrDA* transceiver was used to communicate with external sensors. The external sensor module/device also had to include an *IrDA* infrared transceiver on its board to communicate with the transmitter node. The *TFBS4650* application circuit is shown in Figure 52. *TFBS4650* is a tiny *IrDA* transceiver, and it can support data rates up to 115 kbit/s. It has a photodiode and the controller IC in the same package in a 1.6 mm(H) x 6.8 mm (L) x 2.8 mm (W) footprint [114].

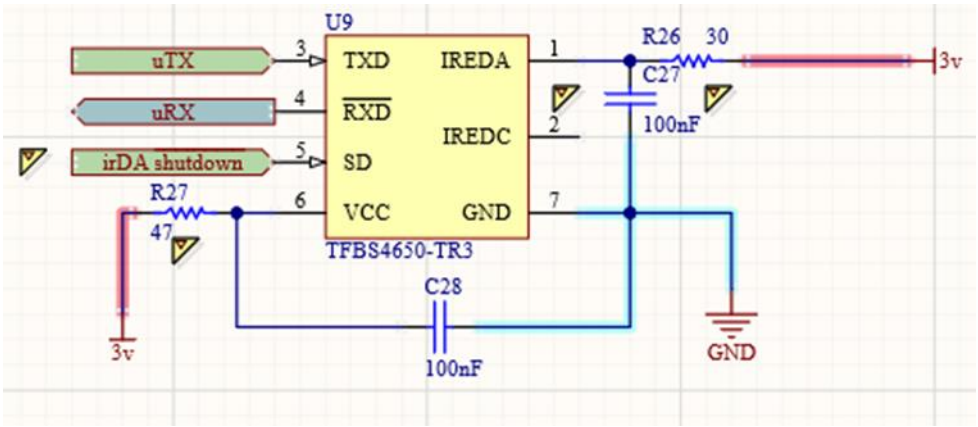


Figure 52 TFBS4650 - External IrDA interface

In subsequent designs, a wired interface to communicate with the external sensor was used, since commonly used marine sensors use a wired connection (analog or digital) and the requirement for integration via *IrDA* needs a redesign of

the off-the-shelf sensors or requires an intermediate board to communicate over *IrDA*, thus it increases the total cost of the monitoring solution while using a wired connection, simplifies the overall integration process, reduces the costs and efforts associated with system integration.

The wired interface connector is shown in Figure 53. This interface includes a selectable I^2C/UART communication interface plus an extra I/O for wake-up/handshaking purposes. The external sensors can trigger the IMPAQT transmitter node to wake up from sleep mode to read the external sensor's data using the wake-up pin fitted on the external connector. Also, there would be an option to schedule a plan for the node to wake up independently and read the external sensor data and transmit the collected data.

It also important to note that the external sensor needs to run on its own power supply (i.e. battery). This enables the transmitter node to monitor its usage and run independently from the external sensor.

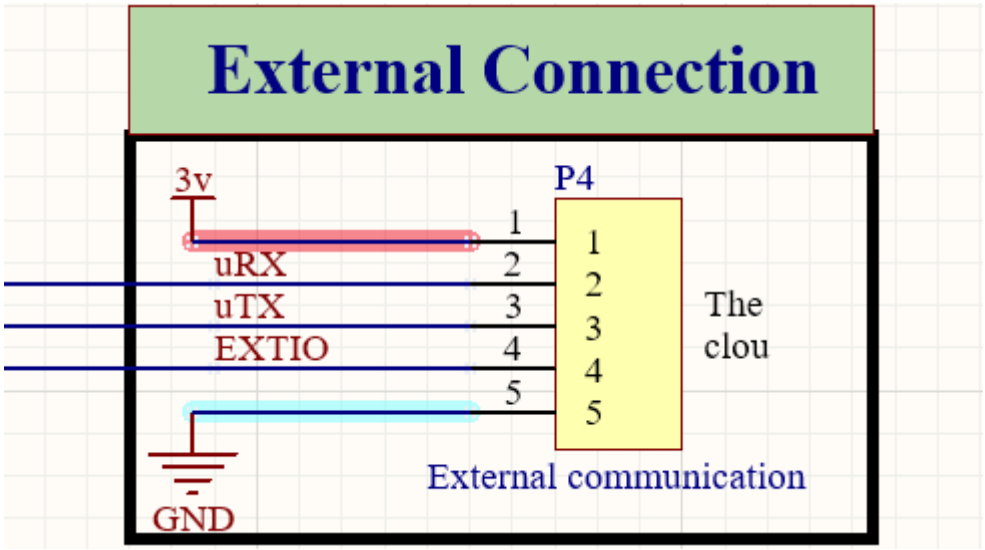


Figure 53 Wired interface

4.2.9 Acoustic transmitter board design

Altium Designer [115] was used to prepare the schematic, shown in Figure 95 in the Appendix section. The schematic is designed in hierarchical mode (Multi sheet design), where circuits are distributed in several blocks, and blocks are connected in a higher-level block. This technique facilitates the design and review process of the schematic. The designed schematic was translated into a PCB layout consisting of a four-layer printed circuit board (PCB), shown in Figure 54. A four-layer PCB stack-up was implemented so as to help to minimize the analog interference and noise on the board. Two middle planes in the board are used as the power planes (VCC, GND), and top and bottom layers are used as signal layers. The prototype development board final dimension is 33 mm x 55 mm.

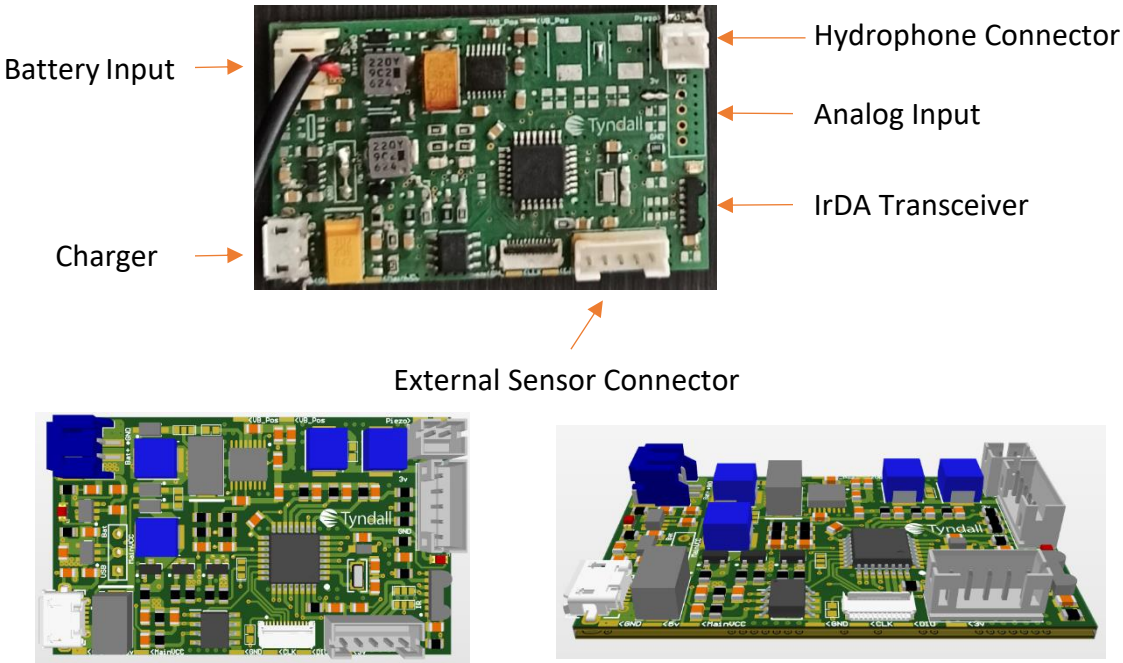


Figure 54 IMPAQT Acoustic transmitter node characterization board

4.2.10 Acoustic transmitter power consumption estimations

The transmitter node's power consumption is a critical factor in the IMPAQT project, and it impacts the maintenance schedule of the marine aquaculture sites directly. In Table 6, the power consumption of the components on the board is shown, and the estimation values are obtained from each individual component datasheet provided by the manufacturers.

To measure the practical power consumption of the transmitter board, a DC power analyser from *Agilent Technologies* with the part number *N6705B* [130] has been used. The *N6705B* power analyser has three measurement ranges of 3 A, 100 mA, 1 mA and 10 uA. In the test scenario, the measurement range was automatically selected by the power analyzer. The highest sampling rate for the power analyser is 0.02048 ms (48.82 kHz). While this sampling rate is adequate for measuring the system behaviour and power consumption at any single point, it cannot be used when the boost converter circuit is active since the boost converter circuit is performing high-current switching at 300 kHz and cannot be sampled at the sampling frequency of the power analyser (48.82 kHz) due to aliasing [116]. Hence, the current consumption of the transmitter tag is measured with the power analyser using a booster circuit in standby mode. When the booster circuit is in standby mode, the input voltage of the circuit (3.7 V) minus the booster diode forward voltage (0.3 V) will be applied to the hydrophone. In this scenario, an average voltage of 3.4 V is applied to the hydrophone instead of 20 V, which results in less power consumption by the hydrophone (refer to Equation 12). To compensate for this difference in current consumption, the average current of the hydrophone at 20 V can be estimated theoretically and accounted for in the measurements by using Equation 12 as discussed in 4.2.1. In all the power measurements, there was a 10 m cable connected to the hydrophone, which will add an extra capacitance of 1.18 nF (according to the manufacturer [90]). This capacitance will also draw extra current when an AC voltage is applied to it, and this should be added to the total capacitance of the transducer. Using Equation 12, at the frequency of 42 kHz, the average current

consumption of *AS-1* transducer considering 10 m cable is 1.7 mA at driving voltage of 3.4 V and 10.3 mA at driving voltage of 20 V. Since the 10.3 mA current consumption is from the transducer point of view and rated at 20 V, this needs to be converted to the equivalent current drawn from the battery using the Electrical Power (P) equations shown Equation 11. The Power drawn from the battery can be estimated using following equations

$$P_{Battery} = P_{Transducer} + P_{Booster\ loss,} \quad 14$$

$$P_{Booster\ loss} = \frac{(10 \times P_{Transducer})}{100} \quad 15$$

where $P_{Battery}$ is the power drawn from the battery, $P_{Transducer}$ is the power drawn by the transducer and $P_{Booster\ loss}$ is the booster loss, which is typically 10% in the MAX1771 booster circuit as claimed by the manufacturer [100].

In order to estimate the power drawn from the battery, the measured values are substituted in the 11, 14, and 15 :

$$P_{Transducer} = 0.0103 \times 20 = 0.206$$

$$P_{Booster\ loss} = 0.0206$$

$$P_{Battery} = 0.206 + 0.0206 = 0.2266$$

to estimate current drawn from the battery, Equation 11**Error! Reference s ource not found.** is used, hence:

$$P_{Battery} = I \times V$$

$$0.2266 = I \times 3.7$$

$$I = \frac{0.2266}{3.7} = 0.0612$$

According to the calculation above, there would be a 61.2 mA current drawn from the battery when the booster circuit is active, and the transducer is being driven

at 20 V. This will lead to a 59.5 mA difference when the booster is active compared to when it is in standby mode and should be accounted for in the measurements. The resulted estimation and measurements are shown in Table 6.

Table 6 Power consumption estimations from battery point of view

Component	**Sleep current (µA)**	**Max supply current (µA) when transmitting logic-one**	**Max Supply Current (uA)-when transmitting logic-zero**
MCP73831 [117]	0.1	2	2
MAX1771 [100]	5	110	110
TPS78230 [110]	0.4	1.3	1.3
ADG1436 [106]	1	280	280
STM32L082x [118]	0.41	1150	1093
AS-1 [90] + 10 m Cable	0	61200	0
Voltage Divider *	1.5	8.2	8.2
Estimated Total	**8.41**	**62751**	**1494**
Measured Total	**10.5**	**65650 ****	**1606**
***** Voltage divider is a passive circuit to measure boosted voltage discussed in Section 4.2.2 ** This value is the measured value with the booster in standby (6.1 mA) plus the compensation for the booster circuit (59.5) as described above			

According to Table 6, There is a 2.09 µA difference between estimated and practical measurements in the average sleep current, which is negligible, and that can be measurements error or capacitors leakage [119]. Such a lower power transmitter node has not been previously reported in the literature. There is a 197 µA difference in max supply current when transmitting logic-zero. The possible explanation is the capacitor charging after driving the transducer, or it can be measurement errors since this measurement is done with the 100 mA range of the power analyzer. There is a 2899 µA difference in the measurements when the transducer was active and transmitting logic-one. This is the result of power dissipation on the analog switch (ADG1436) internal resistance (1 Ω) [106] when actively driving the transducer, and also it can be the result of aliasing when measuring the average current of the transducer when it was oscillating at 42 kHz.

The power consumption profile and the average current consumption are shown in Figure 55. This current profile represents the scenario where the booster circuit was in standby mode, and the system was running from a 3.7 V source. It is important to note that in this chart, the I_B value is not accurate since the transducer was drawing current at 42 kHz and the power analyzer sampling frequency was 48.82 kHz, and according to Nyquist theorem [116], this value may not be accurate. However, the overall power consumption plot is a good approximation of the current consumption profile.

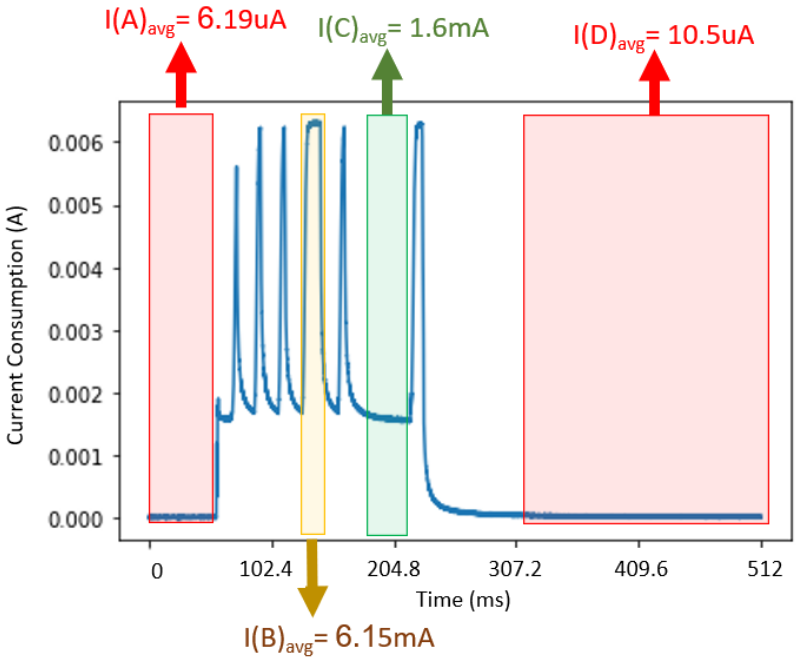


Figure 55 Power consumption plot and the corresponding measurements with the booster in the standby mode

4.3 IMPAQT Acoustic Receiver Prototype

One of the main challenges associated with acoustic communications in water is that the received signal is generally a mixture of various sound signals from the waves, animals and water hitting surface objects, and even sounds from out of the water propagating underwater. There are also various noise sources on the board, e.g., power supply noise that needs to be removed. Hence, it is necessary to filter out the irrelevant signals and demodulate the clean signal in order to retrieve the data bits from it. To extract data bits from the received signal, a combination of theoretical modelling, analysis, and simulations are required. After several designs and simulation iterations, the block diagram shown in Figure 56 was identified as the optimum solution. It features filtering of three frequency bands, which provides the possibility to characterize various hydrophones and piezo materials. The provided solution also features a hardware demodulator for OOK and BPSK modulation which off-loads the host processor since all the demodulations happen in the hardware. Receiver also includes a direct analog to digital sampling circuit, which enables the possibility of software demodulation if required.

As discussed earlier in 4.2.1, the *BII-7003* hydrophone was selected as the receiver hydrophone. The input signal is fed into a JFET pre-amplifier, and then it is fed into the hydrophone driver to remove the offset and drift and amplify. The amplified signal then flows into a filtering stage to remove any irrelevant noise and unrelated frequency ranges and amplify the clean signal further. As the received signal is expected to be extremely weak and of unknown value, it feeds into a digitally controlled variable gain amplifier to amplify to the required level. There is the onboard microcontroller that can sample the filtered analog voltage directly using a 16bit analog to digital converter fitted on the board. The unprocessed analog signal can be used as a dataset for future research on software-defined demodulations techniques. Software-defined demodulation can reduce the receiver board costs significantly by reducing the BOM cost associated with hardware demodulation. The analog signal also converts to a 1bit digital signal for the demodulation stage.

Converting the analog signal to a digital signal simplifies the circuit design for subsequent demodulation circuits. There are BPSK and OOK demodulators on board which can be used to demodulate the data directly to data bits. In the rest of this section, each block shown in Figure 56 will be discussed.

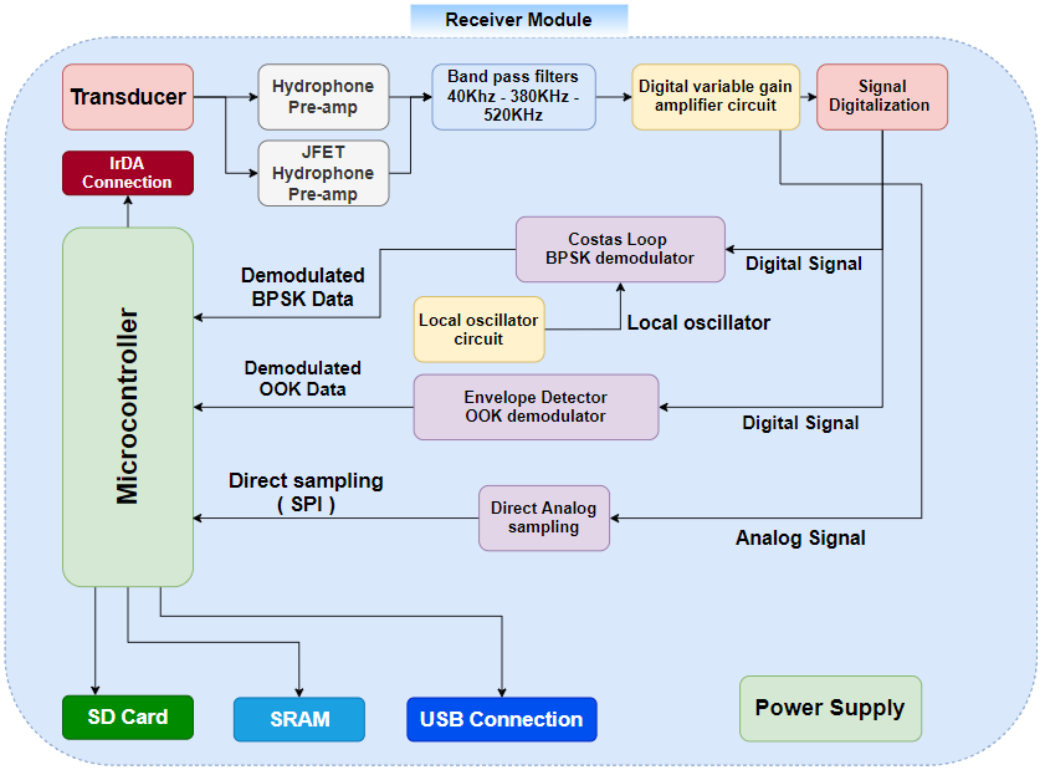


Figure 56 IMPAQT Receiver prototype board

4.3.1 Power supply design

The IMPAQT receiver board requires a number of specific voltage levels in the filtration and amplification stages to perform signal filtering, amplification, and conversion. The required voltages are +5 V, -5 V, 3.3 V, 2.5 V, and 0 V. The power input in this circuit is the USB or Battery connector. The power input provides a +5 V level. *MIC5239* regulates the +5 V to +3.3 V to supply the microcontroller and various

digital controllers. *MIC5239* is a low quiescent regulator which can provide up to 500 mA, and it has an input range of 2.3 V to 30 V [120].

To provide -5 V, a DC voltage inverter is required. This can be done using a step-down voltage regulator or using a charge-pump circuit. Step-down converters are generally used when a high-current power supply is needed. Step-down converters regulate the voltage at any desired voltage below the input voltage, using a switch, an inductor, and a controller, same as step-up converters. On the other hand, charge-pump inverters can be used where voltage regulation is not required, and only the inversion of the input voltage is required. It was decided to use a charge-pump circuit as the board already have the +5 V voltage, and only a -5 V is required. The charge pump requires a simpler circuit, and it has a very compact footprint making it more suitable for miniaturized systems. For this purpose, *MAX660* [121] from *Maxim* has been picked out. *MAX660* is a charge-pump voltage inverter that converts any voltage in a range of +1.5 V to +5.5 V input to a corresponding negative output. It only requires two low-cost capacitors, and it can provide up to 100 mA output. The working principle of the charge pump inverter is shown in Figure 57. At $T_{0,}$ S1 and S3 switch turn on, and S2 and S4 turn off, and this will charge the C1 capacitor, at T_1, C1 capacitor is charged, and it can act as a temporary power supply, so S1 and S3 turn off, S2 and S4 turn on, note that C1 polarity will change at this moment, the pin that was connected to V+, now will connect to GND and the pin that previously was connected to GND, at this moment will act as the V_{out} which results in the V- or the inverted voltage [122].

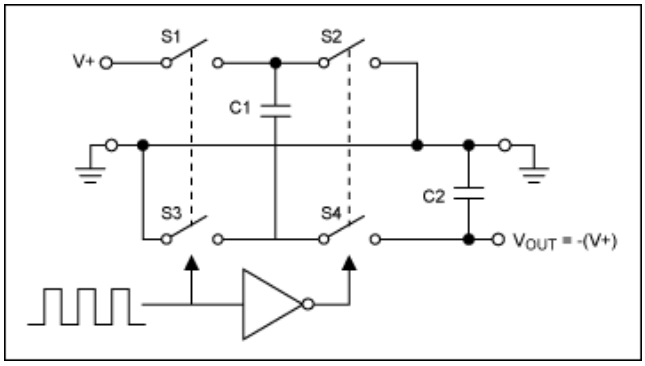


Figure 57 Charge pump inverter (adapted from [122])

In the signal digitization stage, a 2.5 V is also required for comparing purposes and biasing the amplifier. The current consumption of the 2.5 V signal is minimal; hence it was decided to use an opamp circuit for providing the 2.5 V reference voltage. As it is shown in Figure 58. The 2.5 V circuit includes a voltage divider that divides 5 V in half, resulting in 2.5 V, the 2.5 V feed into a voltage follower opamp circuit that acts as a current buffer and supplies the subsequent circuits at 2.5 V.

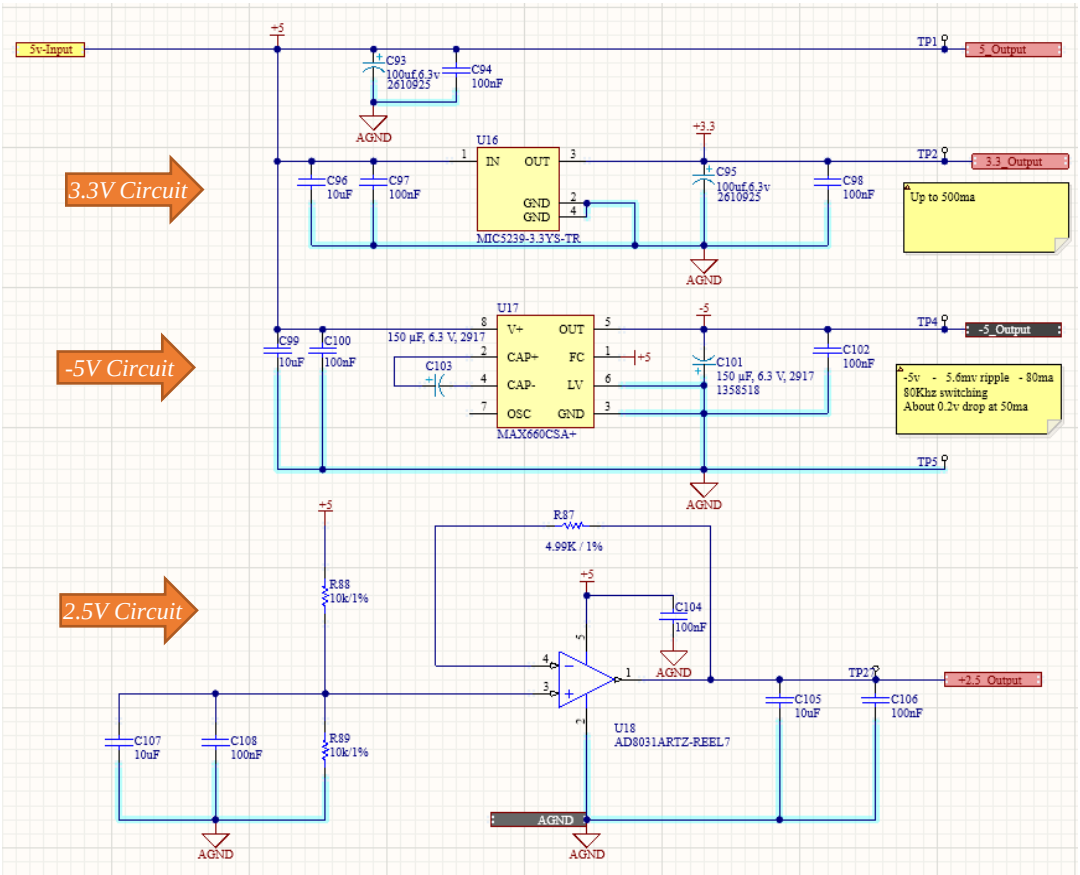


Figure 58 Power supply

4.3.2 Hydrophone amplifiers

As discussed in Section 4, hydrophones are similar to microphones but able to work underwater and record sound from all directions or a specific direction. Hydrophones are generally built from piezo materials that produce a small electrical current subject to changes in water pressure. Since their induced current is very small, a hydrophone amplifier circuit is necessary to amplify the voltage created by the current. In the transmitter node prototype design, two different circuits have been used to perform hydrophone driving for comparison and selection of an optimum design. One of the circuits uses a commercially available hydrophone driver IC, *LT1792* [123], and another circuit uses a J-FET transistor circuit to perform the hydrophone driving [124]. *LT1792* is JFET low noise op-amp that can amplify low-level signals from high impedance capacitive transducers. *LT1792* is usually combined with another precision amplifier to implement a so-called "DC Servo circuit". A DC-Servo circuit is an automatic control system to eliminate the DC offset in the output of the amplifier [125]. In Figure 59 (adapted from [123]), *LT1792* acts as the amplifier, and *LT1097* acts as a DC Servo amplifier. Figure 59 is simulated in LTSpice software, and output is shown in Figure 60.

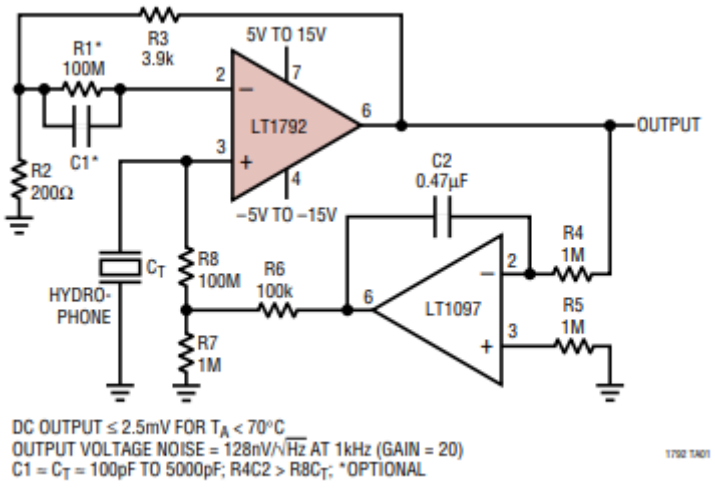


Figure 59 Hydrophone amplifier with DC Servo (adapted from [123])

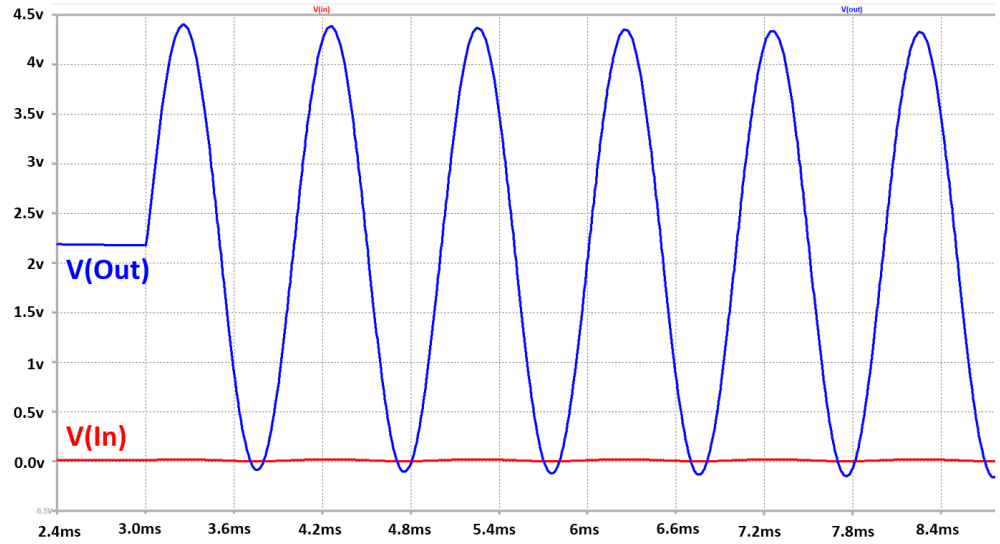


Figure 60 Hydrophone driver simulation in LTSpice

The gain for the *LT1792* circuit is set at 77, and it is limited by the maximum gain-bandwidth property of the *LT1792*, which is 5.6 MHz. Considering 70 kHz as the maximum bandwidth that might be required to characterise the *AS-1* hydrophone, the maximum gain of the *LT1792* amplifier at this frequency will be limited to 80. Figure 96 in the appendix section represents the implementation of the *LT1792* circuit with DC Servo.

Renner et al. [37] used a JFET hydrophone driver in their *AHOI* underwater modem. This simple circuit will amplify the hydrophone signals, which then flow into a subsequent circuit for extra amplification. This circuit is also implemented in the IMPAQT board with a gain of 25, and it is shown in Figure 61. In the IMPAQT prototype board, initially, these circuits were used in parallel to characterize their performance, however, after evaluation and characterization, the two-circuit used in a series, with the JFET pre-amplifier as the first stage and LT1792 circuit as the second stage. The JFET amplifier pre-amplified the signal with a gain of 25, and the *LT1792* circuit amplified the circuit further with a gain of 77.

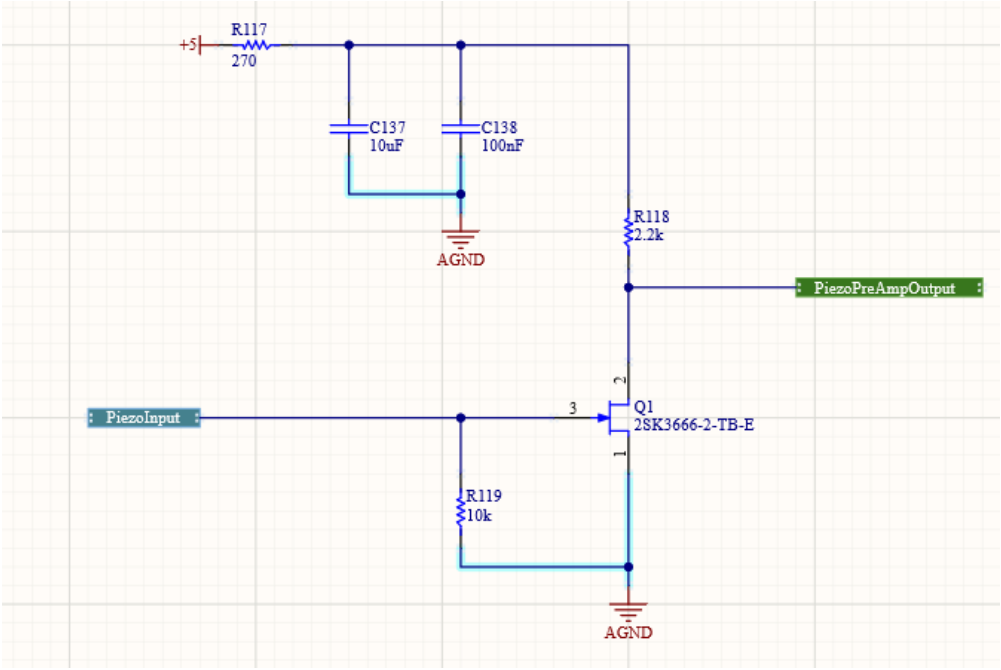


Figure 61 J-Fet based hydrophone driver circuit

4.3.3 Filtering and amplification of the received acoustic signal

Signal filtering is a crucial part of the receiver board. A hydrophone receives signals in a wide range band. The selected *BII-7003* hydrophone can receive all signals in the range of 1 Hz to 560 kHz, where it contains sounds from low-frequency seismic background noises to audible signals from marine animals and terrestrial sound sources and ultrasonic signals from bubbles and surface waves [126]. The IMPAQT telemetry platform uses 42 kHz as the transmission carrier signal. Hence the rest of the frequencies are unwanted signals that should be filtered out and removed. In order to do so, filter circuits were integrated into the receiver platform circuitry. There are various filtering circuits that could be used for this purpose, and the *Analog filter wizard tool* [127] was used to generate the optimum filtering circuit according to requirements and simulate its performance prior to manufacturing. The Analog device filter wizard tool is a free tool provided by Analog Devices Inc to design active hardware-based filters according to defined requirements and the selected frequencies to be filtered out of any signal. This tool provides a recommended circuit using Analog Devices operational amplifiers. As a system characterization circuit was

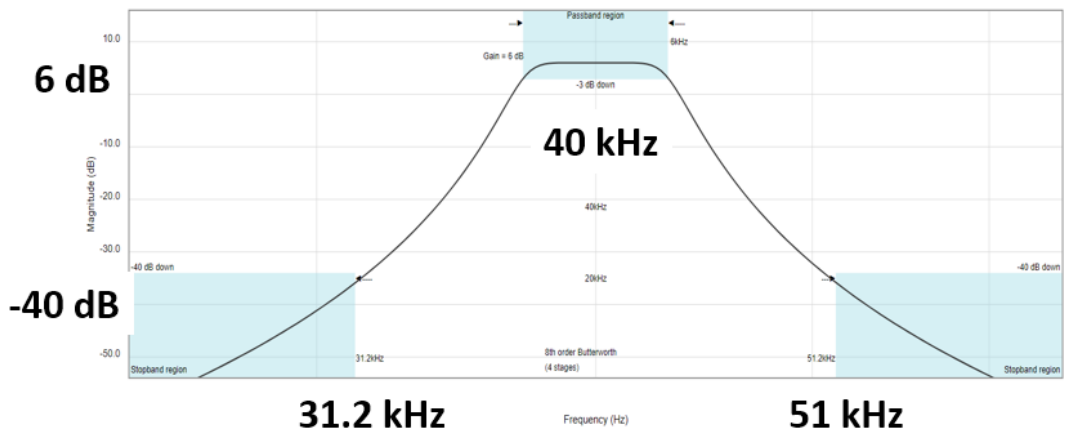
being developed, various filtering circuits were considered to potentially being able to evaluate several receivers and transmitter transducers to establish the best one for implementation in the IMPAQT project. Table 7 lists the implemented filters in the characterization board for evaluation.

Table 7 Implemented filters in the prototype board

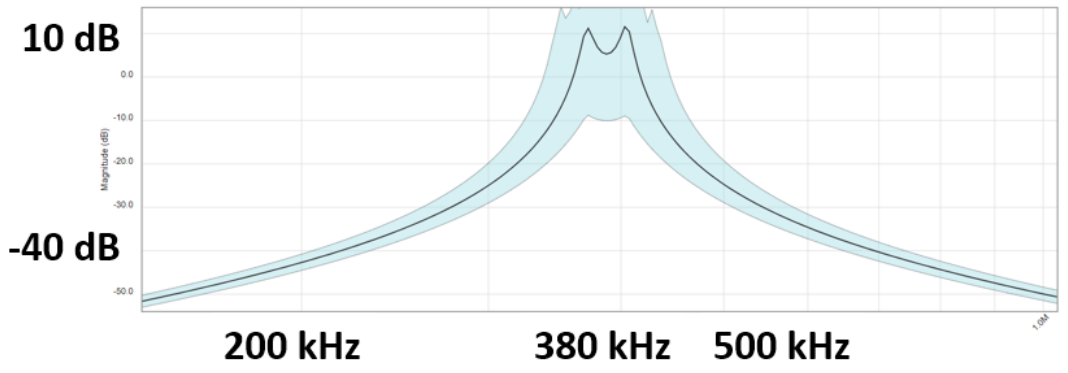
Centre frequency (kHz)	**Bandwidth** (kHz)	**Order**	**Type**	**Gain** (dB)
40	6	8	Butterworth	6
380	50	4	Chebyshev	3
380	60	8	Butterworth	10
520	90	8	Butterworth	10

The 40 kHz filter will be used to evaluate the selected hydrophones (*BII-7003* and *AS-1*), while there are also filters for evaluating miniaturized piezo materials (380 kHz and 520 kHz). As it can be seen in Table 7, there are two 380 kHz filters with almost the same specification considered, however one is 4^{th} order, and the other one is 8^{th} order. The 4^{th} order uses fewer components resulting in a smaller footprint (and cost) on the circuit, making it preferable to the 8^{th} order filter subject to equivalent performance. In future, it will be beneficial to compare the performance of the 8^{th} and 4^{th} order 380 kHz filters. In case that the 4^{th} order filter demonstrates a similar noise rejection and amplification performance as the 8^{th} order filter, it can replace the 8^{th} order filter in future designs, which will reduce the receiver filter stage power consumption and size. In Table 8, a frequency analysis of the filters has been shown. The filter frequency analysis shows that the filter amplifies the passband frequency region of interest and attenuates the remainder from the signal.

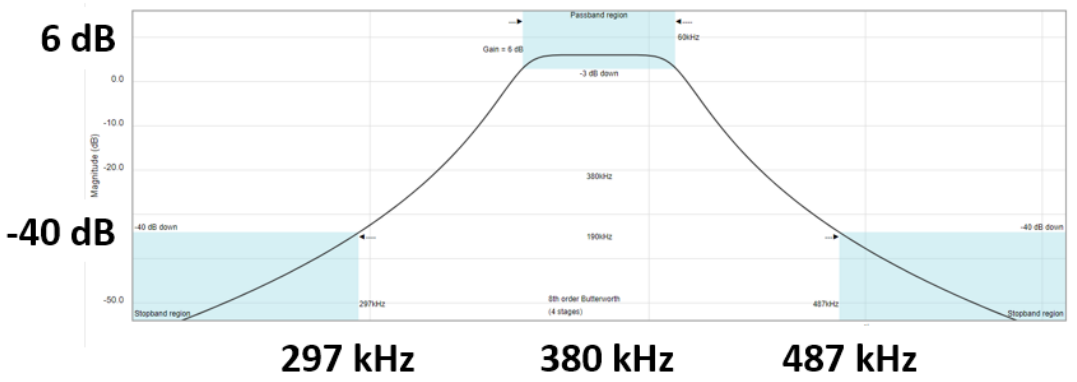
Table 8 Frequency analysis of the filters [127]



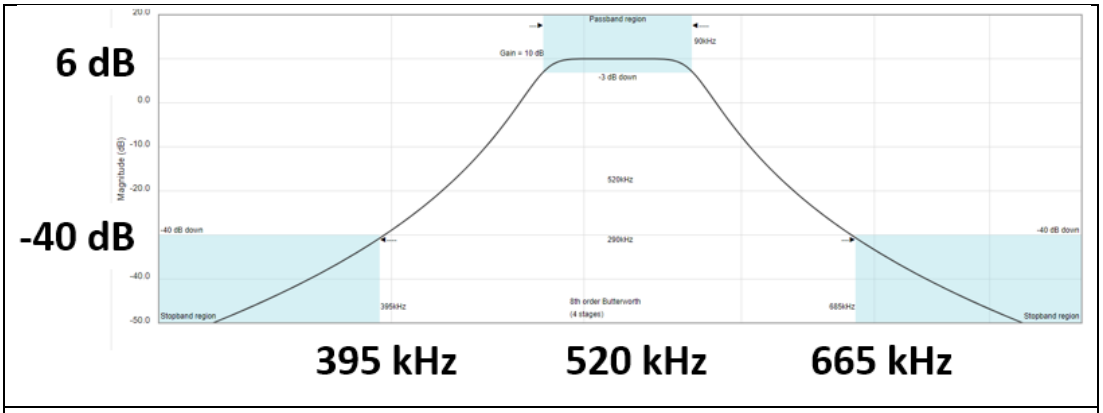
40 kHz 8th Order Butterworth filter – 6 kHz pass band – 6 dB gain



380 kHz 4th order Chebyshev filter – 50 kHz pass band – 6 dB gain



380 kHz 8th order Butterworth filter – 60 kHz Pass band – 6 dB gain



520 kHz 8th Order Butterworth filter – 90 kHz Pass band – 6 dB gain

The filter design tool also generates the recommended circuit to achieve the filter requirements. In Figure 62, the recommended circuit for the 4th order 380 kHz filter is shown.

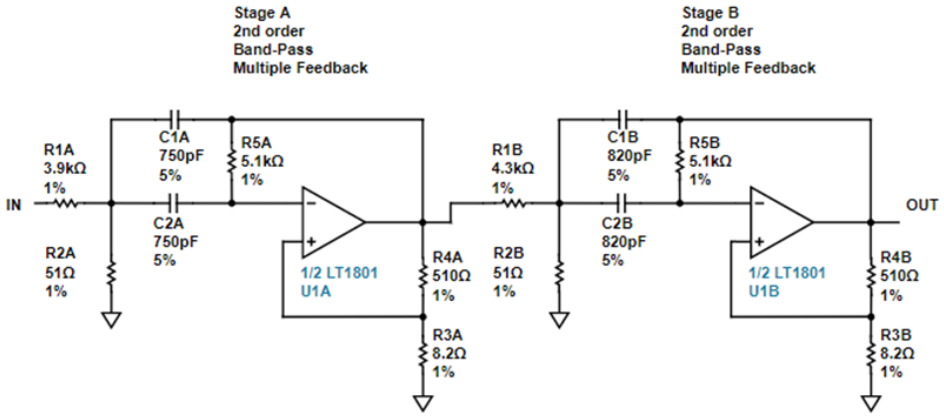


Figure 62 Recommended circuit for 4th order 380 kHz filter (adapted from [127])

The filter wizard also generates an *LTSpice* model to simulate the generated filter circuit. For instance, for the circuit shown in Figure 62, an *LTSpice* model was generated, and the result of the frequency analysis of the circuit is shown in Figure 63. The blue line represents the output from the first amplifier output, and the red line indicates the output of the last stage.

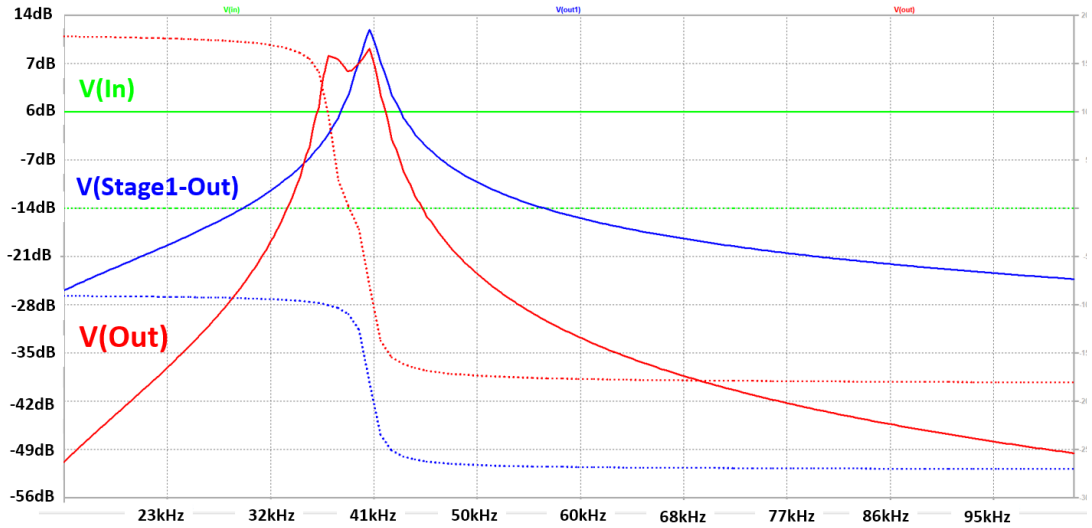


Figure 63 Frequency analysis of the 4th order 380 kHz filter

Overall, four filter circuits were studied and implemented in the receiver design. To reduce their effect on the input stage of the signal, they are separated from the input stage and output stage using solderable jumpers (SJ6-SJ13). This provides the opportunity to test each of them individually without the effect of another filter. The output signal of the filtering stage was measured, and it was a variable signal between –2.5 V to +2.5 V, where the transmitter and receivers were in the 1 cm distance of each other underwater.

4.3.4 Digitally controlled signal amplification

Underwater transducer nodes distance from the receiver node may vary, as such, they might be close to the receiver node, or they might be at 100 m distance from the receiver node. Therefore, the received signal level (ultrasonic wave amplitude in the transmission medium) may vary, and it is required to control the received signal level accordingly. B.-C. Renner et al. [124] proposed the idea of using an I^2C variable resistor in conjunction with an amplifier to control the amplification gain of the signal. In Figure 97, included in the appendix section, the circuit diagram of the digitally controlled variable-gain amplifier, which was implemented in the IMPAQT system described in this thesis, is shown. As discussed in 4.3.3, the output of the filtering stage is a variable signal between -2.5 V to +2.5 V. In this circuit, the

signal passes through a DC offset adjusting circuit (C131 and R112). This offset circuitry adds a +2.5 V offset to the signal, which shifts the signal from -2.5 V - 2.5 V range to 0-5 V range. Removing the negative range of the signal will result in simpler subsequent circuits as the signal shifts to the common logic range. The shifted signal feeds into the non-inverting pin of an *OPA365* amplifier [128] as part of the non-inverting amplifier circuit. A feedback resistor network is present on the inverting pin of the amplifier, which controls the gain of the amplifier. In the feedback resistor network, a digital potentiometer, *AD5245* [129], is present, which can be configured via an I^2C bus. By changing the resistance level of the *AD5245* via I^2C, it is possible to control the feedback resistor network to achieve a variable gain amplifier. The onboard microcontroller monitors the average voltage level of the filtered signal, and using a control loop, it stabilizes the signal level by changing the resistance of the digital potentiometer.

4.3.5 Received signal digitization

The demodulation of an analog signal is a challenging task as it varies, and it can be impacted significantly by noise. As such, to facilitate the demodulation stages, the signal was digitized at an early stage in the demodulation process. This simplifies the further demodulation steps and provides more stability and robustness to the circuit as digital signals are less sensitive to noise than analog signals, and this approach also reduces the component count associated with analog demodulation of signals. The digitization circuit, which is shown in Figure 64, is a Schmitt trigger circuit. A Schmitt trigger is a comparator circuit that only changes the output signal when the input signal crosses predefined values, which is known as hysteresis value. The Schmitt trigger will prevent the input noise effect on the output. In the circuit shown below, the comparing value is +2.5 V, with a 1 V hysteresis value. The output signal would retain its value in the input range of +1.5 V to +3.5 V, resulting in the elimination of unwanted oscillation in the output. The selected hysteresis range is selected based on the observation of the signal level using an oscilloscope. The

comparison of a Schmitt trigger versus a single threshold comparator is shown in Figure 65.

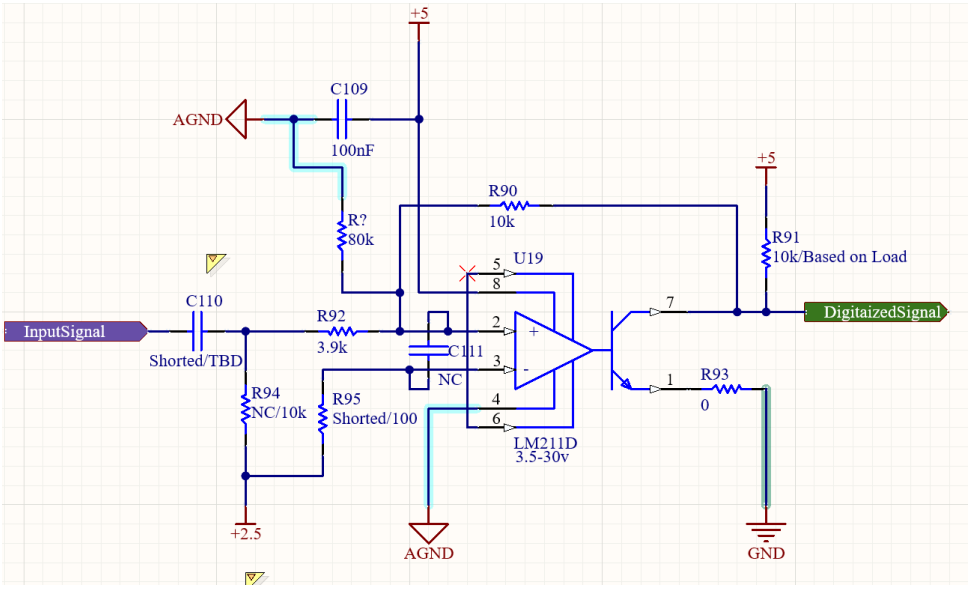


Figure 64 Schmitt trigger circuit

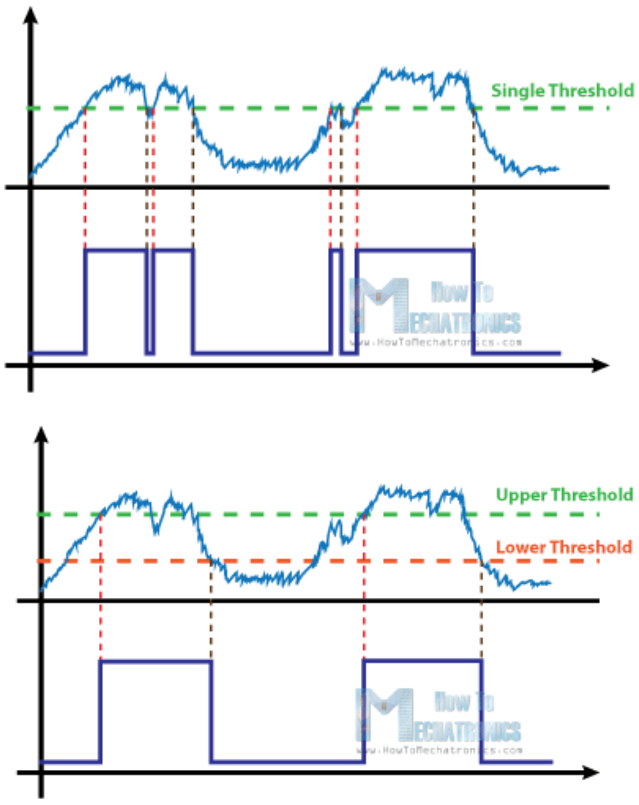


Figure 65 Single Threshold comparator (Top) vs Schmitt trigger comparator (Bottom) (adapted form[130])

4.3.6 BPSK demodulation circuits design

One of the primary challenges of the receiver prototype board is the BPSK demodulator circuit. It is the most complex circuit block on the board. Asgarian et al. [131] reviewed various techniques for the demodulation of BPSK signals. In summary, there are coherent and non-coherent demodulation approaches. The main difficulty with the coherent technique is the estimation of the carrier frequency and phase, which is required for the phase-shifting estimation. The receiver board should detect the frequency and estimate the phase of the received signal and estimate the variation in the phase throughout the reception of the data stream. In non-coherent demodulation, a clock recovery circuit is unnecessary, and the demodulation depends on the phase-shift moments. Hosseinnejad et al. [132] proposed the idea of demodulation of the BPSK signals using a CMOS clipper and several ICs to reconstruct the received data bits. The idea and circuit are shown in Figure 66. The idea is that the CMOS clipper circuit detects negative and positive tops, shown as *Pulse+* and *Pulse-*. These two peaks are combined together with an OR gate and go through a digital frequency divider circuit to construct the clock for the D flip-flop. The D flip-flop sample the digital BPSK signal at the clock rising edge. Using this method, one can reconstruct the data stream.

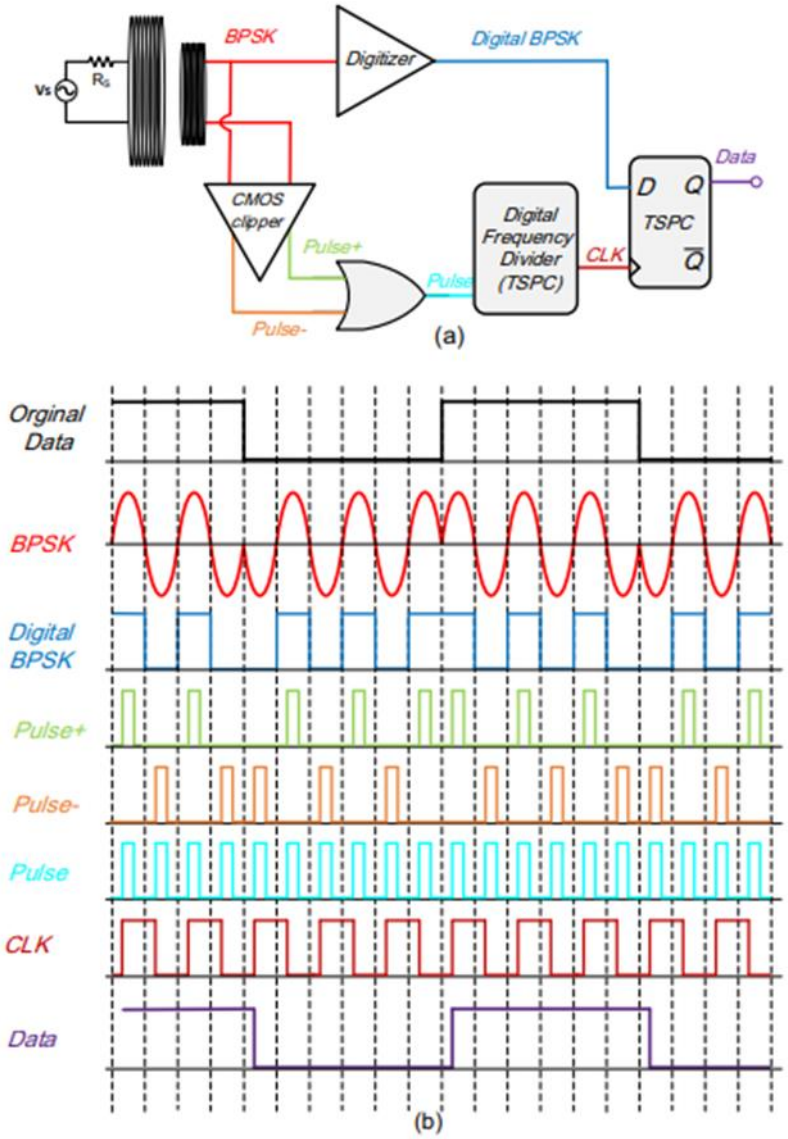


Figure 66 VCO-free digital BPSK demodulation (a) Proposed circuit,(b) the waveforms (adapted from [132])

This technique was originally developed to be used in the demodulation of signals from implantable RF receivers. As such, this technique requires an immediate change of the phase in the transmitter's transducer signal, which is achievable when using RF systems but is more challenging to have in the transducers for the underwater environment. Underwater transducers have the tendency to hold to their current states and resist changes, thus they won't respond immediately to the phase and frequency changes. To verify the proposed method's potential for the

underwater wireless system, it was simulated to establish its capabilities. The simplified block diagram of its operation is shown in Figure 67. A similar circuit was implemented in *MultiSim* simulation software from *National Instruments* [133], the simulation results were promising, and as can be seen in Figure 68, the input signal was digitized, and the clock signal recovered from the digitized signal by the signal clipper circuit. The recovered clock used as the clock input for the D flip-flop to retrieve the data from the modulated signal.

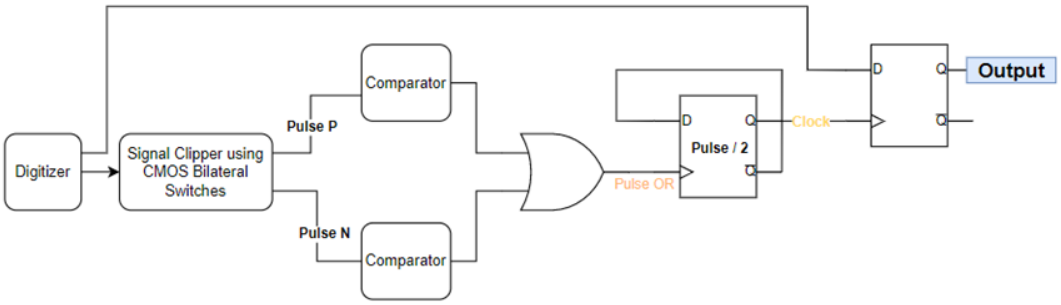


Figure 67 Simplified working principal of VCO-Free BPSK Demodulator

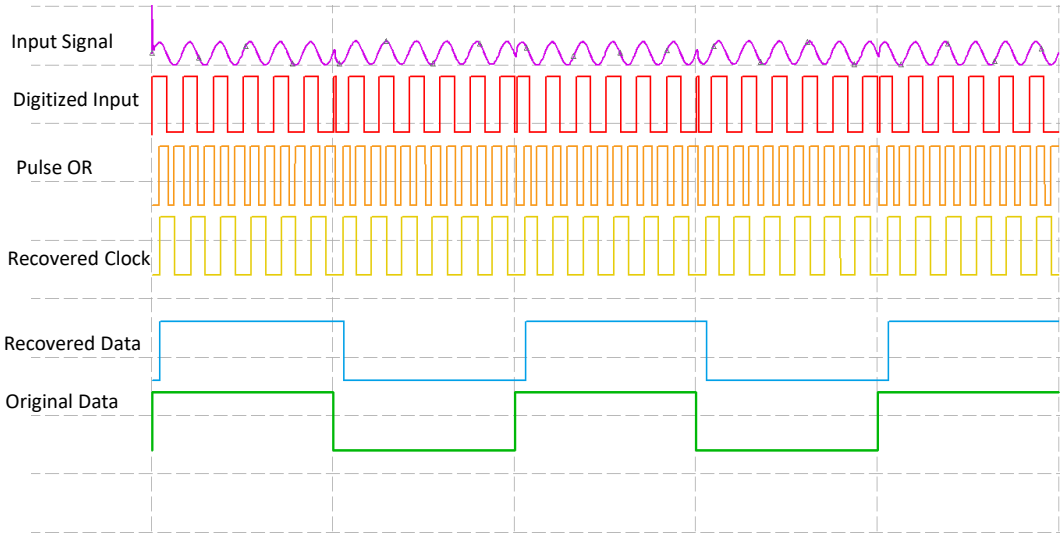


Figure 68 VCO-Free BPSK demodulation simulation

However, during the simulation analysis, it was noticed that this technique is extremely sensitive to the phase of the phase-shifting moment. A sample of incorrect demodulation is shown in Figure 69; the dashed red rectangle indicates an incorrect data recovery due to this phase shift sensitivity. At point (A) in the figure, shifting at a specific phase causes a quick toggle in the digitized input; however, in (B), a phase shift happened with a specific phase which did not result in a toggle in the digitized input, this results in an incorrect clock recovery, and as such, it caused wrong data recovery. It may be possible to control the exact phase in RF communications, while in underwater communication phase can change due to artifacts caused by the underwater environment.

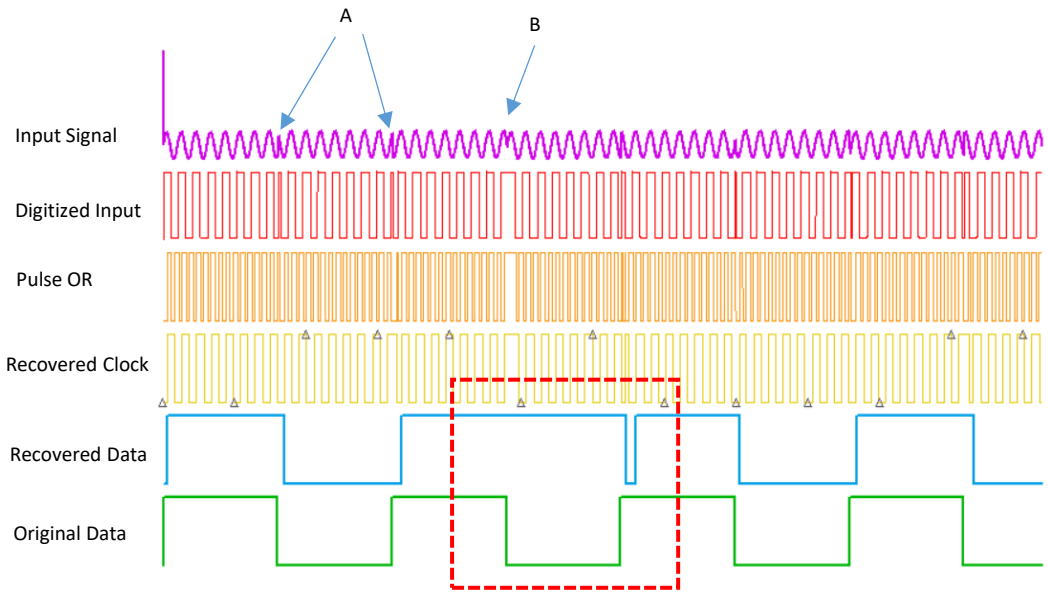


Figure 69 A sample of the wrong demodulation

Considering the difficulties with various non-coherent demodulation, the coherent demodulation approach was considered. A typical coherent demodulation circuit is the Costas loop, shown in Figure 70.

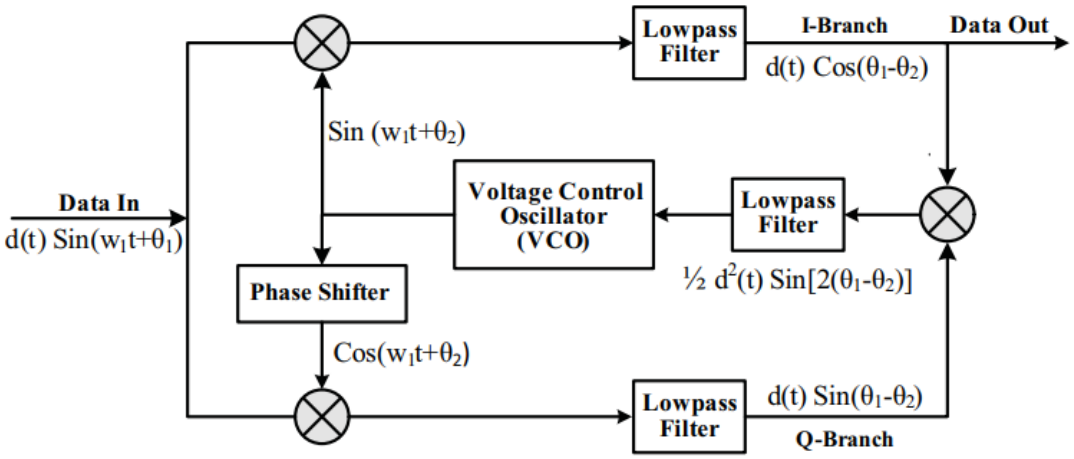


Figure 70 Costas loop (adapted from [131])

One of the main elements in the Costas loop block diagram, presented in Figure 70, is the Voltage Control Oscillator (VCO) that produce a carrier clock, which gets multiplied by the input signal and result in data recovery. A detailed explanation and working principle of the Costas loop is discussed in [134], [135]. Based on the research available in the literature, a Costas loop in the *MultiSim* environment was implemented and simulated. The simplified block diagram and simulation graph for the implemented Costas Loop is shown in Figure 71. The input signal is fed into a mixer circuit which multiplies the input signal by the local clock (Sine vector) and inverted of the local clock (Cosine vector), which are produced by the VCO circuit. This results in the decomposition of the input signal into the corresponding sine vector and cosine vector of the signal. By comparing the sine and cosine outputs, the data bits would be recovered. As it is shown in Figure 71, when the red signal exceeds the grey signal, it indicates a logic-zero; otherwise, it indicates a logic-one.

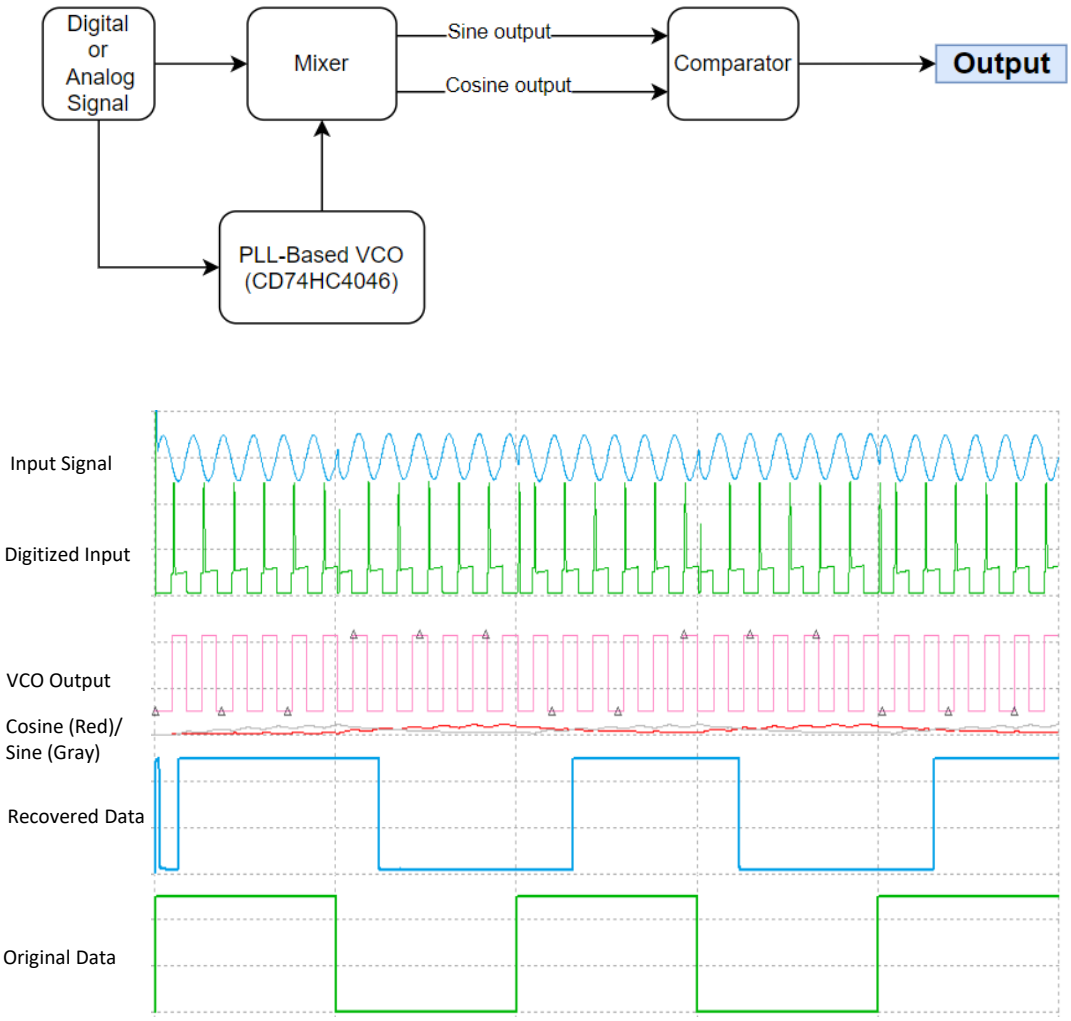


Figure 71 Costas loop block diagram and simulation

For the mixer part, an analog switch has been used. Considering the analog switch circuit in Figure 72, when the VCO output is logic zero, the input signal will redirect to CosOut, and when the VCO output is logic one, the input signal will redirect to SineOut. Hence the input signal will separate into in-phase and out-of-phase signals. When the input signal is in-phase with the clock (VCO output), the signal goes through SineOut; when the input signal is out-of-phase, the signal goes through the CosOut. For successful demodulation of bit-stream, it has been supposed that the VCO output phase does not change in the process of packet reception, and it remains locked with the first-bit phase.

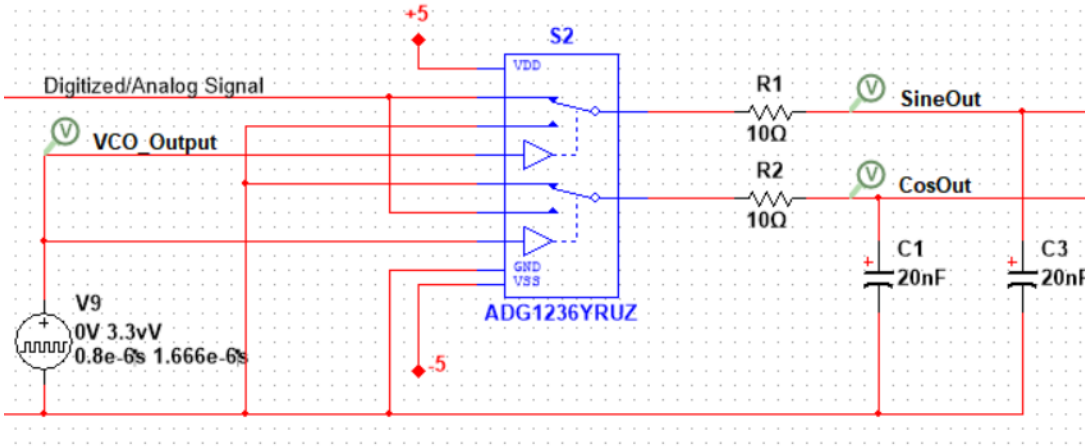


Figure 72 Analog switch-based mixer

The SineOut and CosOut signals flow through a comparator, which compares them and produces the output, which is the recovered data bits. The comparator is shown in Figure 73.

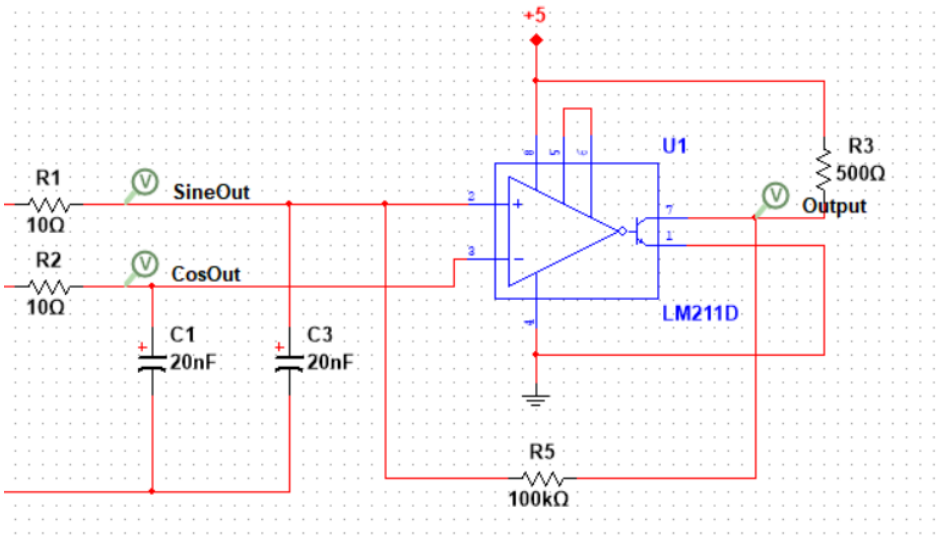


Figure 73 BPSK demodulator comparator stage

The implemented circuit using the result of simulations is shown in Figure 98 included in the appendix section. It worked as expected in the actual evaluations.

For the VCO part, a *CD74HC4046* [136] phase-locked loop IC is used. *CD74HC4046* consists of two internal phase comparators and a VCO. The two comparators have distinct features and properties, which can be studied in [137].

In Figure 74, the implemented circuit is shown. There is the option to choose from two internal phase comparators using a solderable jumper (J1). In the BPSK demodulator, it is important to lock on the preamble sequence phase and then use the locked clock to demodulate the data bits. However, CD74HC4046 does not include this feature, and it continuously tries to lock on the receiving waveform's phase. To solve the issue of the continuous locking and to be able to perform lock only on the preamble sequence, a gating circuit was implemented to disconnect the phase comparator from the VCO input to keep the generated clock fixed. To do so, the *PhaseComparator_Out* goes through a AND gate (U25A) along with *VCOPhaseCheckEnable*. The *VCOPhaseCheckEnable* is controlled by the microcontroller on the board. The reason for AND gate is to be able to control the phase comparator connection to VCO input, and after acquiring a lock on the preamble signal, the AND gate disconnects the PhaseComparator_Out from the *VCOIN* to keep the frequency and phase fixed for the rest of the reception. However, later in the evaluations, it was found that this was not the optimum design choice. By disconnecting the PhaseComparator_Out from VCO input, a zero voltage applies to the VCO input, which forces the VCO frequency to run at the minimum configured frequency, which is irrelevant to the input signal frequency and hence it is not usable to demodulate the data bits.

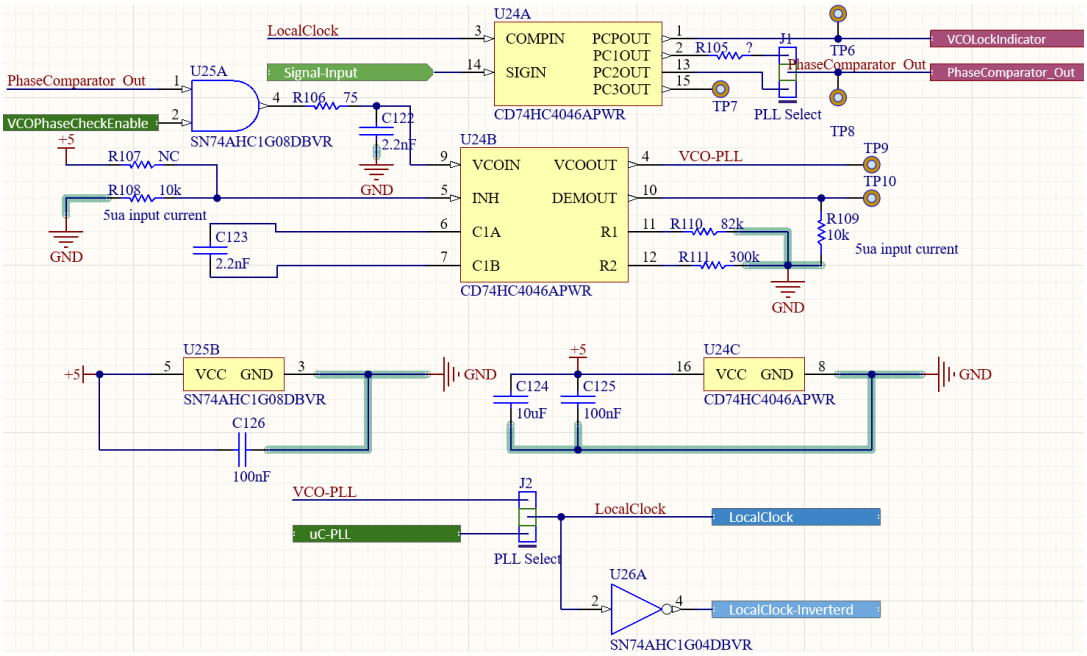


Figure 74 PLL circuit

4.3.7 OOK demodulation circuit design

Apart from BPSK demodulation, an OOK demodulation circuit is also considered and implemented in the prototype board due to its low power consumption and simple demodulation circuit. In OOK, for transmitting logic-zero bits, the transceiver does not consume any power, which makes it power efficient. This modulation technique has also been used as the primary modulation technique in various industrial and research modems, including the latest compact *AHOI* modem [37]. The demodulation circuit for the OOK is shown in Figure 75. The circuit is a combination of a diode-based envelope detector at the desired frequency followed by a Schmitt trigger comparator. In the envelope detector circuit, when there is an input signal, the current flows through the diode (D3) and charges the immediate capacitor (C142); the capacitor discharges through (R123) constantly. When there is an input signal, the capacitor is charged continuously by the input signal, and when there is no input signal, it discharges fully through (R123). A comparator circuit compares the capacitor voltage and produces relevant logic-one

and logic-zero based on the capacitor voltage level. The value for a capacitor (C142) and (R123) is specified using a simulation in a *MultiSim* environment.

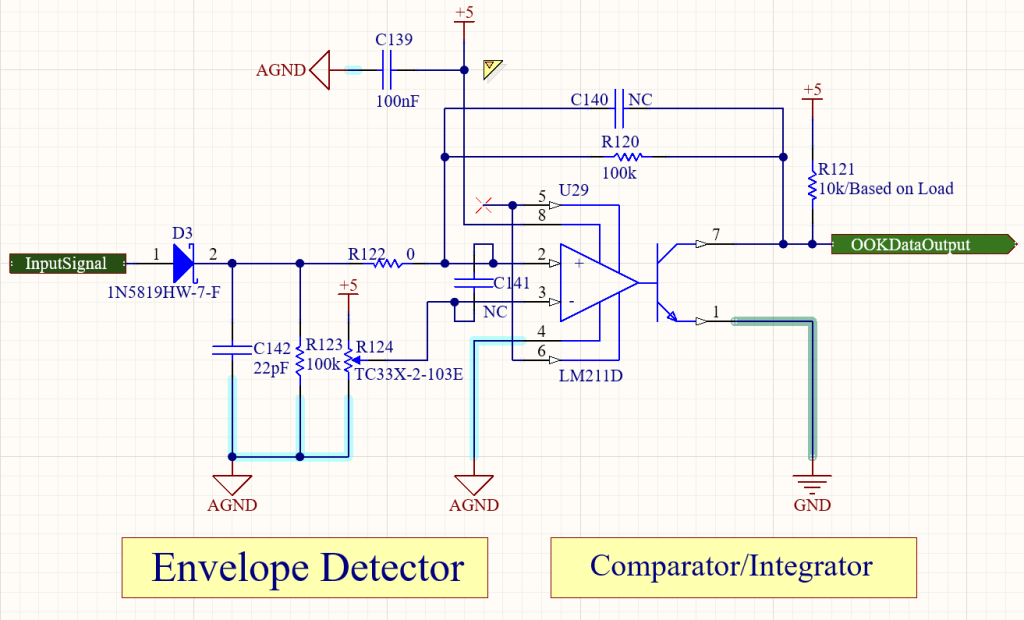


Figure 75 OOK demodulation circuit

In the simulation result's figure, Figure 76, the blue line is the signal received by the receiver hydrophone, which then goes through the filters and amplifiers, and it gets digitalized and finally feeds into the envelope detection circuit. The envelope detection circuit output is shown in red, which then goes through a Schmitt trigger comparator and produce the recovered data, shown in green. The evaluation of the circuit in the real environment was as expected, and OOK was selected as the optimal approach for communications given the system requirements due to its low power requirement and simple and low power demodulation circuit.

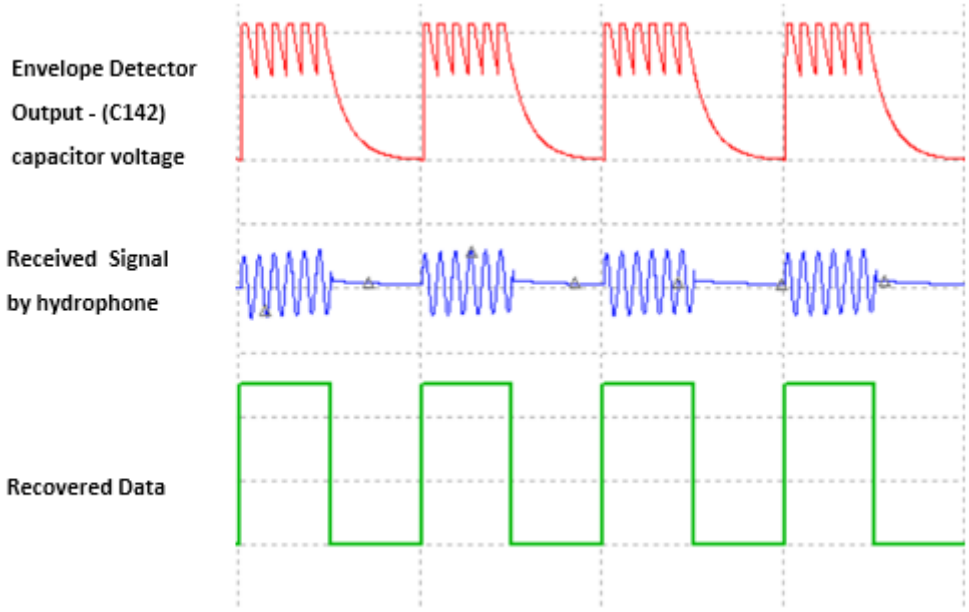


Figure 76 Envelope detector simulation

4.3.8 Direct sampling of the received signal

In addition to the implementation of a hardware-based demodulation scheme, the possibility of software-based demodulation was also investigated. The software-based demodulation enables the possibility to demodulate various modulation schemes without the need to have special hardware circuitry. There are also demodulation techniques that can implement only in software, e.g., chirp demodulators. Software-based demodulation also allows using fewer components, lessening the hardware costs. However, the main disadvantage of this technique is that it needs a high-speed processor and a very efficient Analog to Digital converter circuit, which in both cases can prove to be expensive.

According to the Nyquist sampling theorem [116], to eliminate the aliasing effect in the sampling of the analog signals, the signal needs to be sampled at least at twice the maximum frequency of the input signal. In this design, the minimum sampling frequency should be 1040 kHz to capture the modulated signal at 520 kHz. However, there might be some high-frequency noises in the captured data caused by the underwater environment. So, it is usually suggested as a useful rule of thumb to oversample the signal at higher frequencies to improve the signal-noise ratio and improve the resolution of the reconstructed signals [138]. Hence, it was decided to take samples at ten times the nominal frequency (520 kHz for possible miniaturized piezo tubes), which would be 5 MSPS (Mega Samples Per Second). The selected microcontroller's ADC, *STM32H750VBT6*, can sample up to 3.25 MSPS in 16 bit mode [139], which might not be sufficient. Hence, it was decided to use *LTC2315-12*, a 12-bit, 5 MSPS serial sampling ADC [140]. It just requires decoupling capacitors, and it can be read through the SPI protocol.

To be able to read the ADC data at 5 MSPS with minimum load on the microcontroller, Direct Memory Access (DMA) feature on *STM32* has been used, which off-load the microcontroller and manages the data transmission, reception, and buffering the data.

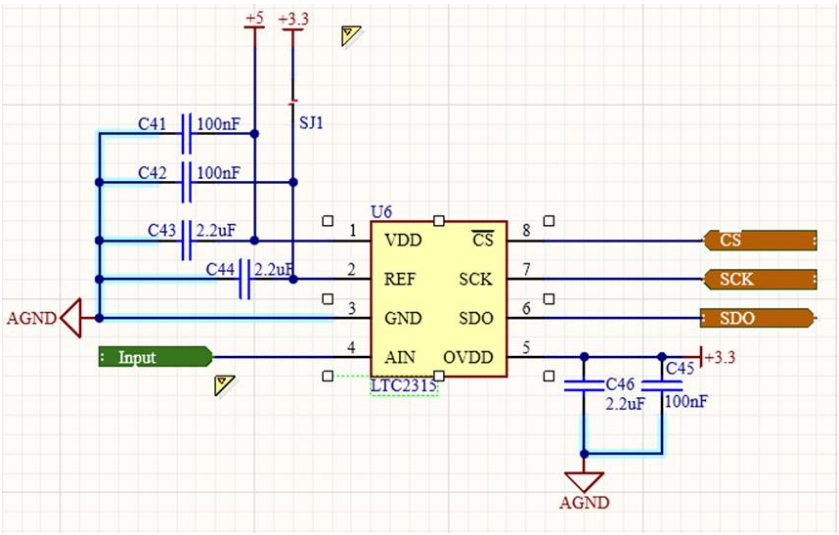


Figure 77 LTC2315 ADC IC

4.3.9 USB communications

As discussed previously, the proposed characterisation prototype board has a complete set of data filtering, amplification stages; as in some potential scenarios, it would be beneficial to be able to record and transfer the underwater signals to a host controller (PC, laptop, etc.) for logging and post-processing to determine the Signal-noise-ratio factor, possible noise sources and signals behaviour underwater. Therefore, a parallel-interface USB controller is considered on the board. Having a parallel interface USB controller eliminates the related serial transmission overhead and reduces the impact of USB transmission on the microcontroller. For this purpose, the *FT232HL* [141] Multipurpose UART/FIFO USB controllers was used that can handle up to 480 MBits/s.

To receive the data on a PC or any other Host controller (SOCs), an efficient program is required to capture the data and save the received data onto that PC. For this purpose, a *Node.js* [142] program was developed to receive data through the USB and save the file in a binary format. Node.js is an open-source, cross-platform JavaScript runtime that is well-known for its high-throughput IO operations. For visualizing the data and performing basic data processing, the *PulseView* [143] environment was used. *PulseView* is also an open-source application that can interface with various data loggers and oscilloscopes and visualize captured data. It also has the ability to read from raw binary files, which was used to visualize the captured data. In Figure 78, the *PulseView* environment while analyzing an OOK signal from the IMPAQT receiver is shown.

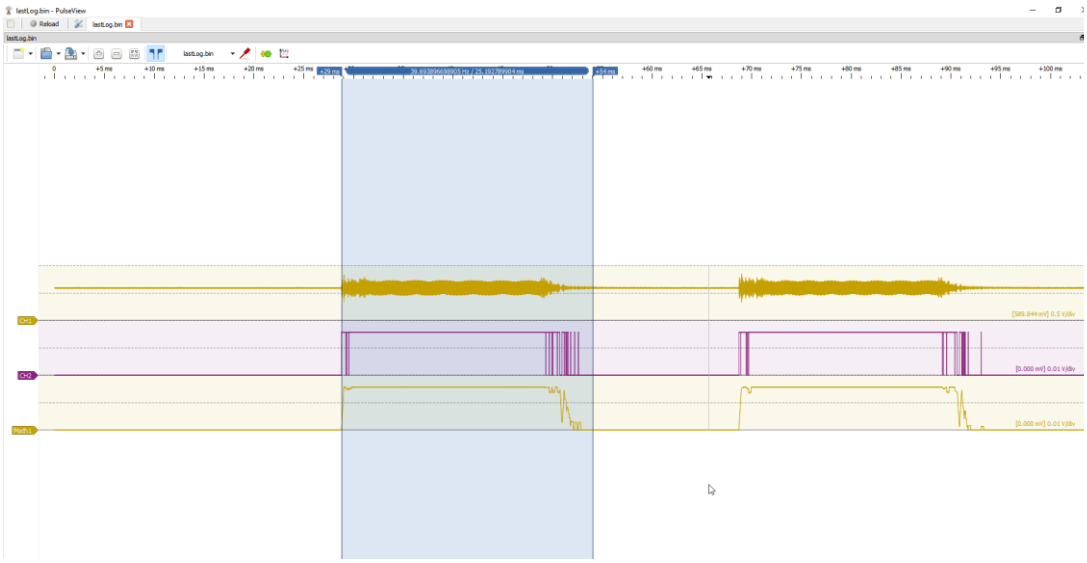


Figure 78 PulseView environment - an OOK signal analysis captured by IMPAQT receiver

4.3.10 Data storage options

To provide an offline logging capability for the IMPAQT receiver board, a variety of data storage solutions were implemented. An SD Card was used for saving the received information for future extraction from the board. It is useful for remote deployments where there is no host controller (PC, Laptop, etc.) present to capture the data or there is no way to transmit the data out of the board. The SD Card connects to the microcontroller using the *SDIO* [144] interface of STM32 microcontrollers.

There is also a parallel SRAM available on the board to act as a temporary highspeed storage. It can be used as a buffer for future machine learning implementation on the board, or it can act as temporary storage for USB communications where required. The associate part number is *IS62WV25616DALL* [145].

4.3.11 Received information transfer interfaces

There is an HC-05 Bluetooth module [146] connector present on the board, as well as nine general-purpose pins, which can be used as SPI or UART connections

for adding other modules to the IMPAQT receiver node. A *LoPy4* module has been used as the LoRa transceiver on the board to transmit data to Data Aggregator Systems (DAS). The LoRa module is configured with a frequency of 868 MHz, channel bandwidth of 125 kHz, spreading factor of 12, preamble symbols of 6 and transmission power of 14. These values are set based on the supporting longest range possible with the help of the article published by Mark Zachmann [60]. The UART protocol has been used for the communication between the onboard microcontroller and *LoPy4* board. There is also an IrDA transceiver, *TFBS4650*, to communicate with the IMPAQT transmitter nodes if required. The HC-05 and IrDA transceiver is shown in Figure 79.

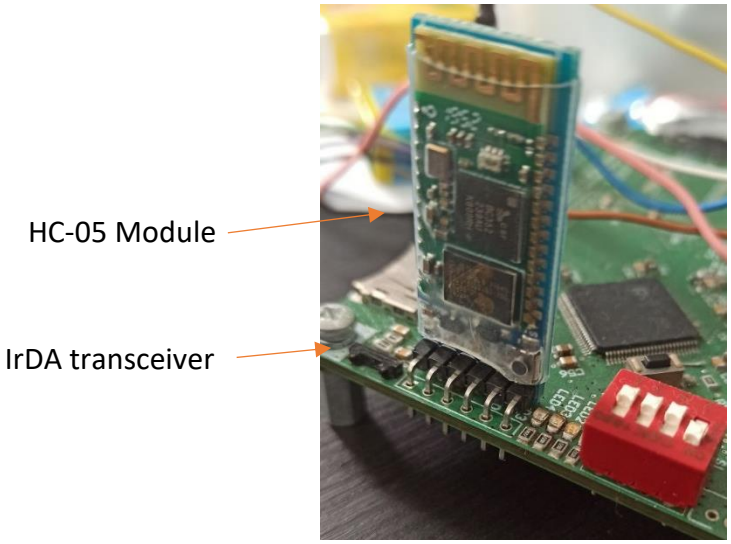


Figure 79 HC-05 and IrDA transciever on the IMPAQT receiver node

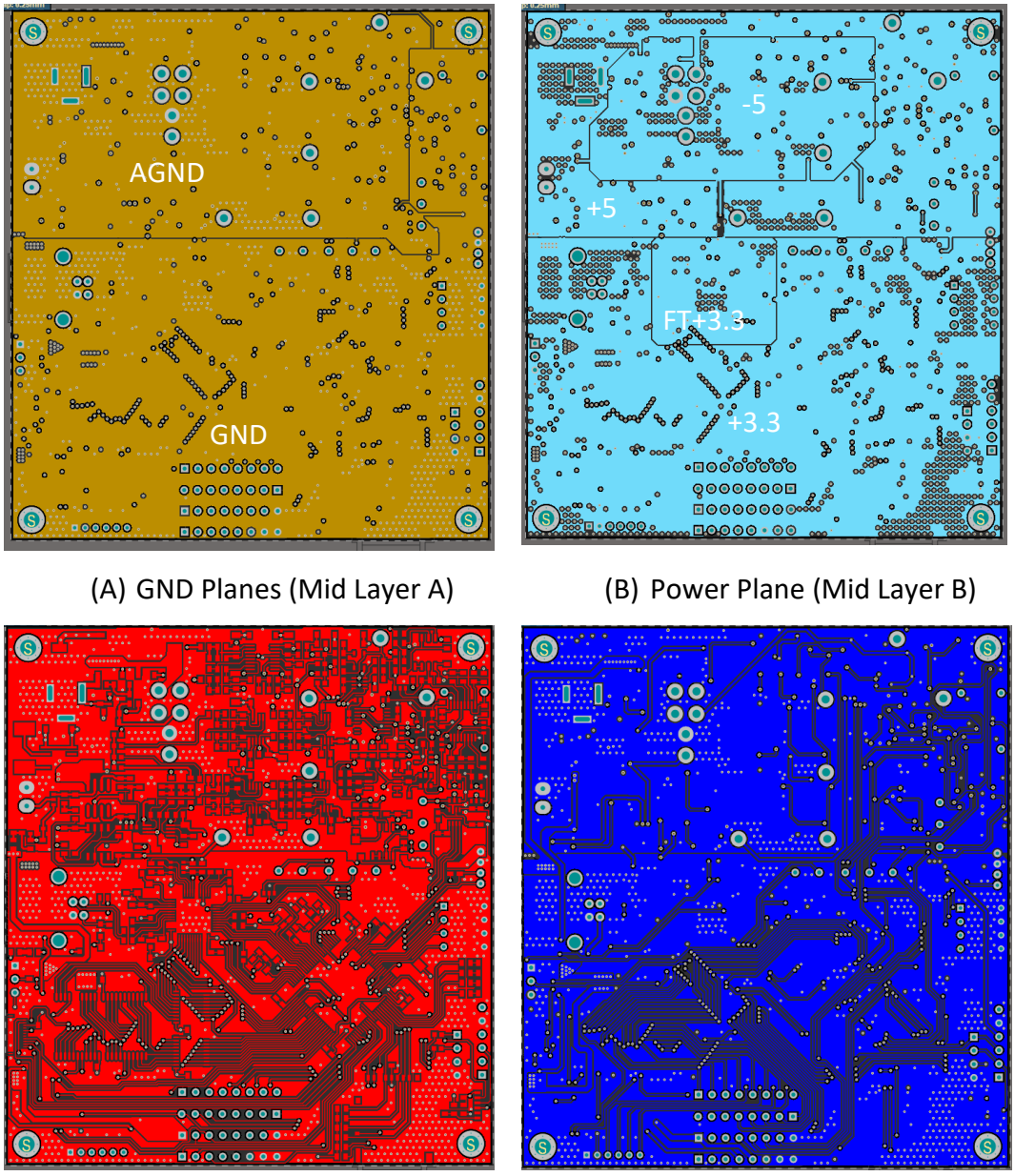
4.3.12 Microcontroller selection

To cater for all envisaged use case requirements, the IMPAQT receiver node is packed with various circuit development building blocks as described in the previous sections, which need to be controlled. Also, there is a direct analog signal sampling functionality on the board, which can be used in the digital demodulation of the received signal, and it requires an efficient microcontroller to sample the analog signal and perform digital signal processing. Therefore, the microcontroller

needs to be high-performance to be able to manage the various tasks. It was decided to use the *STM32H750VBT6* microcontroller. This microcontroller has 100 pins, provides enough general-purpose IOs to perform the required functionalities. It can run up to 480 MHz and provides a variety of functionalities like timers, DMAs, and 35 communication peripherals; further information can be obtained from [147]. As there is no limitation on the size of the receiver board, there is a variety of debugging and experimental tools fitted on the board to simplify the evaluation process. There are four selectable dip switches on the board, four LEDs, nine general-purpose IOs apart from the circuits that are already discussed.

4.3.13 Acoustic receiver board design

The overview of the schematic is shown in Figure 99, included in the appendix section. There are various amplifiers and filters on the board that are sensitive to small variations in the signals; Therefore, a minimal noise on the board can get amplified to a higher level noise which can affect the demodulation and filtering of the input signals. The PCB substrates were designed in four layers. As shown in Figure 80, The top and bottom layers mainly include the signals and communication wires. The two middle layers include the *GND* and Power planes. Having power planes in the middle layers will help in decoupling the voltage levels throughout the PCB, as two immediate middle power planes with different polarities will act as a capacitor, helping rejection of unwanted noises on the circuit and power lines. In Figure 80, the layers of the IMPAQT receiver board are shown. The *GND* plane is split into two parts, the top part is *Analog_GND*, and the bottom plane is *GND*. The reason for this decision is to separate the analog components *GND* from the digital ones, as digital components, due to their rapid change nature, can affect the analog signals performance. This is a well-known technique to separate sensitive components and their power supplies from other components (Digital circuits, High-current circuits, etc.). In this technique, the analog power planes are separated from each other, and they are only connected at a single point. More information about this noise reduction technique can be found in [148].



(A) GND Planes (Mid Layer A)

(B) Power Plane (Mid Layer B)

(C) Signal Plane (Top Layer)

(D) Signal Plane (Bottom layer)

Figure 80 The IMPAQT Receiver board layers decomposition

The final 3D preview of the board is shown in Figure 81, and the decomposition of the circuits is shown in Figure 82.

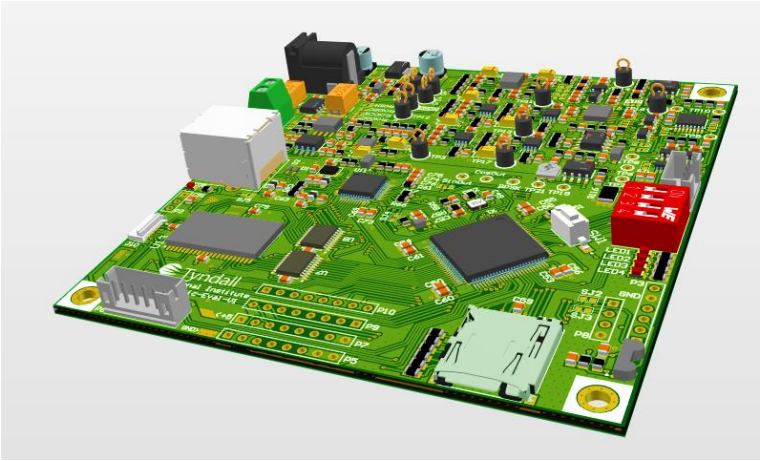


Figure 81 3D view of the IMPAQT receiver board



Figure 82 Annotated 3D view of the IMPAQT receiver board

5 Transceiver Systems Characterisation Tests and Results

As discussed in Chapters 3 and 4, two approaches were explored to develop an underwater communication platform using electromagnetic waves (a feasibility study to investigate if EM transmissions over very short ranges were possible using sub-GHz frequencies) and acoustic waves (for longer range underwater sensor network applications). Prototype systems for both approaches were developed, tested and characterized in the lab prior to underwater deployments to ensure functionality. As estimated by theoretical models discussed in Section 3.1.1, the electromagnetic waves are expected to get attenuated heavily underwater, while acoustic waves are expected to propagate well underwater. In this chapter, the results of the design and deployments of the two transceiver systems (Electromagnetic communication and acoustic communication) are discussed.

5.1 Underwater electromagnetic communication test results

According to the theoretical models for underwater EM propagation [24], [41], which are discussed extensively in 3.1.1, it is predicted that at 868 MHz frequency range, the transmission range of LoRa RF transceivers is limited to 110 cm in freshwater and less than 13 cm in seawater. While electromagnetic communications showed promising results while tested in the terrestrial environment, as it immersed into the water, the communication range dropped significantly as already expected and estimated by theoretical models. The test was carried out near Tyndall National Institute [56] in *Cork* [51.898736, -8.483184] in a freshwater river, it was observed that at 100 cm distance between transmitter and receiver the percentage of packet drops increased significantly and at 120 cm the communication was fully blocked proving that this type of wireless communications underwater is suitable only for extremely short range in freshwater.

5.2 Underwater acoustic communication results

The proposed design for the underwater acoustic transmitter node, described in Section 4.2, was implemented on a 4-layer PCB with the dimension of 5 cm x 3 cm and the proposed design for the receiver board was implemented on a 4-layer PCB with the dimension of 9.1 cm x 10 cm. The developed circuits are shown in Figure 83.

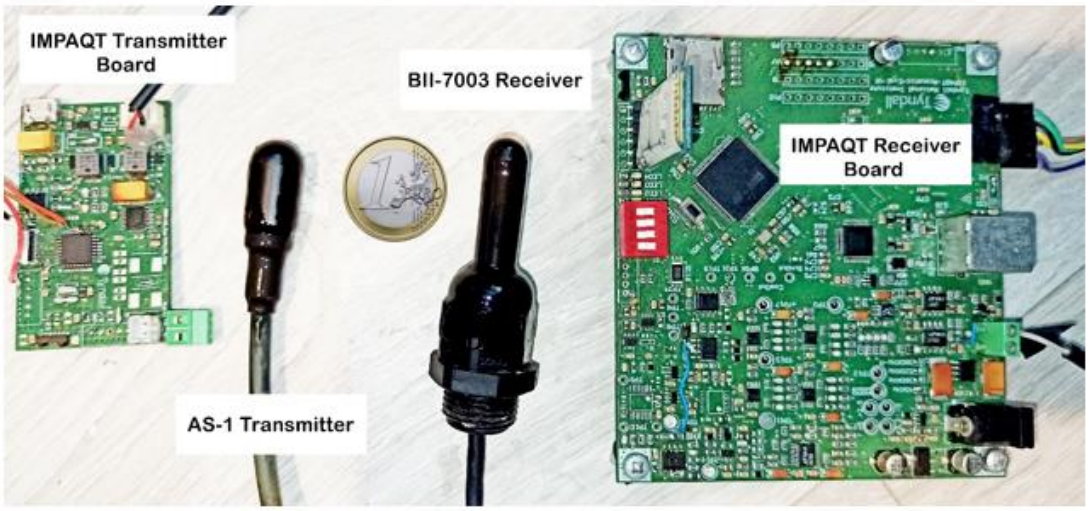


Figure 83 The IMPAQT Telemetry platform boards

5.2.1 Functionality tests results of the acoustic telemetry platform

To verify the functionality of the acoustic telemetry circuits, each system circuit block (shown in Figure 33, and Figure 56) was populated with components separately and tested in isolation to verify their functionality individually before full integration testing. One of the main objectives of the transmitter board was to boost the voltage to the required voltage (20 V) and modulate this signal using the microcontroller and the analog switch on the board, as described in Section 4.2. This objective was successfully achieved, as can be seen in Figure 84, where the screenshot of the traces captured by a *Hantek 2D72* oscilloscope [149] shows a blue line that indicates the 3.7 V input voltage supplied from the LiPo battery. The yellow line shows the transducer input terminal, and as it can be seen, it is rated at 20 V,

and it is oscillating at 42 kHz. This measurement indicates that the boost converter is boosting the voltage to the required level, and analog switch is controlled by the microcontroller successfully.

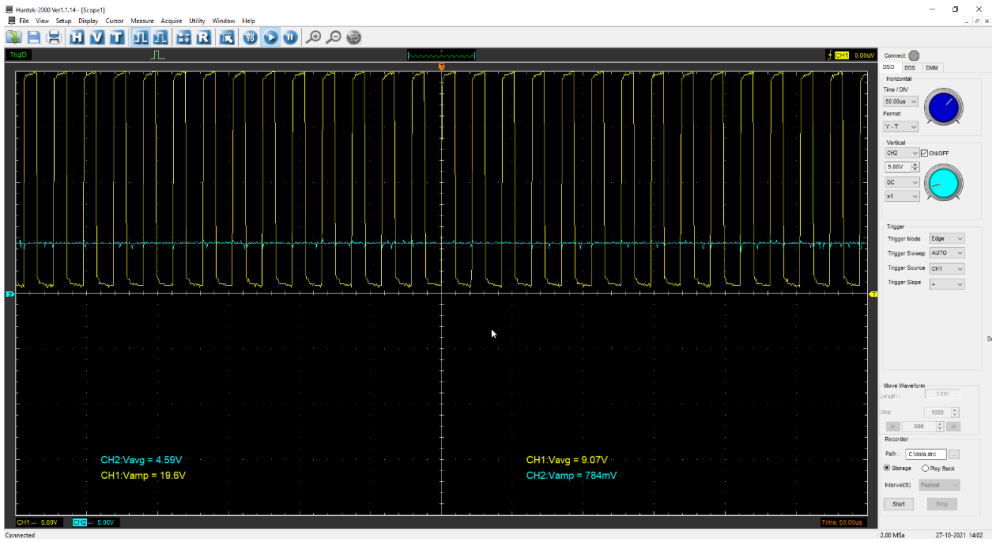


Figure 84 Transmitter boost convertor and modulator evaluation

The next objective of the transmitter board is the ability to perform the OOK modulation, which was the selected communication protocol (discussed it 4.3.7), and as is shown in Figure 85, this objective has been achieved. Figure 85 shows the transmission of the “1010101101000001” bits stream.

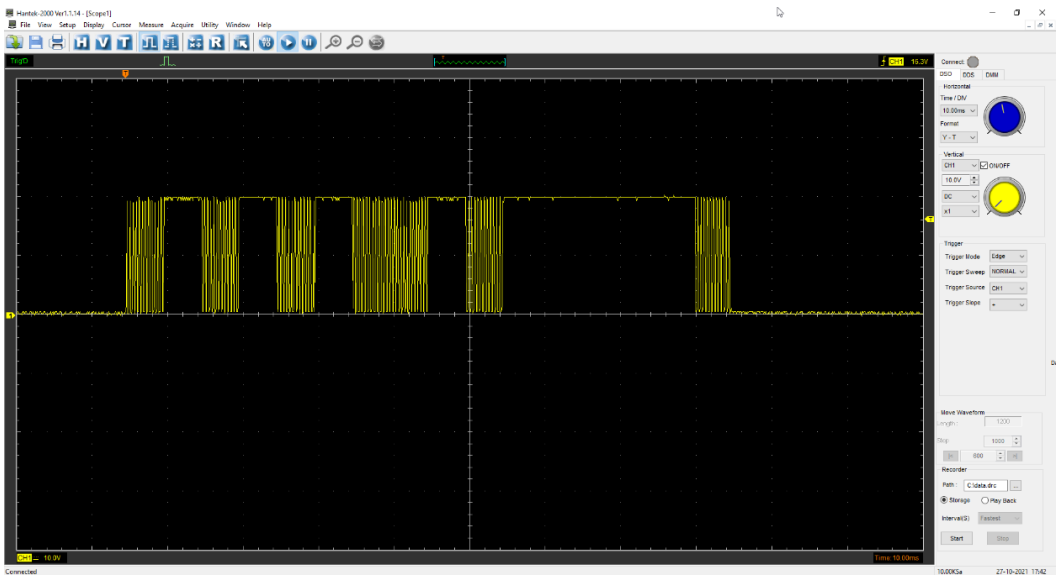
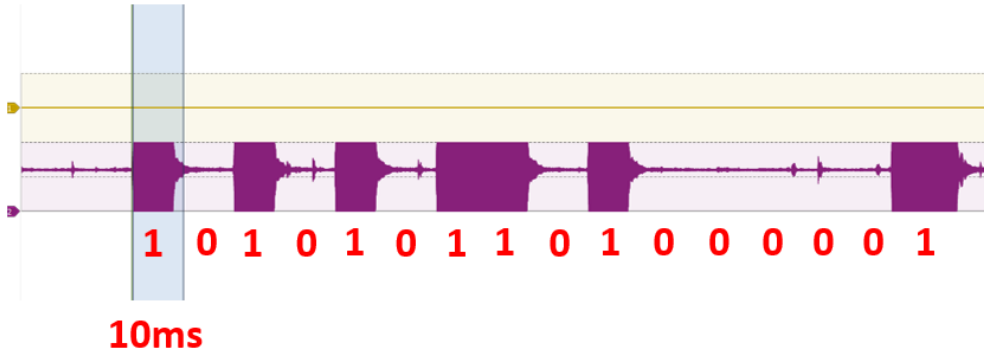


Figure 85 OOK Modulation on the transmitter side

On the receiver side, the transmitted signals are received, filtered, and amplified, and it is shown in Figure 86. The figure shows two types of transmitted signals, software damped signal as described in Section 4.2.7 is shown as (A) and not damped signal shown as (B), where the transmitter didn't use the software damping. As it can be seen, the software damping method effectively controls the damping by dynamic duty cycle control discussed in Section 4.2.7.



(A) Software damped transmitted signal



(B) Not damped transmitted signal

Figure 86 Filtered analog signals on the receiver side

On the receiver board, the amplification stages and filtration stages worked as expected. Each step is depicted in Figure 87, the signal recorded while the transmitter and receiver were 30 cm apart in a water bucket. As it can be seen, despite the receiver and transmitter situated close to each other, the hydrophone output is very weak (in the range of a few millivolts). The signal gets filtered and

amplified to 5 V at the last stage, which then goes through the OOK demodulator to extract the data bits.

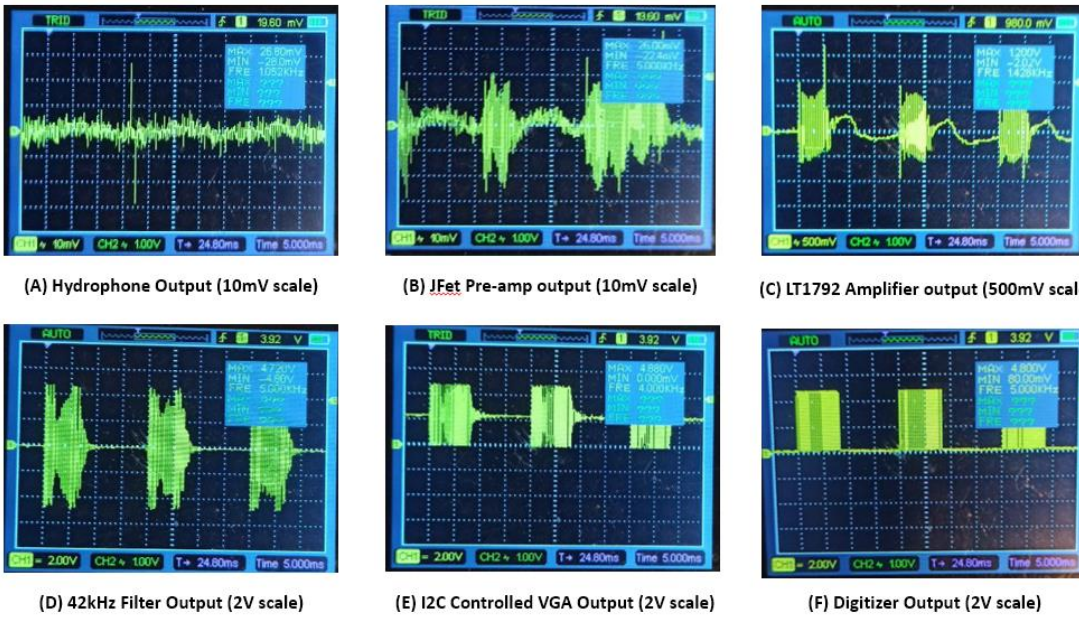


Figure 87 Receiver board filtration, amplification stages results

The OOK demodulator output is shown in Figure 88. It is important to note that up to this stage, all the demodulations have been done using hardware components.

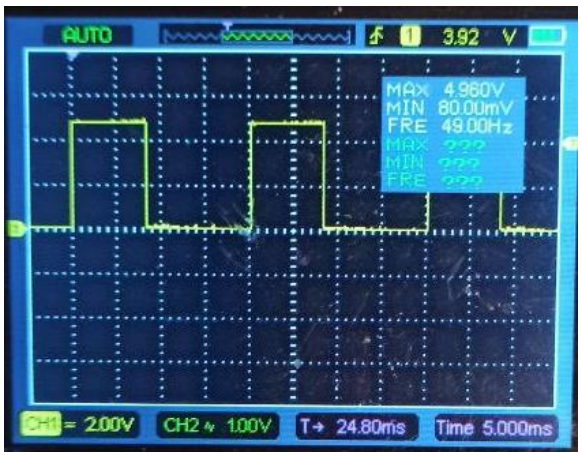


Figure 88 OOK Demodulator output

Regarding the data transmission rate, initially, a test in the air was conducted using air piezo transducer driving at 40 kHz and 200 bit/s achieved without software damping. By changing the medium and transducer to be able to work underwater, the bitrate dropped to 40 bit/s, and with fine-tuning of the filters and amplifiers, it increased to 70 bit/s. Finally, using the software damping technique, 100 bit/s is achieved, as it is shown in Figure 88, and each bit is approximately 10 ms, which is equal to 100 bit/s.

5.2.2 Transceiver system open-water test

In order to evaluate the performance of the proposed system in a more realistic environment, an SNR measurement in the Cork Harbour Marina pier (51.845202, -8.332210) has been carried out. When the receiver gets exposed to a body of open water and the distance between transmitter and receiver increases, the amplitutde difference between the signal level and the noise level in the received signal decreases. In addition, there are additional noise artefacts expected due to sediment or impurities in the open water, wave motion or other sources of acoustic noise interference in the open water that might affect the signal-noise ratio. The signal to noise ratio indicator defines the signal reception quality, and it is used to evaluate the system communication performance. In order to measure the SNR, the transmitter and receiver were immersed in a seawater environment representative of an IMTA site in Cork Harbour. The transmitter was transmitting a stream of logic-one bits, and the received signal for the whole process was being recorded by the receiver system and a PC connected to it. Later, the recorded data was manually processed to calculate the SNR value. The SNR values were calculated at 5 m, 10 m, 15 m, 25 m, 35 m, 50 m, 70 m, and 92 m checkpoints. In order to determine the SNR value at each checkpoint, initially, the transmitter was placed in the water, and it was programmed to transmit a modulated “logic-one” signal for 10 seconds while the receiver was already submerged in the water, and it was recording the input signal level. The main signal level was estimated by averaging the input signal level over the recorded 10 second period. Then the transmitter was taken out of the water and

switched off while the receiver was still inside the water and recording the input signal level. The input signal, in this case, is essentially the circuit noise and the acoustic noise of the environment with a frequency in the pass-band region (6 kHz) of the 42 kHz filter (discussed in Section 4.3.3). Similarly, the noise level was estimated by averaging the input signal level over the recorded 10 seconds period without the transmitter node in the water. This procedure has been repeated for each checkpoint to measure the SNR value. The test environment is shown in Figure 89.

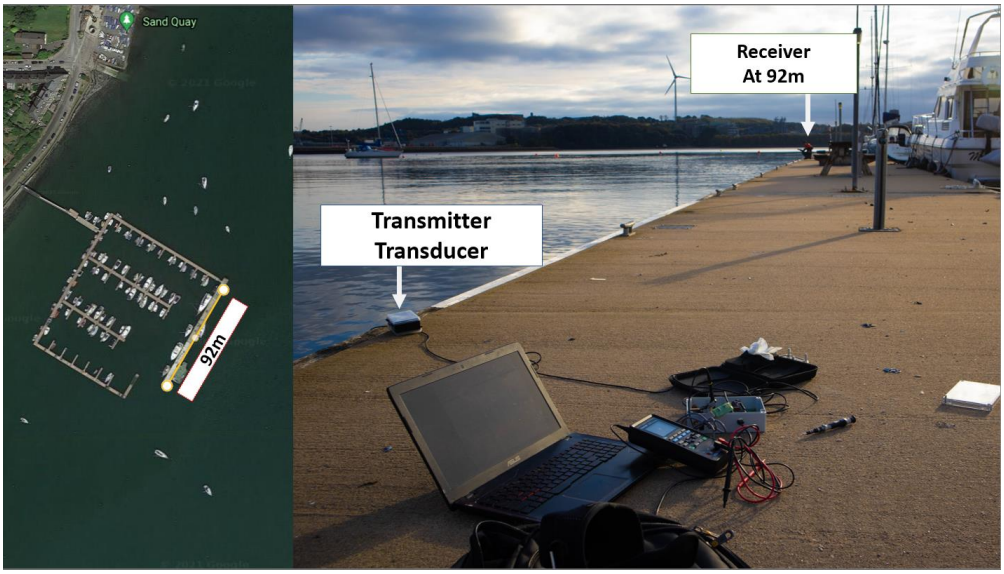


Figure 89 Cork Harbour Marina pier deployment

This entire test procedure has been carried out four times at the pier to ensure the repeatability and reliability of the measurements during the proof of principle demonstration trials. The measurements were carried out twice at a depth of 40 cm and twice at a depth of 100 cm to study the impact of depth on the SNR value. A similar experiment was also performed in a water bucket and recorded to compare with the data recorded from the pier environment to determine the acoustic noise level from the pier environment in the 42 kHz region, which was negligible.

Figure 90 depicts the signal-to-noise ratios obtained versus the distance between transmitter and receiver in the ocean environment. The G on the graph

indicates the Gain percentage. By increasing the gain, both the noise level and signal level get amplified. It is essential to increase the gain when the distance between the transmitter and receiver increases to be able to detect the transmitted signal. The 100% gain in the receiver board is equivalent to 52 dB, and 6% is 3.12 dB. As it can be seen, the signal was recorded at depths of both 40 cm and 100 cm, and it shows that by immersing the communication system deeper into the water, the noise level reduces slightly, probably due to less noise from the surface and terrestrial environment.

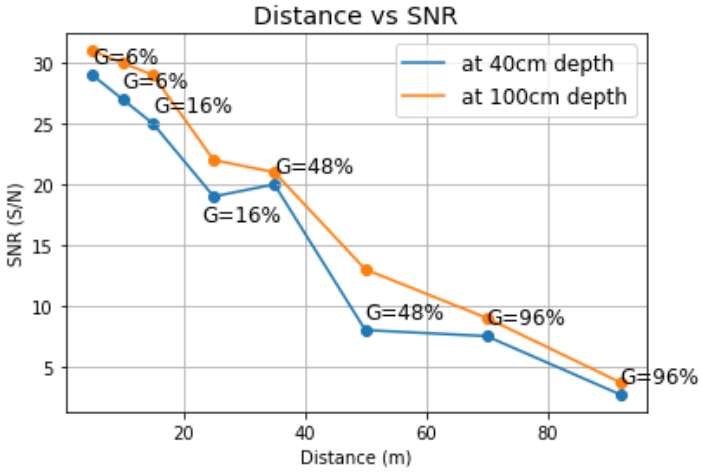


Figure 90 SNR Measurements

A relevant dataset of the signal recordings and ocean noise level is accessible in [150].

5.2.3 Transmitter node battery life

As discussed extensively in 4.2.10, the transmitter node's power consumption has great importance in the IMPAQT project since it directly impacts the maintenance scheduling and the user experience. The estimated power consumption and the practical power consumption measurements are shown in detail in Table 6. To summarize the measurements, the transmitter consumes 10.5 µA in the sleep mode, 65650 µA in the transmitting logic-one, and 1606 µA in transmitting logic-zero. Such a lower power transmitter node has not been previously reported in the literature.

STM32CubeMX power consumption calculator was used to estimate the battery life of the transmitter tag based on the measured current consumptions.

According to Table 6, and the chosen battery (LP503562 [108]), and transmission cycle of 1 data byte every 5 seconds (1 preamble byte + 1 data bytes), considering that two-third of the bits are logic-one, the battery will last one month and 4 days. By increasing the transmission period of the same data to every 30 seconds, the battery life will be 6 months and 18 days. The estimation in the STM32CubeMX software is shown in Figure 91.

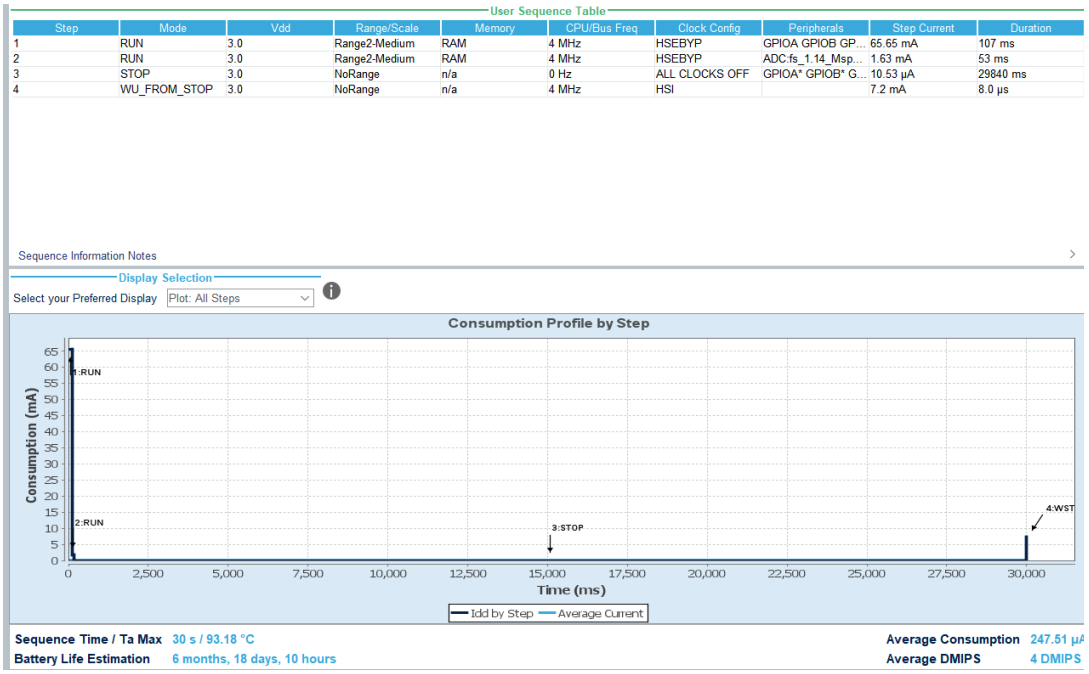


Figure 91 STM32CubeMX Battery life estimator

5.2.4 Integration test of the transmitter node with external sensor

To verify the integration capability of the novel transmitter node, the transmitter node was integrated with the novel electronic tongue sensor developed by the IMPAQT project partners, researchers from *Tor Vergata University of Rome* (*UNITOV*). The novel electronic tongue sensor is a microfluidic sensor that can measure water parameters (e.g., Nitrate and Phosphate) in-situ and with the help of the IMPAQT transmitter node, it can transmit the measured properties data to the remote logging unit (IMPAQT receiver board). The UART protocol is used as part of the communication protocol along with two *Ready* and *Wakeup* pins. The IMPAQT

transmitter node interrupts the *UNITOV* sensor sleep by setting *Wakeup* pin to high level followed by an "S\r\n" string transmission via UART, and then they can communicate as it is shown in Figure 92. The two systems are shown alongside each other in Figure 93.

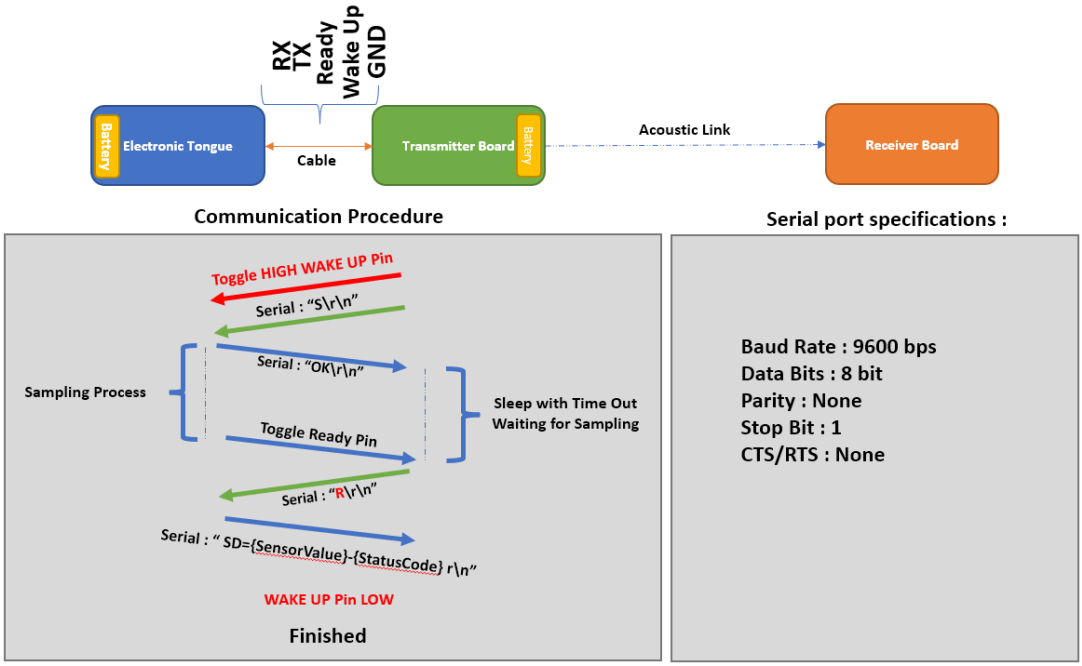


Figure 92 The IMPAQT Transmitter node and The Unitov electronic tongue sensor integration protocol

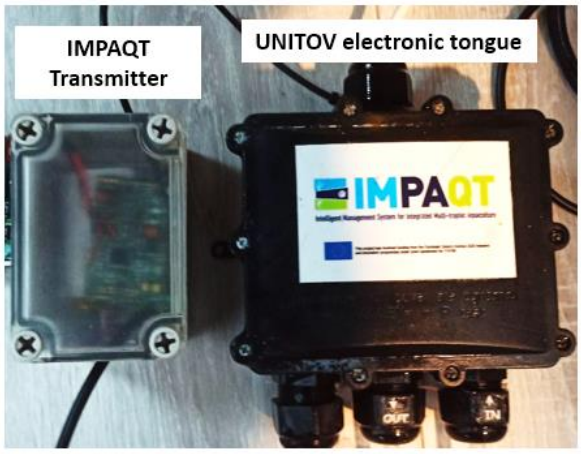


Figure 93 the IMPAQT transmitter node and UNITOV electronic tongue

6 Conclusion and future works

Throughout this thesis, and in particular, in Chapter 1, the importance of marine environmental monitoring is discussed, and the novel technologies developed to meet the needs of marine sensing are discussed. The particular requirements aligned with the IMPAQT project use case to monitor IMTA sites are defined. In Chapter 2, the state-of-the-art in the research area of marine monitoring systems is studied. Despite advancements in the field, the literature review identified a gap in the current state-of-the-art in this area in so much as it concluded that still there is a lack of general-purpose wireless underwater modem, which offers a low-power, low-cost module that can be integrated into other products and transmit as well as store data, similar to the general-purpose terrestrial RF modules. By evaluating electromagnetic communications underwater in Chapter 3, it is concluded that it is not suitable for underwater communications other than extremely short-range applications, as the communication gets blocked at approximately 100 cm range at 868 MHz transmission frequency, using high-power *SX1276* LoRa modules [51]. Using lower frequencies (i.e., 168 MHz) is also not practical due to long antenna requirements making them unsuitable for many deployment situations requiring miniaturized systems. In Chapter 4, the potential for an alternative longer-range underwater communications system using ultrasonic waves was investigated by evaluating the effective parameters in acoustic communication underwater, and finally, the novel IMPAQT ultrasonic telemetry platform design has been proposed. The proposed ultrasonic transmitter using an acoustic transmitter and a gateway buoy can help farmers and researchers to monitor and analyse the underwater environment wirelessly. It also enables the researchers to develop sensors and deploy them in the water without the need for a cable to be connected.

To evaluate the proposed ultrasonic system, a pair of transmitter and receiver characterisation boards were designed and manufactured. The transmitter was designed to be able to run on a single LiPo battery cell. It boosts the battery voltage to the required level (up to 20 V) so as to drive the hydrophone with either OOK or

BPSK modulation schemes using the boosted voltage. In most marine monitoring and sensing systems, two-way communication is not necessary, and only the sensors data need to be transmitted to the logging nodes. Consequently, the IMPAQT transmitter node was designed to be transmitter-only, which helps to reduce the node's dimension and power requirements. Regarding the battery life of the tag, based on the user requirements, it can last up to 6 months with transmitting 1 data byte every 30 seconds on the designated battery. The transmitter node's evaluation board dimension is 33 mm x 55 mm. This board is designed to be easy to modify, hence the components are conventional footprints and easy to solder, and the resistors and capacitors footprints are large. A variety of standard sensor interfaces were designed into the transmitter to make it compatible with a variety of COTS marine sensors.

The receiver prototype board was designed to be able to detect, amplify and demodulate signals at three different frequencies (40 kHz, 380 kHz, 520 kHz) to be able to evaluate various piezo transducers materials. It features an I^2C controlled variable gain amplifier, which can change the signal amplification level digitally to make it suitable for both short and long-range applications. It also includes a high-performance *STM32H7* microcontroller to sample and process the signals. Alongside the microcontroller, there are BPSK and OOK demodulation circuits on the board. The OOK circuit worked as expected, and it has been selected as the preferred modulation method, as it is easier to demodulate and it consumes less power compared to other modulation techniques described in 4.2.6. There is an *FT232H* USB controller on the board, which can transfer the captured signals to another host controller (PC) in real-time to perform post-processing if required to determine the Signal-noise-ratio factor, possible noise sources and signals behaviour underwater. The receiver prototype board met the objectives defined.

The main novelty of this work is **its miniaturized size**, **low-cost and low-power transmitter design** in a **one-way communication platform**, and that it is designed to be a **general-purpose telemetry system** and **attachable to other sensors** and modules with multiple sensor interface options. Such a system has not been

previously reported in the literature. It can replace the sensor cables underwater, which reduce risks and the cost of deployment and maintenances considerably. It also enables the researchers to deploy many sensors underwater and collect all the information on a single receiver node from a “star network” of such devices with appropriate communications protocols integrated into the systems and, more importantly, observe them in real-time if required. As discussed in Chapter 5, all the mentioned objectives were met in this work, and a fully functional system prototype was developed, tested and characterised. However, there are a number of improvements that can be made to take this system to the next level in the size and performance aspects and investigate the opportunities for the commercialisation of such a system.

6.1 Future Works

In the EM characterisation board, there are various elements that can be improved to extend the communication range. The 169 MHz and possible lower frequencies can be used to evaluate the electromagnetic propagation underwater. The impedance matching of the antenna in an underwater environment needs to be studied, and specifically, the electromagnetic reflection of the antenna underwater can be calculated, and possibly the length of the antenna can be shortened to minimize the electromagnetic reflection of the antennas, which ultimately might increase the communication range.

The proposed prototype boards were designed to be modifiable, hence they are built with conventional SMD parts rather than extremely miniaturized ones. These parts can be replaced with miniaturized ones to minimize the component's footprint on the boards. There are also various alternative circuits to evaluate on each board that can be removed in the final product. Considering that the system worked as expected and best practices are explored, in future, the transmitter and receiver boards can be further miniaturized. The *STM32L082* microcontroller in the transmitter node can be replaced by smaller, less complex alternatives since the

microcontroller-based boost converter is not required anymore, and a processor with fewer capabilities can be considered instead. Additionally, removing the microcontroller-based boost converter frees up a considerable amount of space used by the circuit. It is estimated that the final dimension of the next generation proposed tag would be less than 5 cm x 2 cm.

In terms of power consumption in the transmitter board, there are various components which were used in the prototype systems that can be replaced by other counterparts, which are both smaller and more efficient. For instance, The *MAX1771* [100] boost converter can be replaced by TPS61040 [101], which is 22 mm^2 smaller in area size and consumes 82 µA less current than *MAX1771* when it is in active mode.

It would be a useful feature to include a very simple channel-activity detection circuit [112] on the transmitter node, which detects when the communication channel is being used by other transmitters and postpone the transmission until when the channel is free. This feature, in conjunction with appropriate higher-level communication protocols, would improve the usability of the next-generation device and would reduce the collision of data signals where a significant number of nodes are deployed in a very small area. It also enables the possibility of making a star network of sensing systems.

Regarding the transmission speed, by using a higher frequency range (i.e., 90 kHz range), it is possible to increase the transmission rate. There are also other techniques to reduce the free oscillation of the transducers and decrease the transducer response time, which will ultimately lead to higher transmission speed. For instance, E. Lee et al. [151] discussed a method in their article.

There are some modifications recommended for the next generation of the receiver board, in particular as regards the power regulator circuits. The noise in the 5 V power line was the main contributory factor in limiting the communication range to approximately 100 m can be optimised further. Although the 100 m range is sufficient for the first generation of the novel prototype, mitigating the noise on the

5 V line can increase the communication range and increase the SNR significantly. The 5 V power line requires a linear regulator to stabilize the signal and eliminate the noises. In the current prototype board, the 5 V power line is supplied by the external power source (i.e., mobile charger, USB), and these power supplies are not designed to be used in applications requiring a sensitive power supply for amplification and filtration circuit. These power supplies generally comprise switching circuits that cause a significant ripple and noise in the power lines. The best practice is to use a regulator in the receiver board to clean up and stabilize the power supply.

In these prototype boards, the software algorithms for demodulating the unprocessed signals haven't been used. This can be explored, which might ultimately reduce the number of electronic components on the board. There is also the opportunity to explore the chirp modulation and demodulation, which results in a better SNR and better efficiency of converting electric energy to acoustic energy [152].

The BPSK circuitry and software worked as expected on the transmitter board. However, on the receiver side, opportunities for some further optimisation and circuit modifications associated with the BPSK demodulator were identified. Figure 94 shows the data received on the receiver side and the phase-shifting moment in the received data. The phase-shifting is always followed by a rapid amplitude increase for a short time, where it can be seen in Figure 94.

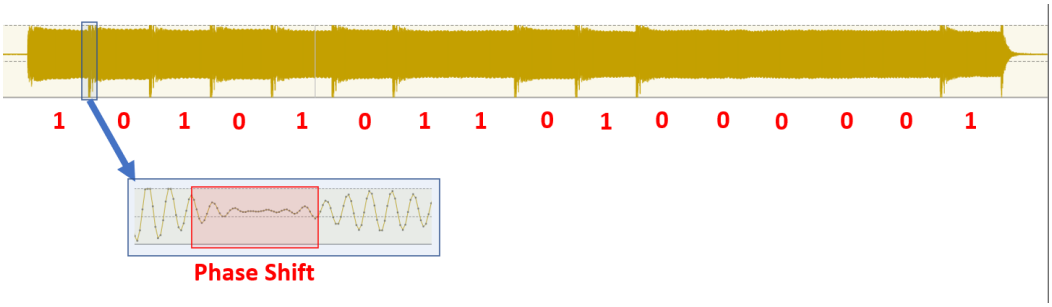


Figure 94 BPSK data received in the receiver side

However, the received signal, shown in Figure 94, couldn't be demodulated using the implemented circuit on the receiver board. In the BPSK demodulation circuit, a modification in the local oscillator circuit is required to be able to lock on the preamble sequence phase and keep it fixed for the demodulation of the data bits. This problem is extensively discussed in Section 4.3.6.

In general, in future prototypes, it is expected that by using 380 kHz piezo materials, the bitrate will increase significantly, which will reduce the overall battery consumption and lead to more frequent data capturing and transmitting. It would also be possible to evaluate the 4^{th} order and 8^{th} order performance at 380 kHz frequency. However, this needs to be confirmed in a future iteration of the transceiver system.

In the communication range aspect, there would be the opportunity to use range-extender nodes and backscatter nodes to improve the communication range of the system. For instance, the work by Ghaffarivardavagh et al. [82] can be used in conjunction with this work to improve the communication range.

There is also the opportunity to use the developed transmitter node in applications other than aquaculture, such as communication and health monitoring of the divers underwater, early detection of underwater oil pipes leakages, controlling underwater vehicles and robots.

References

[1] "World Population Prospects - Population Division - United Nations." https://population.un.org/wpp/Graphs/DemographicProfiles/Line/900 (accessed Sep. 16, 2020).

[2] "Seafood production: wild fish catch vs aquaculture," *Our World in Data*. https://ourworldindata.org/grapher/capture-fisheries-vs-aquaculture-farmed-fish-production (accessed Sep. 16, 2020).

[3] B. Worm *et al.*, "Impacts of Biodiversity Loss on Ocean Ecosystem Services," *Science*, vol. 314, no. 5800, pp. 787–790, Nov. 2006, doi: 10.1126/science.1132294.

[4] R. P. Subasinghe, "Aquaculture: Status and Prospects," *FAO Aquac. Newsl.*, p. 3.

[5] "AQUACULTURE PONDS." UNITED STATES DEPARTMENT OF AGRICULTURE NATURAL RESOURCES CONSERVATION SERVICE. [Online]. Available: https://efotg.sc.egov.usda.gov/references/public/AL/397_cps_AquaculturePonds.pdf

[6] "IMPAQT – Intelligent Management Systems for Integrated Multi-Trophic Aquaculture." https://impaqtproject.eu/ (accessed May 18, 2021).

[7] U. Acar *et al.*, *Designing An IoT Cloud Solution for Aquaculture*. 2019, p. 6. doi: 10.1109/GIOTS.2019.8766428.

[8] "OLCreate: PUB_4560_1.0 Integrated Multi-Trophic Aquaculture and Precision Aquaculture." https://www.open.edu/openlearncreate/course/view.php?id=7116 (accessed Aug. 08, 2021).

[9] "IP Code," *Wikipedia*. Oct. 13, 2021. Accessed: Oct. 20, 2021. [Online]. Available: https://en.wikipedia.org/w/index.php?title=IP_Code&oldid=1049727117

[10] "LoRa and LoRaWAN: Technical overview | DEVELOPER PORTAL." https://lora-developers.semtech.com/documentation/tech-papers-and-guides/lora-and-lorawan/ (accessed Nov. 14, 2021).

[11] Q. Xing *et al.*, "Monitoring seaweed aquaculture in the Yellow Sea with multiple sensors for managing the disaster of macroalgal blooms," *Remote Sens. Environ.*, vol. 231, p. 111279, Sep. 2019, doi: 10.1016/j.rse.2019.111279.

[12] "Mapping the Seafloor with Remote Sensing and Satellite Imagery." https://www.hydro-international.com/content/article/mapping-the-seafloor-with-remote-sensing-and-satellite-imagery (accessed Jul. 29, 2021).

[13] A. Fitzpatrick, A. Singhvi, and A. Arbabian, "An Airborne Sonar System for Underwater Remote Sensing and Imaging," *IEEE Access*, vol. 8, pp. 189945–189959, 2020, doi: 10.1109/ACCESS.2020.3031808.

[14] P. Fairley, "Neptune rising," *IEEE Spectr.*, vol. 42, no. 11, pp. 38–45, Nov. 2005, doi: 10.1109/MSPEC.2005.1526904.

[15] D. Debruyn *et al.*, "MEDUSA: A Multi-Environment Dual-Robot for Underwater Sample Acquisition," *IEEE Robot. Autom. Lett.*, vol. 5, no. 3, pp. 4564–4571, Jul. 2020, doi: 10.1109/LRA.2020.3001534.

[16] "YSI sensors," *YSI sensors*. https://www.ysi.com/parameters

[17] Z. D. Deng *et al.*, "An injectable acoustic transmitter for juvenile salmon," *Sci. Rep.*, vol. 5, no. 1, p. 8111, Jul. 2015, doi: 10.1038/srep08111.

[18] J. Lu *et al.*, "A small long-life acoustic transmitter for studying the behavior of aquatic animals," *Rev. Sci. Instrum.*, vol. 87, no. 11, p. 114902, Nov. 2016, doi: 10.1063/1.4967941.

[19] J. A. Martos-Sitcha *et al.*, "Ultra-Low Power Sensor Devices for Monitoring Physical Activity and Respiratory Frequency in Farmed Fish," *Front. Physiol.*, vol. 10, 2019, doi: 10.3389/fphys.2019.00667.

[20] P. R. de Almeida, T. J. Pereira, B. R. Quintella, A. Gronningsaeter, M. J. Costa, and J. L. Costa, "Testing a 3-axis accelerometer acoustic transmitter (AccelTag) on the Lusitanian toadfish," *J. Exp. Mar. Biol. Ecol.*, vol. 449, pp. 230–238, Nov. 2013, doi: 10.1016/j.jembe.2013.09.015.

[21] C. Brockmann, V. Großer, J. Hefer, S. Guttowski, and H. Reichl, "Miniaturized Implantable Wireless Sensor System for Realtime Measurement of Well-Being of Fishes," in *2010 Fourth International Conference on Sensor Technologies and Applications*, Jul. 2010, pp. 453–457. doi: 10.1109/SENSORCOMM.2010.72.

[22] T. Shaneyfelt, M. A. Joordens, K. Nagothu, and M. Jamshidi, "RF communication between surface and underwater robotic swarms," in *2008 World Automation Congress*, Sep. 2008, pp. 1–6.

[23] M. Vollmer, "Physics of the microwave oven," *Phys. Educ.*, vol. 39, no. 1, pp. 74–81, Jan. 2004, doi: 10.1088/0031-9120/39/1/006.

[24] L. B. Vkbr, "Underwater Radio Communication," *Amateur Radio*, pp. 1–8, 1987.

[25] I. F. Akyildiz, D. Pompili, and T. Melodia, "Underwater acoustic sensor networks: research challenges," *Ad Hoc Netw.*, vol. 3, no. 3, pp. 257–279, May 2005, doi: 10.1016/j.adhoc.2005.01.004.

[26] C. Peres, M. Emam, H. Jafarzadeh, M. Belcastro, and B. O'Flynn, "Development of a Low-Power Underwater NFC-Enabled Sensor Device for Seaweed Monitoring," *Sensors*, vol. 21, no. 14, Art. no. 14, Jan. 2021, doi: 10.3390/s21144649.

[27] S. Ohata, Y. Eriguchi, and K. Ishii, "AquaBox Series: Small Underwater Robot Systems for Shallow Water Observation," in *2007 Symposium on Underwater Technology and Workshop on Scientific Use of Submarine Cables and Related Technologies*, Apr. 2007, pp. 314–319. doi: 10.1109/UT.2007.370796.

[28] Y. Cong, C. Gu, T. Zhang, and Y. Gao, "Underwater robot sensing technology: A survey," *Fundam. Res.*, vol. 1, no. 3, pp. 337–345, May 2021, doi: 10.1016/j.fmre.2021.03.002.

[29] "SeaSmart AS (EN)." https://www.seasmart.no/english.html (accessed Oct. 19, 2020).

[30] "CageSense Wireless Sensors – Water Linked AS." https://waterlinked.com/cagesense/ (accessed Jul. 09, 2021).

[31] F. Murphy, D. Laffey, B. O'Flynn, J. Buckley, and J. Barton, *Development of a Wireless Sensor Network for Collaborative Agents to Treat Scale Formation in Oil Pipes*, vol. 4373. 2007, p. 194. doi: 10.1007/978-3-540-69830-2_12.

[32] "Popoto Modem," *Popoto Modem*. https://www.popotomodem.com/ (accessed Jul. 08, 2021).

[33] "Water Linked AS – Wireless Sense." https://waterlinked.com (accessed Jul. 08, 2021).

[34] "Micromodem :: Acoustic Communications Group." https://acomms.whoi.edu/micro-modem/ (accessed Jul. 08, 2021).

[35] L. Freitag, M. Grund, S. Singh, J. Partan, P. Koski, and K. Ball, "The WHOI micro-modem: an acoustic communications and navigation system for multiple platforms," in *Proceedings of OCEANS 2005 MTS/IEEE*, Sep. 2005, pp. 1086-1092 Vol. 2. doi: 10.1109/OCEANS.2005.1639901.

[36] E. Gallimore, J. Partan, I. Vaughn, S. Singh, J. Shusta, and L. Freitag, "The WHOI micromodem-2: A scalable system for acoustic communications and networking," in *OCEANS 2010 MTS/IEEE SEATTLE*, Sep. 2010, pp. 1–7. doi: 10.1109/OCEANS.2010.5664354.

[37] B.-C. Renner, J. Heitmann, and F. Steinmetz, "ahoi: Inexpensive, Low-power Communication and Localization for Underwater Sensor Networks and AUVs," *ACM Trans. Sens. Netw.*, vol. 16, no. 2, p. 18:1-18:46, Jan. 2020, doi: 10.1145/3376921.

[38] I. Vasilescu, K. Kotay, D. Rus, M. Dunbabin, and P. Corke, "Data collection, storage, and retrieval with an underwater sensor network," in *Proceedings of the 3rd international conference on Embedded networked sensor systems - SenSys '05*, San Diego, California, USA, 2005, p. 154. doi: 10.1145/1098918.1098936.

[39] D. Boyle, R. Kolcun, and E. Yeatman, *Energy-Efficient Communication in Wireless Networks*. IntechOpen, 2017. doi: 10.5772/65986.

[40] V. Tsiatsis, S. Karnouskos, J. Holler, D. Boyle, and C. Mulligan, *Internet of Things: Technologies and Applications for a New Age of Intelligence*. Academic Press, 2018.

[41] G. Hattab, M. El-Tarhuni, M. Al-Ali, T. Joudeh, and N. Qaddoumi, "An Underwater Wireless Sensor Network with Realistic Radio Frequency Path Loss Model," *Int. J. Distrib. Sens. Netw.*, vol. 9, no. 3, p. 508708, Mar. 2013, doi: 10.1155/2013/508708.

[42] U. M. Qureshi *et al.*, "RF Path and Absorption Loss Estimation for Underwater Wireless Sensor Networks in Different Water Environments," *Sensors*, vol. 16, no. 6, Jun. 2016, doi: 10.3390/s16060890.

[43] "LoRaWAN-Range, Part 1: The most important factors for a good LoRaWAN radio range - IoT Solutions - SmartMakers." https://smartmakers.io/en/lorawan-range-part-1-the-most-important-factors-for-a-good-lorawan-signal-range/ (accessed Aug. 04, 2021).

[44] T. Rappaport, *Wireless Communications: Principles and Practice*, 2nd ed. Prentice Hall PTR, 2002.

[45] M. Stojanovic, "On the relationship between capacity and distance in an underwater acoustic communication channel," in *Proceedings of the 1st ACM international workshop on Underwater networks*, New York, NY, USA, Sep. 2006, pp. 41–47. doi: 10.1145/1161039.1161049.

[46] "Water Quality Parameters." http://ftp.fosc.org/WQData/WQParameters.htm (accessed Dec. 16, 2021).

[47] Z. Zheng, Y. Fu, K. Liu, R. Xiao, X. Wang, and H. Shi, "Three-stage vertical distribution of seawater conductivity," *Sci. Rep.*, vol. 8, no. 1, p. 9916, Jul. 2018, doi: 10.1038/s41598-018-27931-y.

[48] A. I. Al-Shamma'a, A. Shaw, and S. Saman, "Propagation of electromagnetic waves at MHz frequencies through seawater," *IEEE Trans. Antennas Propag.*, vol. 52, no. 11, pp. 2843–2849, Nov. 2004, doi: 10.1109/TAP.2004.834449.

[49] C. Uribe and W. Grote, "Radio Communication Model for Underwater WSN," in *2009 3rd International Conference on New Technologies, Mobility and Security*, Dec. 2009, pp. 1–5. doi: 10.1109/NTMS.2009.5384789.

[50] A. Lavric, "LoRa (Long-Range) High-Density Sensors for Internet of Things," *J. Sens.*, vol. 2019, p. e3502987, Feb. 2019, doi: 10.1155/2019/3502987.

[51] Semtech, "Lora Design Guide for SX127x series." Semtech. [Online]. Available: https://www.rs-online.com/designspark/rel-assets/ds-assets/uploads/knowledge-items/application-notes-for-the-internet-of-things/LoRa%20Design%20Guide.pdf

[52] "BRATS - Advanced Amateur Radio Tuition Course." https://brats-qth.org/training/advanced/feed3.htm (accessed Nov. 09, 2021).

[53] Y. Zahedi, H. Ghafghazi, S. H. Syed Ariffin, and N. Kassim, *Feasibility of Electromagnetic Communication in Underwater Wireless Sensor Networks*. 2011, p. 623. doi: 10.1007/978-3-642-25462-8_55.

[54] "wavelength | Definition, Formula, & Symbol," *Encyclopedia Britannica*. https://www.britannica.com/science/wavelength (accessed Jul. 14, 2021).

[55] "ANT-MDIP5." Accessed: Nov. 12, 2021. [Online]. Available: https://docs.rs-online.com/8634/0900766b8158bd51.pdf

[56] "DIRECTIONAL YAGI ANTENNA, 830-890MHZ WITH 10DBI GAIN." https://www.rfsolutions.co.uk/antennas-c8/directional-yagi-antenna-830-890mhz-with-10dbi-gain-p165 (accessed Oct. 20, 2021).

[57] "RF Safety FAQ," *Federal Communications Commission*, Nov. 25, 2015. https://www.fcc.gov/engineering-technology/electromagnetic-compatibility-division/radio-frequency-safety/faq/rf-safety (accessed Sep. 13, 2021).

[58] "SX1276." https://www.semtech.com/products/wireless-rf/lora-core/sx1276 (accessed Aug. 25, 2021).

[59] "The LoPy4 is a quadruple bearer MicroPython enabled development board including LoRa, Sigfox, WiFi and Bluetooth," *Pycom*. https://pycom.io/product/lopy4/ (accessed Aug. 25, 2021).

[60] M. Zachmann, "The Best LoRa Settings for Range and Reliability," *Home Wireless*, Dec. 30, 2019. https://medium.com/home-wireless/testing-lora-radios-with-the-limesdr-mini-part-2-37fa481217ff (accessed Nov. 03, 2021).

[61] "STM32F4DISCOVERY - Discovery kit with STM32F407VG MCU * New order code STM32F407G-DISC1 (replaces STM32F4DISCOVERY) - STMicroelectronics." https://www.st.com/en/evaluation-tools/stm32f4discovery.html (accessed Aug. 25, 2021).

[62] "1554H2GYCL - Plastic Enclosure, Small, Polycarbonate, 61 mm, 119 mm, 180 mm, IP68." https://ie.farnell.com/hammond/1554h2gycl/small-enclosure-small-pc-grey/dp/2988671 (accessed Oct. 31, 2020).

[63] R. G. Donmez, "A STUDY ON PATH LOSS FOR INDOOR WIRELESS COMMUNICATION NETWORKS," p. 70.

[64] w8bya, *RF Attenuation of Common Plastics at 10 GHz*, (Jun. 28, 2020). Accessed: Nov. 03, 2021. [Online Video]. Available: https://www.youtube.com/watch?v=-olT_qjKwFw

[65] "Tyndall National Institute - Excellence in ICT Research." https://www.tyndall.ie/ (accessed Aug. 25, 2021).

[66] "What is a Refractometer & How Does it Work - Cole-Parmer." https://www.coleparmer.com/tech-article/refractometers (accessed Oct. 31, 2020).

[67] B. O'Flynn *et al.*, "SmartCoast: A Wireless Sensor Network for Water Quality Monitoring," in *32nd IEEE Conference on Local Computer Networks (LCN 2007)*, Oct. 2007, pp. 815–816. doi: 10.1109/LCN.2007.34.

[68] "Lesson Seven: How does sound travel in different environments?" https://kenanfellows.org/kfp-cp-sites/cp05/cp05/lesson-seven-how-does-sound-travel-different-environments/index.html (accessed Dec. 10, 2021).

[69] "Nondestructive Evaluation Physics : Waves." https://www.nde-ed.org/Physics/Waves/typesofwaves.xhtml (accessed Dec. 10, 2021).

[70] A. S. Dukhin and P. J. Goetz, Eds., "Chapter 3. Fundamentals of acoustics in liquids," in *Studies in Interface Science*, vol. 15, Elsevier, 2002, pp. 75–99. doi: 10.1016/S1383-7303(02)80014-X.

[71] E. B. Thorstad, A. H. Rikardsen, A. Alp, and F. Okland, "An overview of fish tags," *Turk. J. Fish. Aquat. Sci.*, vol. 13, no. 5, 2014, doi: 10.4194/1303-2712-v13_5_13.

[72] V. Krishnaswamy and S. S. Manvi, "Analysis of acoustic channel in underwater acoustic sensor network," in *2015 IEEE International Advance Computing Conference (IACC)*, Jun. 2015, pp. 233–236. doi: 10.1109/IADCC.2015.7154704.

[73] "4. FORMING THE ACOUSTIC EQUATIONS." http://www.fao.org/3/X5818E/x5818e05.htm (accessed Sep. 24, 2020).

[74] L. Hall, "The Origin of Ultrasonic Absorption in Water," *Phys. Rev.*, vol. 73, no. 7, pp. 775–781, Apr. 1948, doi: 10.1103/PhysRev.73.775.

[75] H. Jafarzadeh, M. Belcastro, and B. O'Flynn, "IMPAQT Miniaturized Underwater Acoustic Telemetry Platform: Transmitter Node System Design," in *Proc. SENSORCOMM*, Nov. 2020, pp. 34–37. Accessed: May 14, 2021. [Online]. Available: http://www.thinkmind.org/index.php?view=article&articleid=sensorcomm_2020_1_60_10031

[76] M. A. Ainslie and J. G. McColm, "A simplified formula for viscous and chemical absorption in sea water," *J. Acoust. Soc. Am.*, vol. 103, no. 3, pp. 1671–1672, Mar. 1998, doi: 10.1121/1.421258.

[77] "Calculation of absorption of sound in seawater - Underlying Physics." http://resource.npl.co.uk/acoustics/techguides/seaabsorption/physics.html (accessed Nov. 12, 2021).

[78] "relaxation phenomenon | physics and chemistry | Britannica." https://www.britannica.com/science/relaxation-phenomenon (accessed Nov. 12, 2021).

[79] F. Fisher and V. Simmons, "Discovery of boric acid as cause of low frequency sound absorption in the ocean," in *OCEAN 75 Conference*, Sep. 1975, pp. 21–24. doi: 10.1109/OCEANS.1975.1154163.

[80] "Ocean Acidification | Smithsonian Ocean." http://ocean.si.edu/ocean-life/invertebrates/ocean-acidification (accessed Sep. 25, 2020).

[81] "Calculation of absorption of sound in seawater." http://resource.npl.co.uk/acoustics/techguides/seaabsorption/ (accessed Sep. 25, 2020).

[82] R. Ghaffarivardavagh, S. S. Afzal, O. Rodriguez, and F. Adib, "Ultra-Wideband Underwater Backscatter via Piezoelectric Metamaterials," in *Proceedings of the Annual conference of the ACM Special Interest Group on Data Communication on the applications, technologies, architectures, and protocols for computer communication*, Virtual Event USA, Jul. 2020, pp. 722–734. doi: 10.1145/3387514.3405898.

[83] "Electric power," *Wikipedia*. Oct. 30, 2021. Accessed: Nov. 06, 2021. [Online]. Available: https://en.wikipedia.org/w/index.php?title=Electric_power&oldid=1052682026

[84] X. Jiang, "Chapter 15 - Optical performance monitoring in optical long-haul transmission systems," in *Optical Performance Monitoring*, C. C. K. Chan, Ed. Oxford: Academic Press, 2010, pp. 423–446. doi: 10.1016/B978-0-12-374950-5.00015-8.

[85] T. N. Pearsons, "The Juvenile Salmon acoustic telemtry system : a new tool," *Fisheries*, vol. 35, no. 1, pp. 23–31, Jan. 2010, doi: 10.1577/1548-8446-35.1.23.

[86] R. B. Mitson and T. J. Storeton-west, "A transponding acoustic fish tag," *Radio Electron. Eng.*, vol. 41, no. 11, pp. 483–489, Nov. 1971, doi: 10.1049/ree.1971.0147.

[87] H. Li, Z. D. Deng, Y. Yuan, and T. J. Carlson, "Design Parameters of a Miniaturized Piezoelectric Underwater Acoustic Transmitter," *Sensors*, vol. 12, no. 7, Art. no. 7, Jul. 2012, doi: 10.3390/s120709098.

[88] "CeramTec Electro Ceramics (formerly provided by Morgan Advanced Materials)." https://www.ceramtec.com/electro-ceramics/ (accessed Nov. 03, 2021).

[89] "Piezoelectric applications for both medical and industrial fields | EBL Products." https://eblproducts.com/ (accessed Nov. 09, 2021).

[90] "AS-1 Hydrophone." https://www.aquarianaudio.com/as-1-hydrophone.html (accessed Nov. 01, 2020).

[91] B. D. Manager, "Broadband," *Sensor Technology Ltd.*, Jan. 14, 2014. https://sensortechcanada.com/products/custom-hydrophones/spherical-

hydrophones/broadband-passive-spherical-hydrophone/ (accessed Nov. 01, 2020).
[92] "BII-7003Datasheet Technical document." Accessed: Nov. 01, 2020. [Online]. Available: https://www.benthowave.com/products/Specs/BII-7003Datasheet.pdf
[93] "H3 Technical document." Accessed: Nov. 01, 2020. [Online]. Available: https://www.aquarianaudio.com/AqAudDocs/H3_manual.pdf
[94] B. Benson, "Design of a low-cost underwater acoustic modem for short- range sensor networks," UC San Diego, 2010. Accessed: Sep. 24, 2020. [Online]. Available: https://escholarship.org/uc/item/8j70s26c
[95] S. P. Ceramics, "Steminc Piezoelectric Ceramic Manufacturer," *STEMINC*. https://www.steminc.com/PZT/piezo-ceramic-cylinder-26x22x13mm-43-khz (accessed Nov. 01, 2020).
[96] "Boost converter," *Wikipedia*. May 07, 2021. Accessed: Aug. 31, 2021. [Online]. Available: https://en.wikipedia.org/w/index.php?title=Boost_converter&oldid=1022011215
[97] "Please tell me a current consumption by a Piezoelectric Sounder (External Drive Type). | Murata Manufacturing Co., Ltd." https://www.murata.com/en-us/support/faqs/products/sound/sounder/char/sch0003 (accessed Sep. 27, 2020).
[98] EETimes, "EETimes - Choosing the optimum switching frequency of your DC/DC converter," *EETimes*, Oct. 25, 2006. https://www.eetimes.com/choosing-the-optimum-switching-frequency-of-your-dc-dc-converter/ (accessed Aug. 31, 2021).
[99] "LT8337/LT8337-1 Technical document." Accessed: Oct. 22, 2021. [Online]. Available: https://www.analog.com/media/en/technical-documentation/data-sheets/lt8337-8337-1.pdf
[100] "MAX1771 Technical document." Accessed: Sep. 03, 2021. [Online]. Available: https://datasheets.maximintegrated.com/en/ds/MAX1771.pdf
[101] "TPS61040 Technical document." Accessed: Oct. 22, 2021. [Online]. Available: https://www.ti.com/lit/ds/symlink/tps61040.pdf?ts=1634897886531&ref_url=https%253A%252F%252Fwww.ti.com%252Fproduct%252FTPS61040
[102] "IRLML6344 Technical document." Accessed: Nov. 03, 2021. [Online]. Available: https://www.infineon.com/dgdl/Infineon-IRLML6344-DataSheet-v01_01-EN.pdf?fileId=5546d462533600a4015356689c44262c
[103] "Basic Calculation of a Boost Converter's Power Stage." Texas Instrument. [Online]. Available: https://www.ti.com/lit/an/slva372c/slva372c.pdf
[104] "What is the working of a H-bridge circuit? - Quora." https://www.quora.com/What-is-the-working-of-a-H-bridge-circuit (accessed Sep. 03, 2021).
[105] "Selecting the Right CMOS Analog Switch." https://www.maximintegrated.com/en/design/technical-documents/app-notes/5/5299.html (accessed Sep. 03, 2021).

[106] “ADG1436 Technical document.” Accessed: Nov. 02, 2020. [Online]. Available: https://www.analog.com/media/en/technical-documentation/data-sheets/ADG1436.pdf

[107] “STM32 Microcontrollers - STMicro | Mouser.” https://www.mouser.ie/new/stmicroelectronics/stm32/ (accessed Sep. 05, 2021).

[108] “503562 Battery document.” Accessed: Oct. 28, 2021. [Online]. Available: https://cdn-shop.adafruit.com/datasheets/503562+1200mah.pdf

[109] “LiPo Batteries - Texim Europe.” [Online]. Available: https://www.texim-europe.com/getfile.ashx?id=126229

[110] “TPS78230DDCT | Buy TI parts | TI.com.” https://www.ti.com/store/ti/en/p/product/?p=TPS78230DDCT (accessed Sep. 16, 2021).

[111] N. Nowsheen, C. Benson, and M. Frater, “Design of a high frequency FPGA acoustic modem for underwater communication,” in *OCEANS’10 IEEE SYDNEY*, Sydney, Australia, May 2010, pp. 1–6. doi: 10.1109/OCEANSSYD.2010.5603819.

[112] D. Sundman, M. M. Lopez, and L. R. Wilhelmsson, “Partial On-Off Keying - A Simple Means to Further Improve IoT Performance,” in *2018 Global Internet of Things Summit (GIoTS)*, Jun. 2018, pp. 1–5. doi: 10.1109/GIOTS.2018.8534548.

[113] “Resonance, damping and frequency response,” *Deranged Physiology*. https://derangedphysiology.com/main/cicm-primary-exam/required-reading/cardiovascular-system/Chapter%20734/resonance-damping-and-frequency-response

[114] “TFBS4650 Technical document.” Accessed: Nov. 02, 2020. [Online]. Available: https://www.vishay.com/docs/84672/tfbs4650.pdf

[115] “PCB Design Software & Tools | Altium.” https://www.altium.com/ (accessed Sep. 07, 2021).

[116] “Nyquist–Shannon sampling theorem,” *Wikipedia*. Oct. 06, 2021. Accessed: Nov. 02, 2021. [Online]. Available: https://en.wikipedia.org/w/index.php?title=Nyquist%E2%80%93Shannon_sampling_theorem&oldid=1048443869

[117] “MCP73831 Technical document.” Accessed: Oct. 28, 2021. [Online]. Available: https://ww1.microchip.com/downloads/en/DeviceDoc/MCP73831-Family-Data-Sheet-DS20001984H.pdf

[118] “STM32L0x2 Technical document.” Accessed: Oct. 28, 2021. [Online]. Available: https://www.st.com/resource/en/reference_manual/dm00108281-ultralowpower-stm32l0x2-advanced-armbased-32bit-mcus-stmicroelectronics.pdf

[119] R. W. Franklin, “ANALYSIS OF SOLID TANTALUM CAPACITOR LEAKAGE CURRENT,” p. 7.

[120] “MIC5239 Technical document.” Accessed: Sep. 08, 2021. [Online]. Available: http://ww1.microchip.com/downloads/en/DeviceDoc/mic5239.pdf

[121] “MAX660 Technical document.” Accessed: Sep. 08, 2021. [Online]. Available: https://datasheets.maximintegrated.com/en/ds/MAX660.pdf

[122] "Guide to Integrated Charge Pump DC-DC Conversion | Maxim Integrated." https://www.maximintegrated.com/en/design/technical-documents/tutorials/7/725.html (accessed Sep. 08, 2021).

[123] "LT1792 - Low Noise, Precision, JFET Input Op Amp." https://www.analog.com/media/en/technical-documentation/data-sheets/1792f.pdf

[124] C. Renner and A. J. Golkowski, "Acoustic modem for micro AUVs: design and practical evaluation," in *Proceedings of the 11th ACM International Conference on Underwater Networks & Systems - WUWNet '16*, Shanghai, China, 2016, pp. 1–8. doi: 10.1145/2999504.3001076.

[125] "DC Servos." https://sound-au.com/articles/dc-servo.htm (accessed Nov. 09, 2021).

[126] C. Knowlton, "What are common underwater sounds?," *Discovery of Sound in the Sea*, Nov. 29, 2016. https://dosits.org/science/sounds-in-the-sea/what-are-common-underwater-sounds/ (accessed Nov. 01, 2021).

[127] "Filter Design Tool | Filter Wizard | Analog Devices." https://tools.analog.com/en/filterwizard/ (accessed Nov. 02, 2020).

[128] "OPA365 data sheet, product information and support | TI.com." https://www.ti.com/product/OPA365 (accessed Sep. 08, 2021).

[129] "AD5245 Datasheet and Product Info | Analog Devices." https://www.analog.com/en/products/ad5245.html (accessed Sep. 08, 2021).

[130] Dejan, "What is Schmitt Trigger | How It Works," *HowToMechatronics*, Aug. 24, 2015. https://howtomechatronics.com/how-it-works/electrical-engineering/schmitt-trigger/ (accessed Sep. 09, 2021).

[131] F. Asgarian and A. M. Sodagar, "Wireless Telemetry for Implantable Biomedical Microsystems," 2011. doi: 10.5772/12997.

[132] M. Hosseinnejad and A. Erfanian, "A VCO-free low-power fully digital BPSK demodulator for implantable biomedical microsystems," in *2017 24th IEEE International Conference on Electronics, Circuits and Systems (ICECS)*, Dec. 2017, pp. 474–477. doi: 10.1109/ICECS.2017.8292052.

[133] "Multisim Live Online Circuit Simulator," *NI Multisim Live*. https://www.multisim.com/ (accessed Sep. 09, 2021).

[134] Stephanos, "Costas Loop for Binary Phase Shift Keying (BPSK) Demodulation," *stephanos.io*, Nov. 27, 2016. https://stephanos.io/archives/46 (accessed Sep. 09, 2021).

[135] E. Hagemann, "The Costas Loop – An Introduction," 2001. https://zipcpu.com/doc/DSP010315F1.pdf

[136] "CD54HC4046a Technical Document." Accessed: Oct. 28, 2021. [Online]. Available: https://www.ti.com/lit/ds/symlink/cd54hc4046a.pdf?ts=1635326412260&ref_url=https%253A%252F%252Fwww.google.com%252F

[137] "CD4046BC Micropower Phase-Locked Loop." http://www.mit.edu/~6.331/CD4046BC.pdf

[138] "Oversampling," *Wikipedia*. Jul. 20, 2021. Accessed: Nov. 02, 2021. [Online]. Available: https://en.wikipedia.org/w/index.php?title=Oversampling&oldid=1034545823

[139] "dm00628458-getting-started-with-the-stm32h7-series-mcu-16bit-adc-stmicroelectronics.pdf." Accessed: Sep. 10, 2021. [Online]. Available: https://www.st.com/resource/en/application_note/dm00628458-getting-started-with-the-stm32h7-series-mcu-16bit-adc-stmicroelectronics.pdf

[140] "LTC3124 Datasheet and Product Info | Analog Devices." https://www.analog.com/en/products/ltc3124.html (accessed Aug. 31, 2021).

[141] "FT232H Technical document." Accessed: Nov. 03, 2021. [Online]. Available: https://ftdichip.com/wp-content/uploads/2020/07/DS_FT232H.pdf

[142] Node.js, "Node.js," *Node.js*. https://nodejs.org/en/ (accessed Nov. 03, 2021).

[143] "PulseView - sigrok." https://sigrok.org/wiki/PulseView (accessed Nov. 10, 2021).

[144] "SDIO/iSDIO | SD Association," Dec. 11, 2020. https://www.sdcard.org/developers/sd-standard-overview/sdio-isdio/ (accessed Nov. 13, 2021).

[145] "IS62WV25616DxLL Technical document." Accessed: Sep. 10, 2021. [Online]. Available: https://media.digikey.com/pdf/Data%20Sheets/ISSI%20PDFs/IS62WV25616DxLL,_IS65WV25616DxLL.pdf

[146] "HC-05 Bluetooth Module Pinout, Specifications, Default Settings, Replacements & Datasheet." https://components101.com/wireless/hc-05-bluetooth-module (accessed Sep. 10, 2021).

[147] "STM32H750 Value line - Arm Cortex-M7 core Microcontrollers (MCUs) - STMicroelectronics." https://www.st.com/en/microcontrollers-microprocessors/stm32h750-value-line.html (accessed Aug. 17, 2020).

[148] "Analog & Digital Grounding: Principles for Mixed-Signal Designs | Arrow.com," *Arrow.com*. https://www.arrow.com/en/research-and-events/articles/principles-of-grounding-for-mixed-signal-designs (accessed Sep. 10, 2021).

[149] "Hantek2000 Series - Hantek Electronic & Your testing solution provider." http://hantek.com/products/detail/13174 (accessed Oct. 27, 2021).

[150] HamedJafarzadeh, *HamedJafarzadeh/IMPAQT-Telemetery-Platform*. 2021. Accessed: Aug. 10, 2021. [Online]. Available: https://github.com/HamedJafarzadeh/IMPAQT-Telemetery-Platform

[151] E. Lee, S. Park, and S. Cho, "An On-Off Keying LC Oscillator-Based Acoustic Transmitter with Fast Turn-On and Turn-Off Time," in *2019 IEEE Asia Pacific Conference on Circuits and Systems (APCCAS)*, Nov. 2019, pp. 369–372. doi: 10.1109/APCCAS47518.2019.8953070.

[152] "Chirp - an overview | ScienceDirect Topics." https://www.sciencedirect.com/topics/earth-and-planetary-sciences/chirp (accessed Nov. 10, 2021).

Appendix

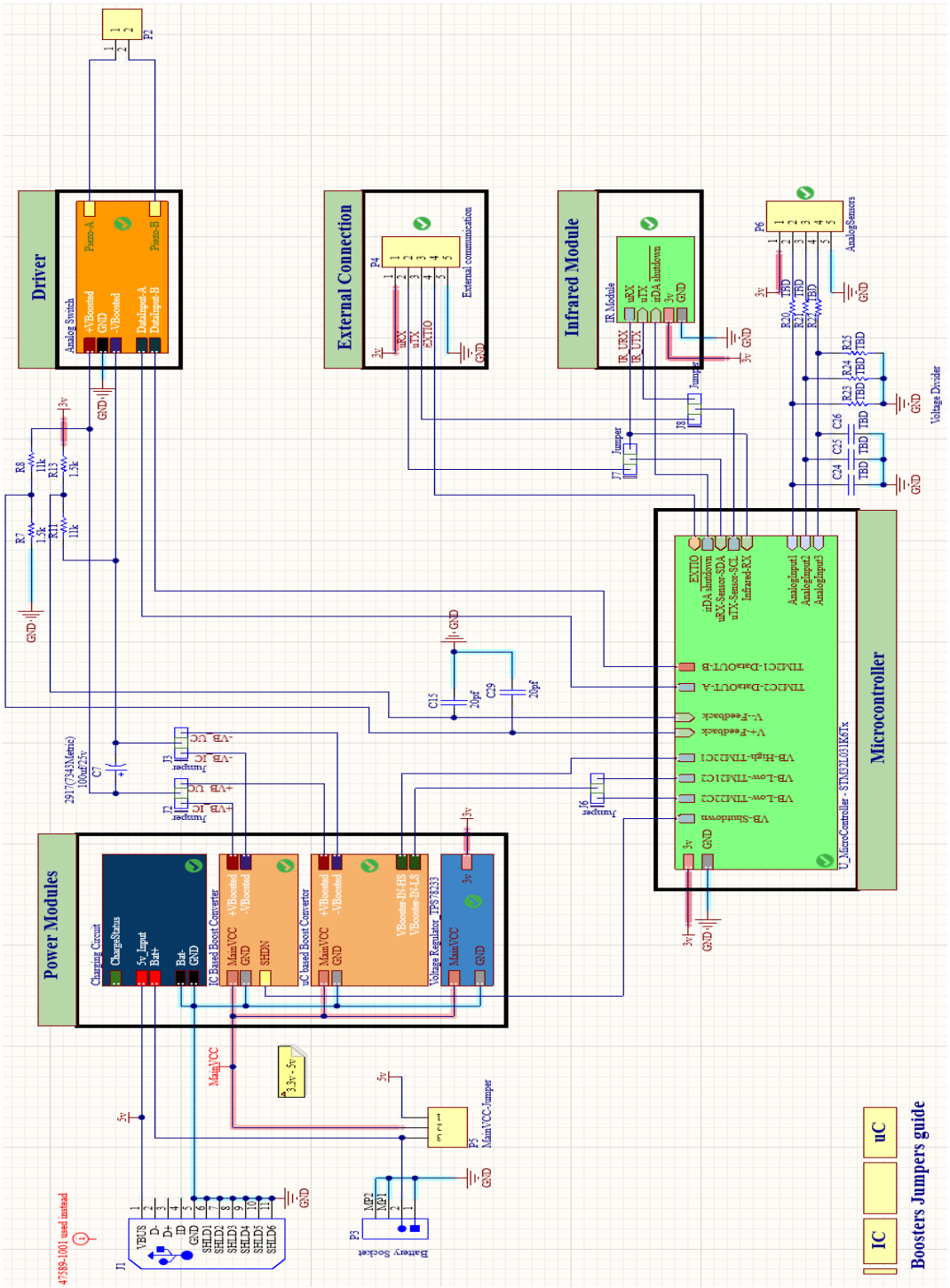


Figure 95 IMPAQT Transmitter schematic block diagrams

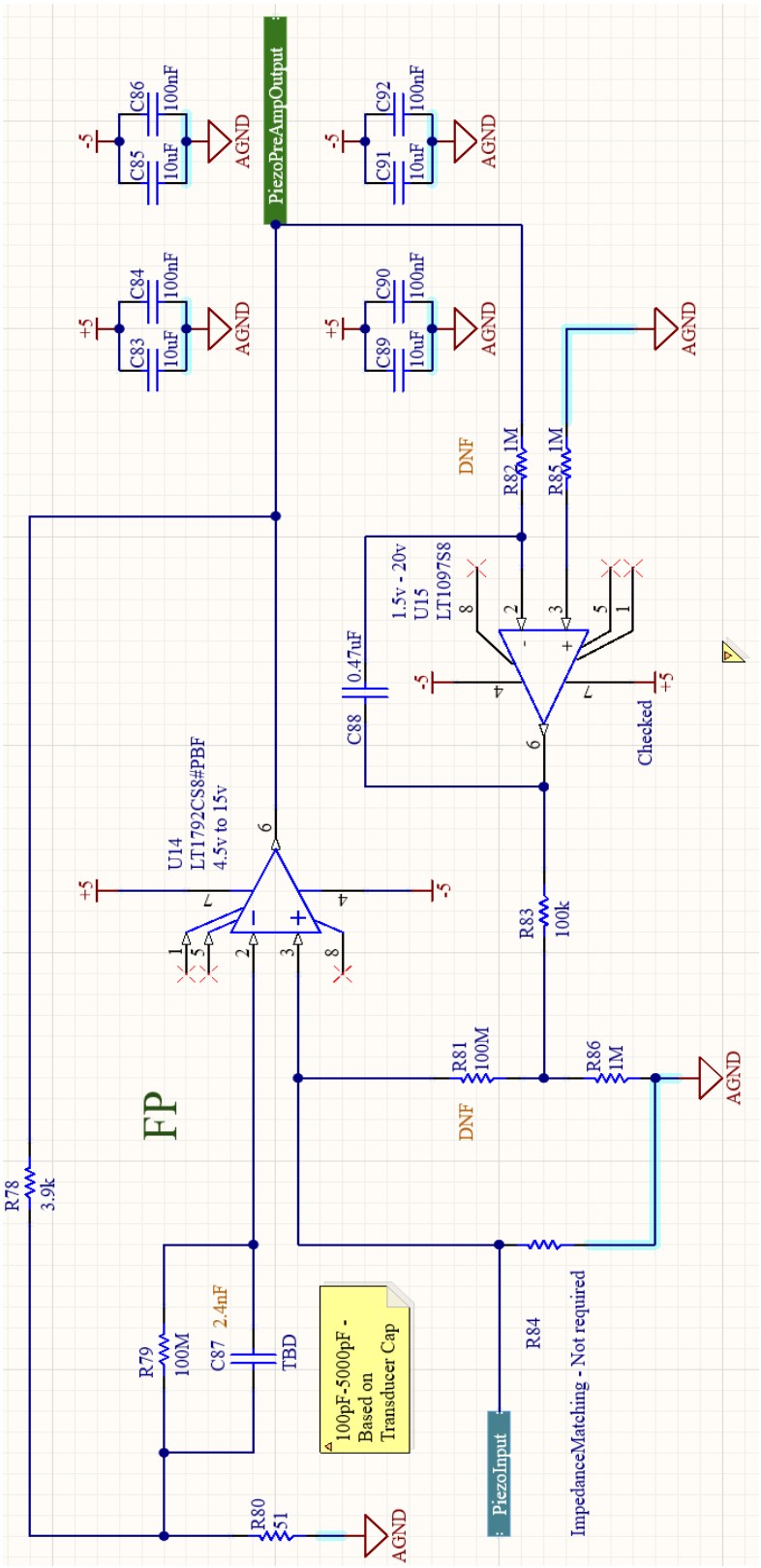


Figure 96 LT1792-based hydrophone driver circuit

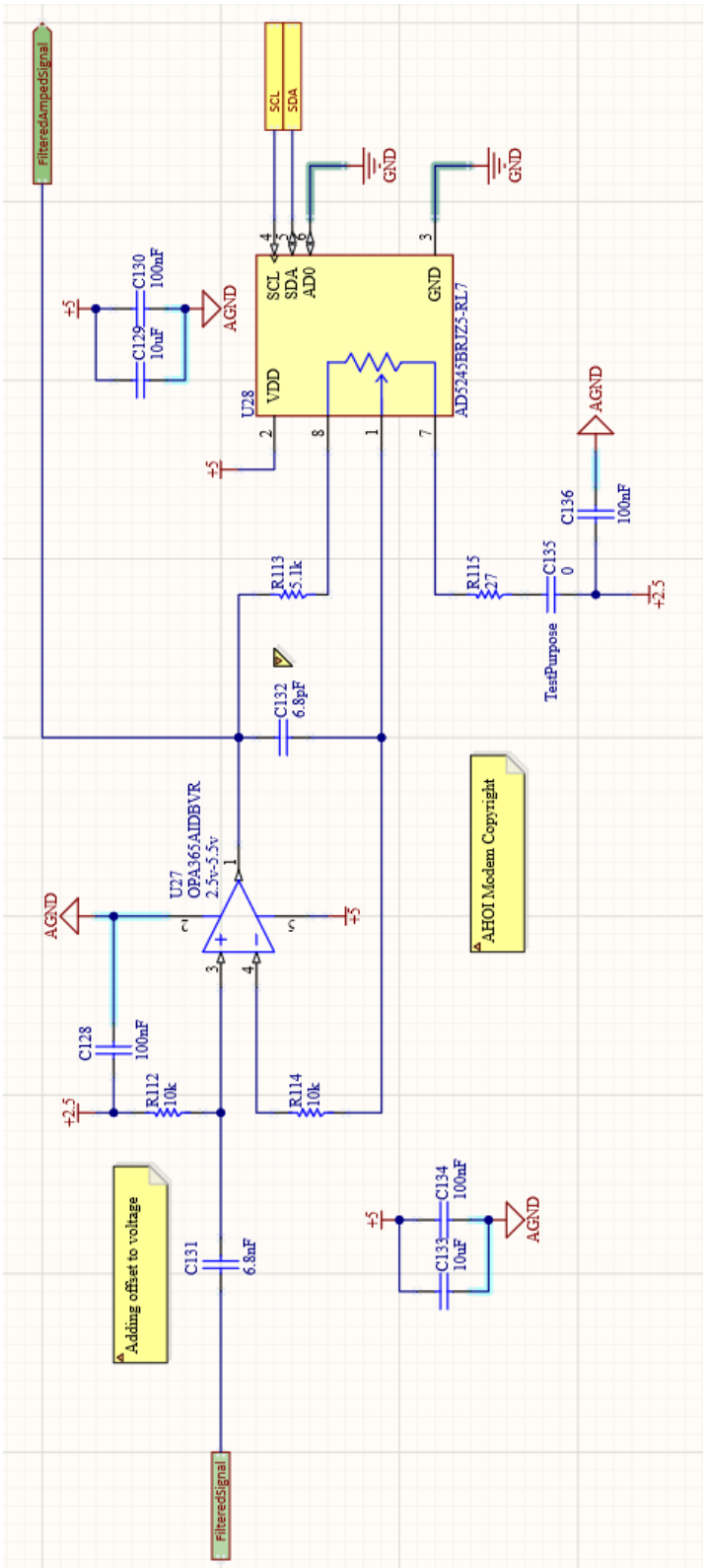


Figure 97 Digitally controlled variable gain amplifier

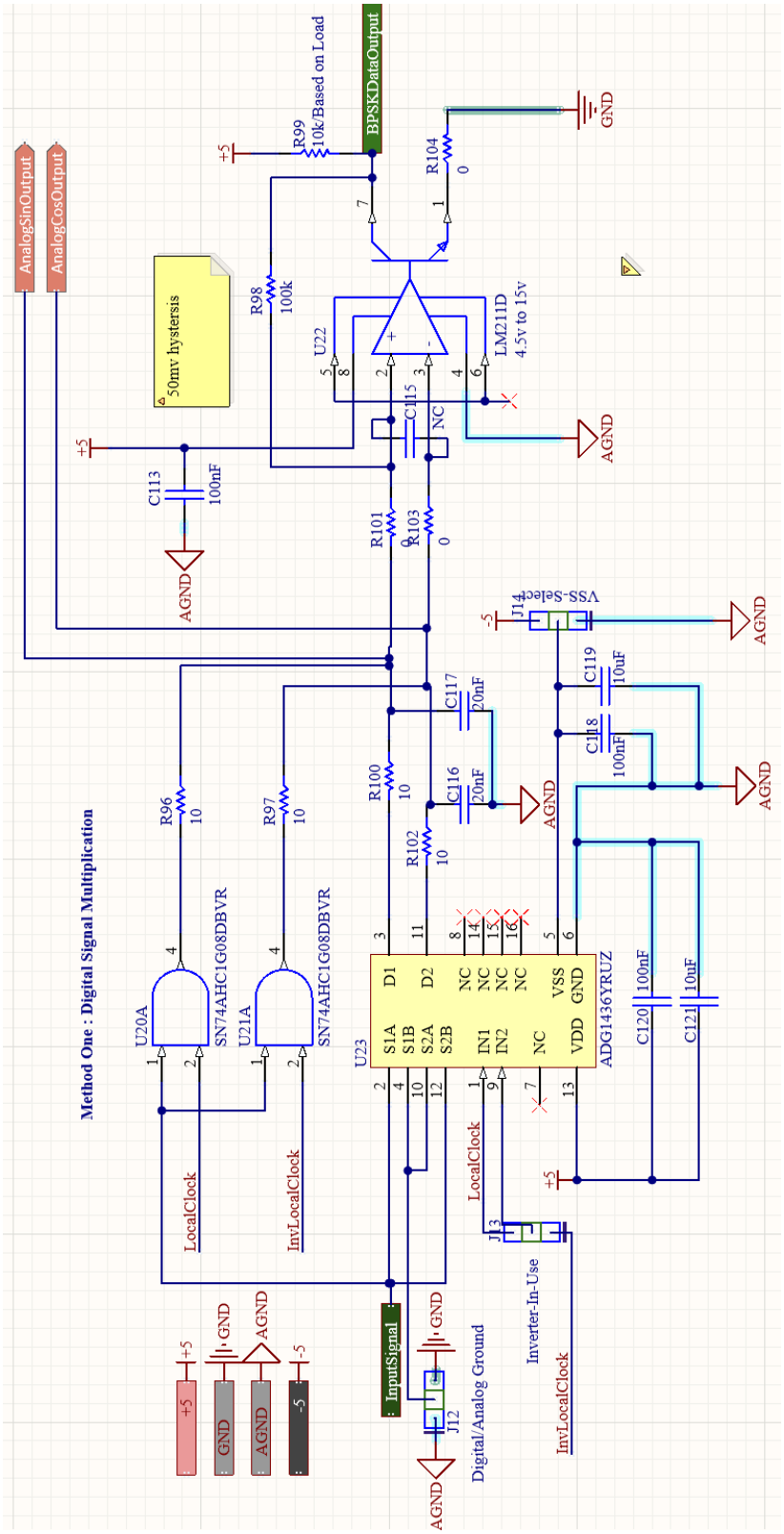


Figure 98 Modified Costas loop using an analog switch

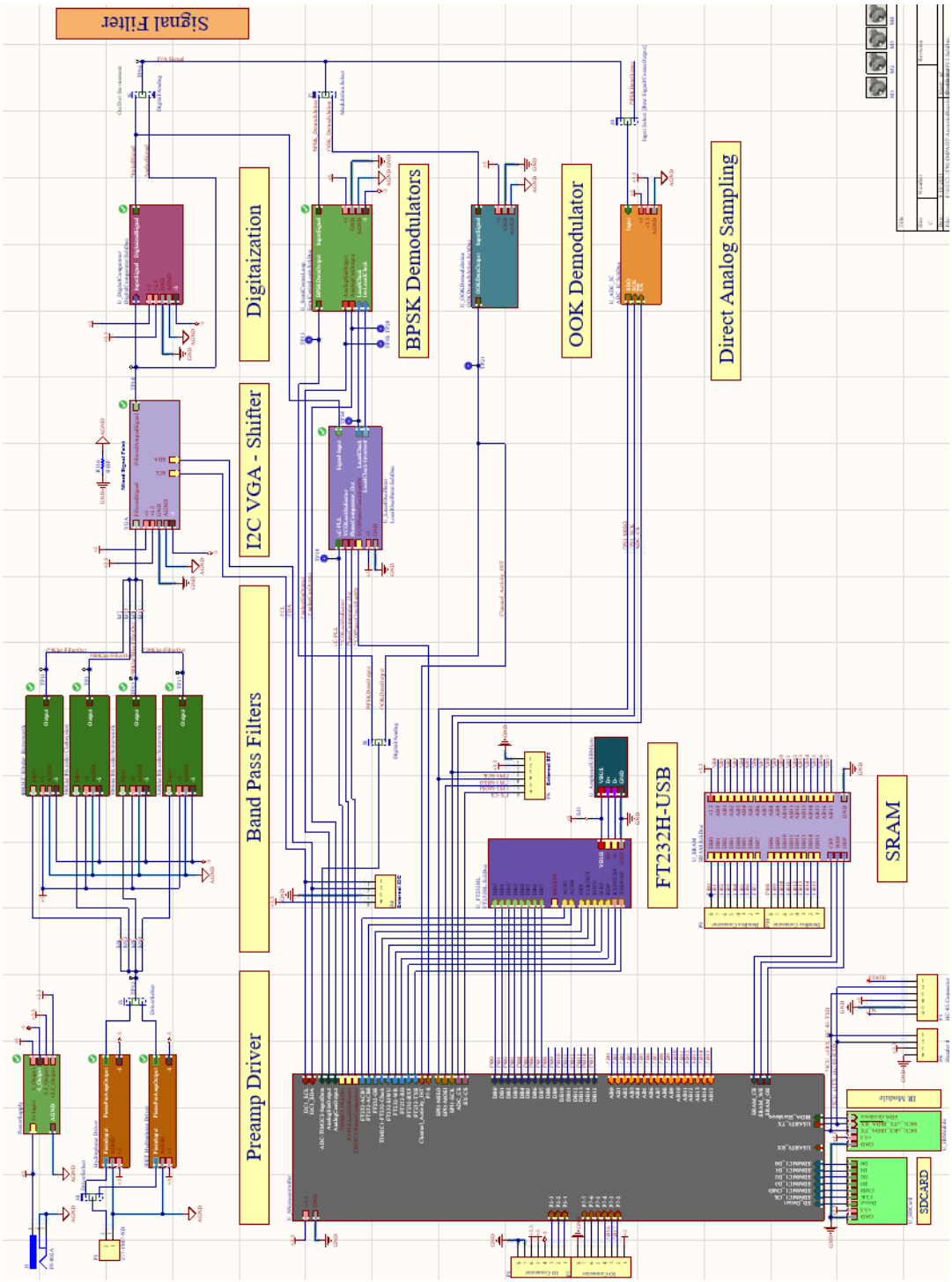


Figure 99 Overview of the IMPAQT receiver schematic